1-20-2015

Geomorphic and Structural Evidence for an Active Tectonostratigraphic Boundary in an Accretionary Wedge: the Southern Central Range, Taiwan

Chung Huang
University of Connecticut - Storrs, huangchung@gmail.com

Geomorphic and Structural Evidence for an Active Tectonostratigraphic Boundary in an Accretionary Wedge: the Southern Central Range, Taiwan

Chung Huang, Ph.D.

University of Connecticut, 2015

Taiwan is an active accretionary wedge resulting from the collision between the Chinese passive margin and the Luzon magmatic arc. This study focus on the southern Central Range of Taiwan as an example to demonstrate the internal deformation of an active accretionary wedge.

Recent leveling survey shows that the uplift rate in southern Taiwan is higher in the core of the wedge and lower on both flanks. We propose that this differential uplift rate is accommodated by major structures that should be recorded in geologic and geomorphic data. In this study, we suggest that one of the structures is the Tulungwan-Chaochou fault system, which separates Miocene slates from unmetamorphosed rocks of the same age.

The study revealed a major structure along the east flank of the range, the Tulungwan-Chaochou fault system, and an associated regional-scale, SSW-plunging antiform composed of slaty cleavage that verges to the NW. The antiform is a post-metamorphic structure and is an active structure based on field data and geodetic survey. The second part of the study demonstrates that landslides are preferentially developed where structural cleavage and hillslopes dip in the same direction, suggesting that the orientation of tectonic fabrics is important in landslide development. The last part of the study compiled the geomorphic indices (river steepness index, k_{sn}, and basin asymmetry factor, AF) and geodetic data. The results suggest that the Tulungwan-Chaochou fault system has been active at a time scale sufficient to influence the evolution of the watersheds in the hanging wall.

Geomorphic and Structural Evidence for an Active Tectonostratigraphic Boundary in an Accretionary Wedge: the Southern Central Range, Taiwan

Chung Huang

B.S., National Taiwan University, 2005

M.S., National Taiwan University, 2007

A Dissertation

Submitted in Partial Fulfillment of the

Requirements for the Degree of

Doctor of Philosophy

at the

University of Connecticut

2015

APPROVAL PAGE

Doctor of Philosophy Dissertation

Geomorphic and Structural Evidence for an Active Tectonostratigraphic Boundary in an Accretionary Wedge: the Southern Central Range, Taiwan

Presented by

Chung Huang, B.S., M.S.

Major Advisor _____
Dr. Timothy B. Byrne

Associate Advisor _____
Dr. William B. Ouimet

Associate Advisor _____
Dr. Jean M. Crespi

Associate Advisor _____
Dr. Jonathan R. Gourley

Associate Advisor _____
Dr. Jonathan C. Lewis

University of Connecticut
2015

AKNOWLEDGEMENTS

The past five an half years in University of Connecticut was a memorable experience for me. Not only the knowledge I learned from class, but also the life and culture in New England. This work would not have been possible if it were not for the support of many individuals and institutions. First of all, I would like to thank my major advisor, Dr. Tim Byrne, for his advice and support during my stay in University of Connecticut. He was always helpful, and full of encouragement during his lecture both in Storrs or measuring slicken fibers in Taiwan. I would like to thank Dr. Jean Crespi for her insightful comments and her help when I faced difficulties in my life. I am grateful to have Dr. Will Ouimet as my co-advisor, he helped me to understand the beauty of fluvial geomorphology which I never knew before. I also would like to thank Drs. Jon Lewis and Jon Gourley for being my committee members and their comments and discussions of my research.

I appreciate the help and support from my colleague and friends in the University of Connecticut: Januka Attanayake, Sheng-Yu Chen, Ching-Chang Chung, Sy-Han “Steven” Chiou, Christin Donnelly, James Farrell, Meredith Fichman, Patrick Gonsoulin-Getty, Abi Hastillo, Ellen Lamont, Gong-Yi Liao, Hui-Jan Lin, Ching-Yang Liu, David Mirakian, Kristen Myshrall, Amberlee Nicoulin, Mark Smith, Neil Shea, Fu-Chang “Edison” Sun, Yu-Bo Wang, and Tai-Yi Wu.

This study could not be done without the help from Taiwan, I would like to thank to the Taiwanese scientists and geologists who supported us while working in Taiwan. Drs. Yu-Chang Chan, Jian-Cheng Lee,

and Chih-Tung Chen from Institute from the Earth Sciences of Academia Sinica, Dr. Hao-Tsu Chu and Mr. Yu-Chung Hsieh from the Central Geological Survey of Taiwan, Drs. Hao Kuo-Chen, Chung-Pai Chang, and Andrew Lin from the National Central University, Drs. Ruey-Juin Rau and Kuo-En Ching from the National Cheng Kung University, Drs. Yuan-Hsi Lee and Meng-Long Hsieh from the National Chung Cheng University, Drs. Jyr-Ching Hu, Chia-Yu Lu, Jonny Wu, John Suppe, Bruce Shyu, Hsin-Hua Huang, Chao-Lung Tang and Mr. Wei-Hao Hsu from the National Taiwan University, Dr. Mong-Han Huang from the University of California, Berkeley, and Mr. Li-Jan Sun from the United Geotech Inc.

Finally I would like to thank my family for their support. I really appreciate the understanding and help from my father Chih Huang, my mother Lin Wang, my sister Hua "Rosa" Huang, my uncle Kiang-Tay Huang and my aunt May Huang. The last sentence is for my girlfriend Hsuan-Wei – thank you for everything you have done for me in the past nine years.

TABLE OF CONTENTS

LIST OF TABLE

LIST OF FIGURES

PREFACE

Mechanisms of active mountain building are well-described by wedge theory (Dahlen, 1990; Davis et al., 1983; Suppe, 1981) and internal deformation is an important factor in maintaining critical taper (Malavieille, 2010). Thrust faults, folds and tectonic cleavages are examples of internal deformation, and can contribute significantly to growth of the wedge even as the deformation front propagates into the foreland.

Thrusts in the inner part of a wedge that are active while the deformation front propagates into the foreland are called "out-of-sequence-thrusts" or OOSTs. Out of sequence thrusts tend to show hinterland propagation and can represent reactivation of older in-sequence-thrusts or the development of a new thrust that cuts through a deformed thrust sheet (Morley, 1988). Out of sequence thrusts can also be regionally extensive, deforming a significant portion of the inner part of an active accretionary wedge and generating earthquakes of large magnitude (Moore et al., 2009; Park et al., 2002; Strasser et al., 2009). In other words, OOSTs form an important component of accretion prism tectonics, including the generation of earthquakes.

Taiwan is a growing wedge that formed from the collision between the Philippine Sea and Eurasia Plates at 82 mm/yr (Yu et al., 1997) since about 5Ma (Seno, 1977; Teng, 1990) and exposes a series of tectonostratigraphic units that form an accretionary wedge (Ho, 1986). Many of the boundaries between different units are also considered to be tectonically active and could cause seismic hazards (Shyu et al.,

2005). To understand the internal deformation pattern of Taiwan, integrated structural and geomorphological studies have become important. This study focuses on the southern Central Range of Taiwan for the following reasons. First, the southern Central Range is a single mountain belt and has only a few contacts with adjacent units, and thus the regional scale deformation patterns could be relatively simple. Second, high uplift rates are reported in the southern Central Range, indicating that the orogen is active although specific accommodation structures have not been previously identified. And thirdly, the southern Central Range is a relatively young part of the mountain belt, and may have a more straightforward deformation history compared to other parts of the mountain belt. The following three chapters focus on the patterns of late stage structures and their evolution, and on the geomorphic indices and landslide patterns which reflect deformation and uplift of the southern Central Range of Taiwan.

Chapter one focuses on the geometry and late stage history of the slaty cleavage in the Miocene Changshan Formation in the western side of the southern Central Range. Two major structures are recognized in this area: the Tulungwan-Chaochou fault system, and the Laonung antiform. The Tulungwan-Chaochou fault system represents the boundary between a slate belt of moderate metamorphic grade and a relatively unmetamorphosed fold-and-thrust belt. This 75-km-long fault system is also one of the most conspicuous topographic features in Taiwan. Recent field mapping of fabrics and brittle faults show that a 45-km-long west-northwest-vergent antiform defined by folded slaty cleavage exists in the hanging wall of

the fault; informally, we refer to this structure as the Laonung antiform. The Laonung antiform has not been previously described and apparently formed in a brittle environment. The antiform also appears to be active based on data from a recent geodetic survey and river incision rates derived from river terraces present along the crest of the antiform. The flat crest and tight forelimb of the antiform suggest a two-stage deformation model composed of fault-bend folding followed by a trishear folding. I infer that this regional scale fold is associated with an out of sequence thrust that splays upward from the main detachment.

Chapter two focuses on the distribution of landslides in the southern Central Range, and the spatial relation between landslides and structural fabrics. The landslide pattern can reflect the local strength of the rocks or geological structures (Chen et al., 2009; Guzzetti et al., 2008), and we suggest the landslides in the southern Central Range reflect the rock anisotropy. In this study, θ_D is defined as the angle between the direction of hill slope and the direction of cleavage dip. A θ_D value that is close to 0° indicates that the hillslope direction is sub parallel to the cleavage dip direction, whereas a θ_D value equal to 180° indicates the hillslope direction is opposite to the cleavage dip direction. A comparison of θ_D values from areas with landslides to θ_D values from the whole field area suggests an important conclusion about the role of tectonic fabrics in landslide development. For example, in the slate belt, which has a well-developed penetrative cleavage, landslides develop preferentially in areas with low θ_D values. In contrast, landslides in the pre-Tertiary schist Tananao Metamorphic Complex form preferentially in areas of high θ_D values. The result

suggest that θ_D correlates with rock anisotropy; that is, when the rock has a strong anisotropy (e.g., slate), landslides tend to occur in areas of lower θ_D values, and when the rock has weak anisotropy (e.g., schist), landslides form in areas with no preferred θ_D value.

Chapter three focuses on two geomorphic indices that can provide information on patterns of differential uplift: River steepness index (k_{sn}) and basin asymmetry factor (AF). k_{sn} values can reflect the combination of uplift rate and rock erodibility, higher k_{sn} can be related to stronger rock or higher uplift rate (Wobus et al., 2006). AF is the ratio between the two sub-watersheds in a drainage basin divided by the main trunk stream (Hare and Gardner, 1985). A primary assumption in using AF is that higher erosion rates will enlarge the drainage area, so the ratio between the two watersheds of a river will reflect differential erosion rates. Erosion rates can be related to uplift rate, rock erodibility, and rock anisotropy within a drainage basin. In this study, however, the AF is mainly controlled by the uplift rate, which means the asymmetry of the drainage basins reflect differential uplift or tilting of the watershed.

Taken together, the results from Chapter 1, 2 and 3 argue for higher uplift rates in the north part of the southern Central Range. Detailed field studies also show that uplift along the northwestern flank of the range is accommodated by form of a regional-scale antiform that may be associated with a crustal scale out of sequence thrust. Although specific structures that accommodated uplift along the eastern flank of the

range have not been identified, higher uplift rates in the north have formed asymmetric watersheds that progressively increase in asymmetry to the north.

REFERENCE

Chen, C.-H., Ke, C.-C., Wang, C.-L., 2009. A back-propagation network for the assessment of susceptibility to rock slope failure in the eastern portion of the Southern Cross-Island Highway in Taiwan. Environmental geology 57, 723-733.

Dahlen, F.A., 1990. Critical taper model of fold-and-thrust belts and accretionary wedges. Annual Reviews of Earth and Planetary Sciences 18, 55-99.

Davis, D., Suppe, J., Dahlen, F.A., 1983. Mechanics of fold-and-thrust belts and accretionary wedges. Journal of Geophysical Research 88, 1153-1172.

Guzzetti, F., Peruccacci, S., Rossi, M., Stark, C.P., 2008. The rainfall intensity–duration control of shallow landslides and debris flows: an update. Landslides 5, 3-17.

Hare, P.W., Gardner, T., 1985. Geomorphic indicators of vertical neotectonism along converging plate margins, Nicoya Peninsula, Costa Rica. Allen and Unwin, Boston, 75-104.

Ho, C.S., 1986. A synthesis of the geologic evolution of Taiwan. Tectonophysics 125, 1-16.

Malavieille, J., 2010. Impact of erosion, sedimentation, and structural heritage on the structure and kinematics of orogenic wedges: Analog models and case studies. GSA Today 20, 4-10.

Moore, G.F., Park, J.O., Bangs, N.L., Gulick, S.P., Tobin, H.J., Nakamura, Y., Sato, S., Yoro, T., Tanaka, H., Uraki, S., Kido, Y., Sanada, Y., Kuramoto, S., Taira, A., 2009. Structural and seismic stratigraphic framework of the NanTroSEIZE Stage 1 transect. In: Structural and Seismic Stratigraphic Framework of the Nan-TroSEIZE Stage 1 Transect: Proc. IODP 314/315/316, Integrated Ocean Drilling Program Management International.

Morley, C. K., 1988. Out-of-sequence thrusts, Tectonics 7, 539-561.

Park, J.O., Tsuru, T., Kodaira, S., Cummins, P., Kaneda, Y., 2002. Splay fault branching along the Nankai subduction zone. Science 297, 1157-1160.

Seno, T., 1977. The instantaneous rotation vector of the Philippine Sea plate relative to the Eurasian plate. Tectonophysics 42, 209-226.

Shyu, J.B.H., Sieh, K., Chen, Y.G., Liu, C.S., 2005. Neotectonic architecture of Taiwan and its implications for future large earthquakes. J. geophys. Res 110.

Strasser, M., Moore, G.F., Kimura, G., Kitamura, Y., Kopf, A.J., Lallemant, S., Park, J.O., Screaton, E.J., Su, X., Underwood, M.B., 2009. Origin and evolution of a splay fault in the Nankai accretionary wedge. Nat. Geosci. 2, 648-652.

Suppe, J., 1981. Mechanics of Mountain Building and Metamorphism in Taiwan. Memoir of the Geological Society of China 4, 67-89.

Teng, L.S., 1990. Geotectonic evolution of late Cenozoic arc-continent collision in Taiwan. Tectonophysics 183, 57-76.

Wobus, C.W., Crosby, B.T., Whipple, K.X., 2006. Hanging valleys in fluvial systems: Controls on occurrence and implications for landscape evolution. Journal of Geophysical Research: Earth Surface (2003–2012) 111.

Yu, S.-B., Cheng, H.-Y., Kuo, L.-C., 1997. Velocity field of GPS stations in the Taiwan area. Tectonophysics 274, 41-59.

CHAPTER 1

Tectonic evolution of an active tectonostratigraphic boundary in accretionary wedge: An example from the Tulungwan-Chaochou Fault system, southern Taiwan

1.1 INTRODUCTION

Thrust faults, folds and tectonic cleavages, which help to maintain wedge taper, are the result of internal deformation during active mountain building (Malavieille, 2010). These structures can significantly contribute to the growth of the wedge even as the deformation front propagates forward as well-described by critical wedge theory (Dahlen, 1990; Davis et al., 1983; Suppe, 1981). For example, the growth of an antiform in the hinterland of a wedge can result from underplating (Beyssac et al., 2007; Malavieille, 2010; Sample and Fisher, 1986), and active thrust faults can define inner and outer parts of the wedge with significantly different deformation mechanisms and physical properties (Moore et al., 2009; Park et al., 2002; Strasser et al., 2009).

Here, we propose that a major thrust fault in southern Taiwan, which separates an unmetamorphosed fold-and-thrust belt from a prehnite-pumpellyite facies slate belt (Chen and Wang, 1995), is active and may be accumulating strain. Wiltschko et al. (2010) also recognized this major thrust fault and suggested that the northern segment is more active than the southern segment. In fact, it was this proposal (Wiltschko et al., 2010) that inspired us to complete a more detailed survey along the fault, particularly in the hanging wall of this major structure. It was also for this reason that we focus on late stage and generally more brittle structures. Previous studies of the ductile fabrics in the slate belt show that the dominant structure is a penetrative and consistently oriented slat cleavage. Wiltschko et al. (2010), however, identified significant

deviations from this simple pattern and suggested that there may have been a change in the state of stress over time or that part of the slate belt may have rotated as the rocks were exhumed. Our more detailed structural studies support these general ideas and provide a more complete history of the post-cleavage deformation.

Based on the earlier work by Wiltschko et al. (2010) and the results presented here, we propose that the thrust fault between the slate belt and the unmetamorphosed fold-and-thrust belt in southern Taiwan represents a major tectonostratigraphic boundary. Although there are no historical large earthquakes related to the structure, leveling data suggest that the northern segment of the boundary may be active. In this paper, we interpret the geological and structural development of this boundary and discuss the role in the deformation of the accretionary wedge.

1.2 GEOLOGIC AND PLATE TECTONIC SETTINGS OF TAIWAN

The Taiwan orogenic belt sits on the convergent boundary between the Philippine Sea and Eurasian Plates. Due to the NW-SE convergence between these plates at 82 mm per year (Yu et al., 1997) since 5 Ma (Teng, 1990), the Chinese continental margin of the Eurasian Plate has collided with the Luzon arc forming an accretionary wedge. Byrne et al. (2011) interpreted a 500 km long northeast-trending magnetic anomaly that extends from the South China Sea to central Taiwan as a proxy for the boundary between continental and transitional crusts. A northwest trending structure offsets the magnetic anomaly and Byrne et al. (2011) interpreted the structure as a northwest-trending continental margin fracture zone that has been reactivated during the arc-continental collision (Figure. 1.1), controlling many of the regional-scale geological patterns in the orogen.

There are six tectonostratigraphic units in Taiwan, four of them form the accretionary wedge and vary in structural histories and metamorphic grades. From east to west, these are the Tananao Metamorphic Complex, the Central Range slate belt, the Hsuehshan Range slate belt and the fold-and-thrust belt (Teng, 1990). The Tananao Metamorphic Complex mostly contains mica schists with minor greenstones, carbonates, and ultramafic serpentinites (Ho, 1986). The metamorphic facies of the Tananao Metamorphic Complex ranges from greenschist facies to amphibolite facies (Chen and Wang, 1995). The age of the complex is Late Paleozoic based on deformed fusuline fossils (Yen, 1953), and the complex has been

correlated with a marble unit cored beneath the Coastal Plain (Jahn et al., 1992). Both units are interpreted as metamorphosed remnants of the south Chinese continental margin. The complex is only exposed in the northern and central segments of the wedge, and the exposed width is wider in the north than in the south. The Central Range slate belt, composed of Eocene and Miocene slates, argillites, and quartzite (Ho, 1986), lies in the west of the Tananao Complex and east of Lishan Fault. The metamorphic facies in the central section of the slate belt is greenschist and prehnite pumpellyite facies to the north and south (Chen and Wang, 1995). The southernmost segment of the slate belt gradationally changes from prehnite-pumpellyite facies to unmetamorphosed sedimentary rock in the Hengchun Peninsula; the boundary of metamorphic grade is marked by a dashed line in Figure. 1.1. The slate belt of the Hsuehshan Range is only exposed in northern and central Taiwan and covers less area than the Tananao Complex and the Central Range slate belt. The belt is located west of the Lishan Fault and mostly composed of Eocene to Oligocene slates, argillites, and quartzite (Ho, 1986). Finally, the fold-and-thrust belt, which crops out west of two slate belts, is composed of sedimentary rocks that range in age from Oligocene to Pleistocene (Ho, 1986).

Figure. 1.1. Tectonostratigraphic and GPS velocity map of Taiwan modified from Lee et al. (2002) and Yu et al. (1997). Black thick solid lines are the interpreted boundary of continental crust based on magnetic anomaly and Mesozoic basement morphology, and the black thick dashed line is interpreted continental edge fracture zone (Byrne et al., 2011). The shaded area represents the continental margin magnetic anomaly (Cheng, 2004; Hsu et al., 1998). The east-west direction dashed line in the southern section of the Central Range represents the boundary between unmetamorphosed sedimentary rock (south of the line) and lower grade metamorphic rock. Three major segments of the boundary fault are shown in the southern Central Range, a = Tulungwan Fault, b = Chaochou Fault and c = Hengchun Fault. The boundary fault between the Tananao Metamorphic Complex and the Hsuehshan Range is d = Lishan Fault. Box shows the location of Figure. 1.2. Black arrows are the velocity obtained by GPS between 1990 and 1995, white arrow represents the convergent direction and rate between Philippine Sea Plate and Eurasian Plate (Yu et al., 1997). The velocity is related to the Paisha station, S01R, located in the Chinese continental margin. The velocity vectors are based on the Table 2 of Yu et al. (1997), and 95% confidence error ellipse is shown at tip of each vector. C-C' shows the location of the tomography profile of Figure. 1.13.

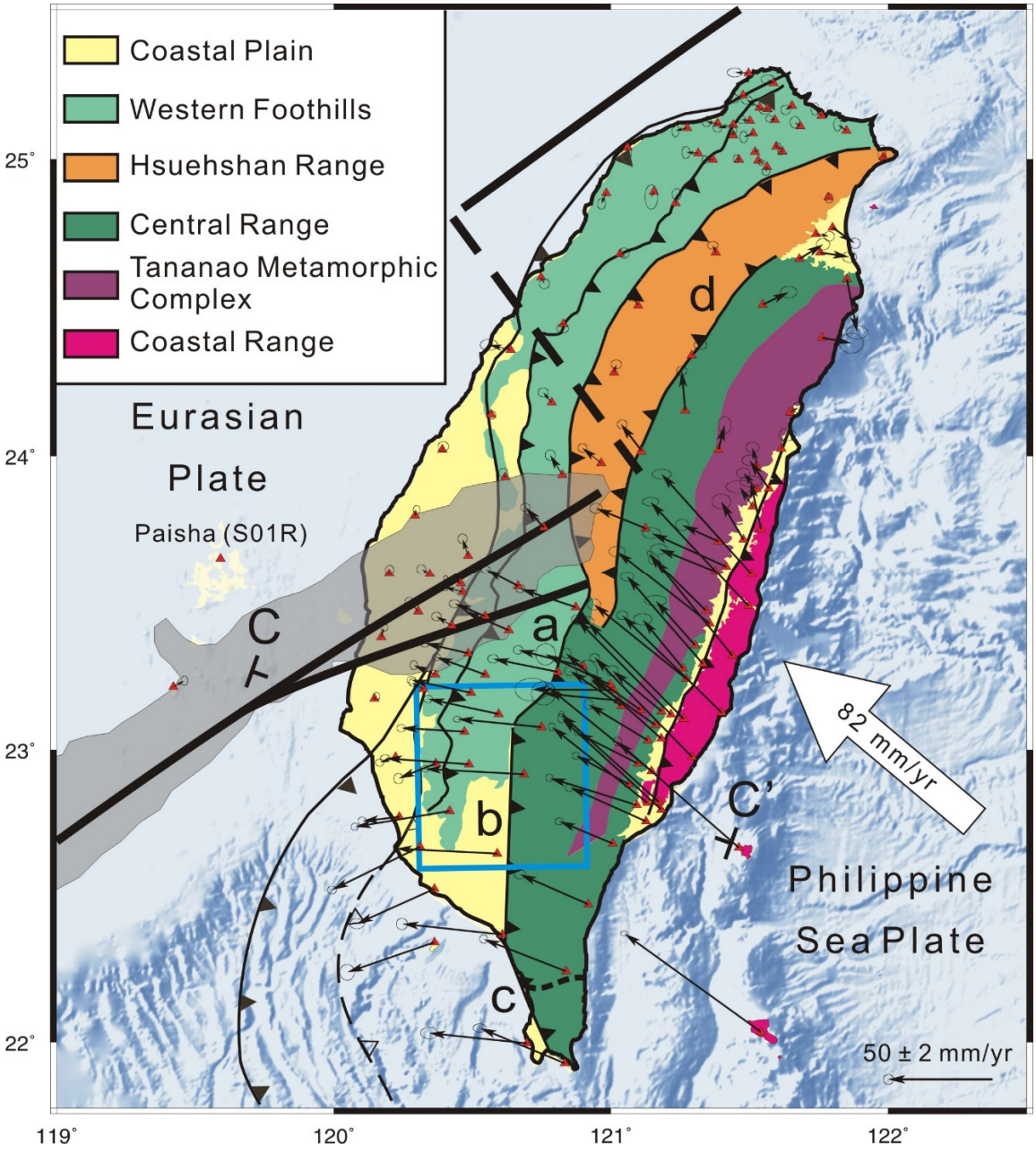
Coastal Plain
Western Foothills
Hsuehshan Range
Central Range
Tananao Metamorphic Complex
Coastal Range
Eurasian Plate
Paisha (S01R)
Philippine Sea Plate
82 mm/yr
50 ± 2 mm/yr
a
b
c
d
C
C'
25°
24°
23°
22°
119°
120°
121°
122°

1.3 GEOLOGY OF THE SOUTHERN TAIWAN

Here, we focus on the boundary between the fold-and-thrust belt and the slate belt in southern Taiwan where the orogenic belt is just emerging above sea level. The boundary between these two tectonostratigraphic units could preserve original structures that have not been overprinted by later tectonic events. In the northern part of this area, the boundary between the slate and fold-and-thrust belt trends northeast and is recognized as the Tulungwan Fault. To the south, the boundary trends north and is recognized as the Chaochou Fault. Further south, the boundary changes to a northwest trend, and is recognized as the Hengchun Fault (Figure. 1.1). In the following section, we describe the stratigraphy, structural geology and paleo-temperature of the two dominant units in the southern Central Range: the fold-and-thrust belt and the Central Range slate belt. We also elaborate on the boundary between these belts, particularly in the area of the Tulungwan and Chaochou Faults.

1.3.1. Fold-and-thrust belt

The fold-and-thrust belt in southwest Taiwan is composed of units of sandstone and shale that range in age from middle Miocene to Pleistocene. The units are separated by four major northeast striking thrusts, from foreland to hinterland, the Chukou, Chutouchi, Pinghsi and Chishan Faults (Figure. 1.2). The displacements on all the faults are generally less than 5 km with the total shortening of the four faults

ranging from 10 to 17 km (Wiltschko et al., 2010). All of the units are interpreted to have been deposited in a continental shelf environment (Sung et al., 2000). The fold-and-thrust belt of Taiwan is generally recognized to have experienced a low grade of metamorphism (Chen and Wang, 1995). Illite crystallinity data show $\Delta 2\theta$ values ranging from 0.38 to 1.26 (Chen and Wang, 1995) with paleo-temperatures converted from $\Delta 2\theta$ values based on the relation by Ji and Browne (2000), ranging from 170 to 300 °C.

1.3.2. Central Range slate belt: stratigraphy

The Central Range slate belt crops out east of the fold-and-thrust belt (Ho, 1986) and is represented by the Changshan Formation in the west and by the Pilushan Formation in the east (Ho, 1986; Sung et al., 2000). The Pilushan Formation is composed of sandstone and shale with local conglomerate and volcanic layers and ranges in age from middle to late Eocene (Ho, 1986). The Changshan Formation has been divided into two members that range in age from Middle to Late Miocene. The upper member of this formation is composed of shale with thin-bedded sandstone, basaltic pyroclastic rock and lava flows, whereas the lower member is composed of shale with thin-bedded sandstone (Chen et al., 2005; Lin, 1999; Sung et al., 2000). Both the upper and lower members have syn-sedimentary slumping structures and trace fossils that indicate deposition in an upper continental slope environment (Chen et al., 2005). The thickness of the upper member is less than 800 m and that of the lower member is unknown (Sung et al., 2000). A regional unconformity is located between the Changshan and Pilushan Formations (Ho, 1986); and the layer of

conglomerate near the unconformity could mark the base of the Changshan Formation (Chang, 1972). Both formations, which crop out east of the Tulungwan Fault, display a spaced to well-developed cleavage. The cleavage in the upper member of the Changshan Formation, however, is spaced at centimeters intervals whereas the lower member of the Changshan Formation and the Pilushan Formation have cleavages with millimeter or smaller spacing.

1.3.3. Central Range slate belt: metamorphism and low-temperature geochronology

Chen and Wang (1995) constructed a metamorphic facies map of Taiwan using illite crystallinity ($\Delta 2\theta$, shown in Figure. 1.3) and recognized prehnite-pumpellyite and greenschist facies in the slate belt of the southern Central Range; more recent fission track analyses are also consistent with these metamorphic grades (Fuller et al., 2006; Liu et al., 2001; Lock, 2007; Tsao, 1996). In general, metamorphic grade correlates with the depositional age with older rocks recording smaller $\Delta 2\theta$ values. For example, $\Delta 2\theta$ values in the Eocene Pilushan Formation are less than 0.23 suggesting temperatures of about 324 °C whereas the Miocene Changshan Formation has $\Delta 2\theta$ values between 0.23 and 0.39 indicating lower temperatures (Chen and Wang, 1995). The Changshan Formation also locally includes rocks with higher $\Delta 2\theta$ values; however, these higher grade rocks only crop out in a limited area east of the Tulungwan Fault near the Laonung River.

Figure. 1.2. Geological map of study area, modified from Chen (2000). Stratigraphy is modified from Chen (2000), Sung et al. (2000) and Wiltschko et al. (2010). Major faults are marked with numbers. 1 = Chukou Fault, 2 = Chutouchi Fault, 3 = Pinghsi Fault, 4 = Chishan Fault, 5 = Tulungwan Fault and 6 = Chaochou Fault. A-A' shows the location of cross-section. Orientations and synclines (blue lines) in the Western Foothills are adapted from geologic map of western Taiwan, Tainan sheet (CPC Corporation, 1989). Cross-section below is modified from Sung et al. (2000), and the yellow numbers are the sites of stretching lineation shown in Figure. 1.5B and C. The white anticline symbol is the inferred location of the fold axis of the slate antiform. (For interpretation of the references to color in this figure legend, the reader is referred to the web version of this article.)

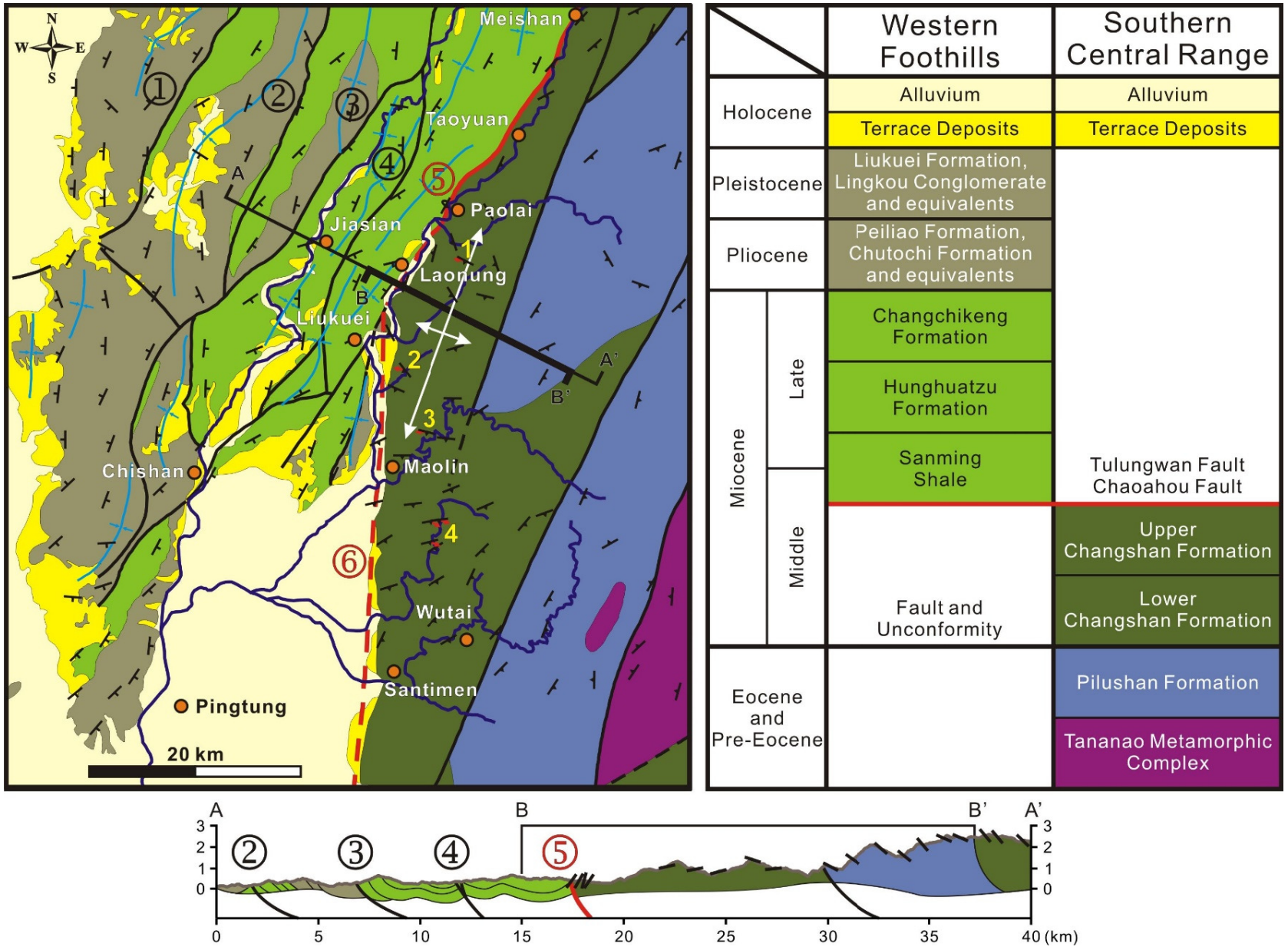
N
W
E
S
Meishan
Taoyuan
Paolai
Jiasian
Laonung
Liukuei
Chishan
Maolin
Wutai
Santimen
Pingtung
20 km
A
A'
B
B'
1
2
3
4
Western Foothills
Southern Central Range
Holocene
Alluvium
Terrace Deposits
Pleistocene
Liukuei Formation, Lingkou Conglomerate and equivalents
Pliocene
Peiliao Formation, Chutochi Formation and equivalents
Miocene
Late
Middle
Changchikeng Formation
Hunghuatzu Formation
Sanming Shale
Tulungwan Fault
Chaoahou Fault
Upper Changshan Formation
Lower Changshan Formation
Fault and Unconformity
Eocene and Pre-Eocene
Pilushan Formation
Tananao Metamorphic Complex
A
B
B'
A'
0
5
10
15
20
25
30
35
40 (km)

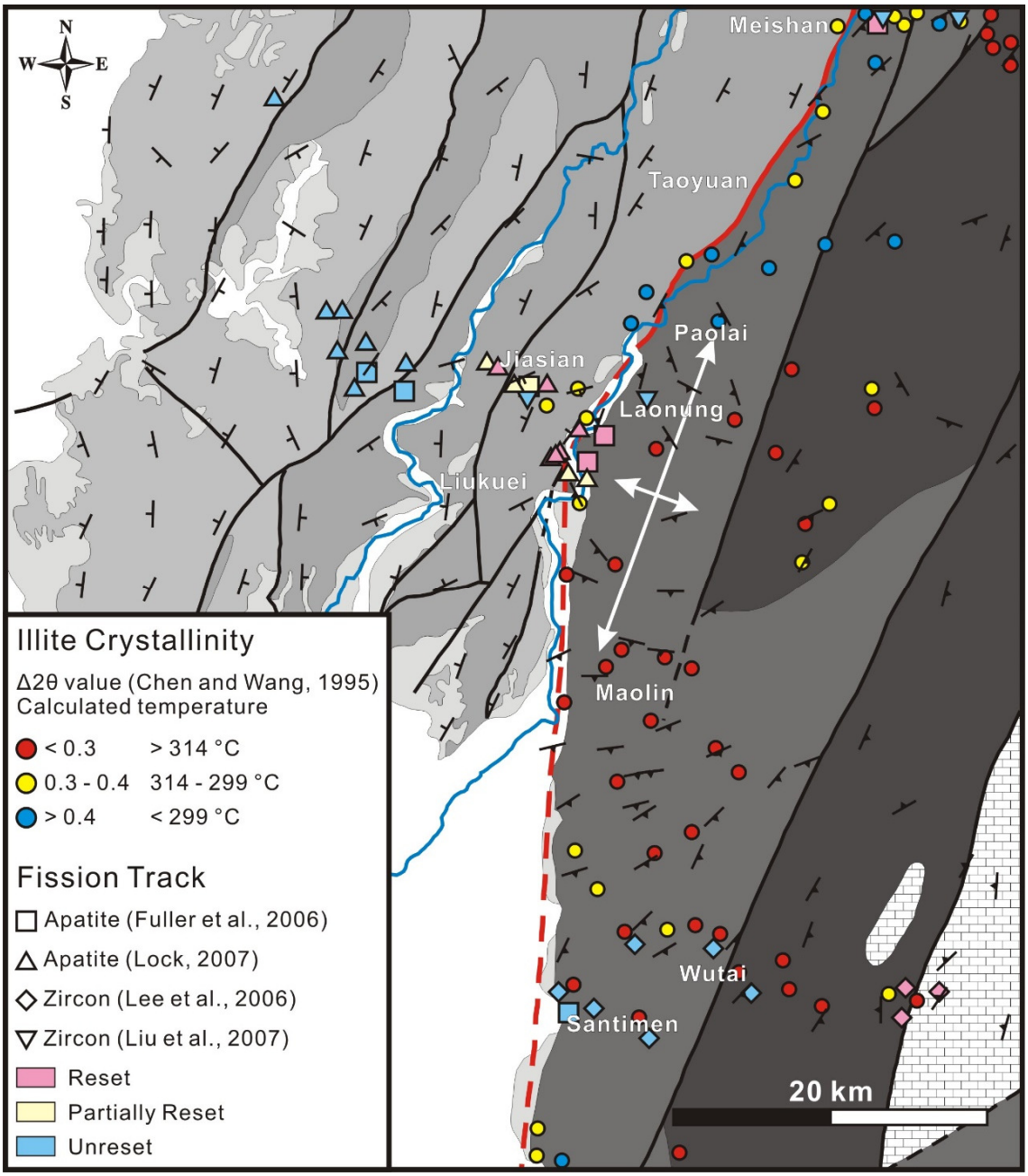

Figure. 1.3. Illite crystallinity and fission track data of study area. Illite crystallinity Δ2θ data are modified from Chen and Wang (1995), and the calculated temperature is based on the relation from Ji and Browne (2000). Apatite fission track data are modified from Fuller et al., (2006) and Lock (2007). Zircon fission track data are modified from Lee et al. (2006) and Liu et al., (2001). The lower Δ2θ values in the Changshan Formation are mainly distributed between Wutai and Laonung, and the apatite fission track data in this area are also reset, which implies more uplift in this area than the south.

1.4. STRUCTURAL GEOLOGY OF THE SOUTHERN CENTRAL RANGE

1.4.1. Regional-scale faults and fabrics

The western boundary of the southern Central Range is marked by three well-defined geomorphic lineaments generally recognized from north to south as the Tulungwan, Chaochou and Hengchun Faults (Figure. 1.1). The Tulungwan Fault in the north trends northeast and separates the fold-and-thrust belt to west from the slate belt on the east. The mapped fault generally follows the Laonung River. The Chaochou fault connects with the southern tip of the Tulungwan, but trends north-south and separates the slate belt from the flat lying Pingtung plain interpreted to be a relatively large piggy-back basin in the fold-and-thrust belt (Wiltschko et al., 2010). This segment of the fault also represents one of the most prominent geomorphic lineaments in Taiwan (Shyu et al., 2005; Yang, 1986). The southern segment of the boundary is represented by the Hengchun Fault and connects with the Chaochou Fault, but it trends more westerly, forming a second kink along the western boundary of the southern Central Range (Figure. 1.1). The differences in topography and metamorphic grade across these three faults indicate the dominance of east-side-up displacements and both the Hengchun and Chaochou Faults are associated with tilted lateritic terraces in their footwalls (Li, 2008; Shyu et al., 2005; Yang, 1986), suggesting motion in the last few hundred thousand years. An outcrop of a subsidiary branch of the Chaochou Fault also shows slate of the Changshan Formation thrust above un-lateritized fluvial deposits, consistent with recent activity (Chen et

al., 2005; Liu et al., 2009; Shyu et al., 2005; Yang, 1986). Limited GPS data across the northern Chaochou also suggests east-side-up deformation (Ching et al., 2007). Based on changes in geomorphic parameters along strike in the Central Range, Wiltschko et al. (2010) propose that the northern area reflects higher uplift rates or a longer period of uplift with constant uplift rates along strike. Illite crystallinity and fission track data also show a broad region of greater uplift in the north, near the intersection of the Tulungwan-Chaochou faults (Chen and Wang, 1995, see Figure. 1.3).

More detailed studies of river morphology, terraces and geodetic data also suggest that the Tulungwan and northern Chaochou faults may be active. For example, leveling data collected between 2000 and 2008 show relatively high rates of 12-13 mm/yr along the Laonung River where it crosses a newly recognized antiform, described in the next section (Ching et al., 2011b). Maximum calculated bedrock incision rates, based on the age of sediments above strath terraces that range in age from 1620 to 1810 BP (^{14}C dates cal. yr.), are between 18 and 19 mm/yr (Figure. 1.4; see also Figure 1.6 in Hsieh and Chyi, 2010). Horizontal GPS data (Chen, 2006) also show a maximum shortening direction perpendicular to the antiform, which strikes oblique to the Tulungwan and Chaochou Faults at acute angles. In conclusion, the Tulungwan-Chaochou-Hengchun fault system represents a major boundary in the southern Central Range, and both long-term and short-term uplift data suggest higher rates of deformation along the northern Chaochou and Tulungwan faults.

Figure. 1.4. Vertical displacement map view and profile of its rate. (A) Vertical GPS displacement contour modified from Ching et al. (2007). Detailed uplift data in the box area between Laonung and Meishan are shown in Figure. 1.4B. Bracket in the box indicates the area with more than 10 mm/yr uplift rate. (B) Vertical displacement along the Laonung River, all the vertical displacement data are projected to the line X-X' in Figure. 1.5C. The triangles show river incision rates calculated from the strath terrace during the past 50,000 years according to radiocarbon dating (Hsieh and Chyi, 2010), circles show the displacement from 2000 to 2008 measured by leveling survey (Ching et al., 2011b), and the squares are the continuous GPS stations (Ching et al., 2011b). The black bars in the displacement rate profile indicate the error of the uplift data. The doming displacement pattern of the Laonung River area suggests an active antiform in this area. (C) Vertical displacement rate profile of X-X' in Figure. 1.4B. The trend of cross section is 110°.

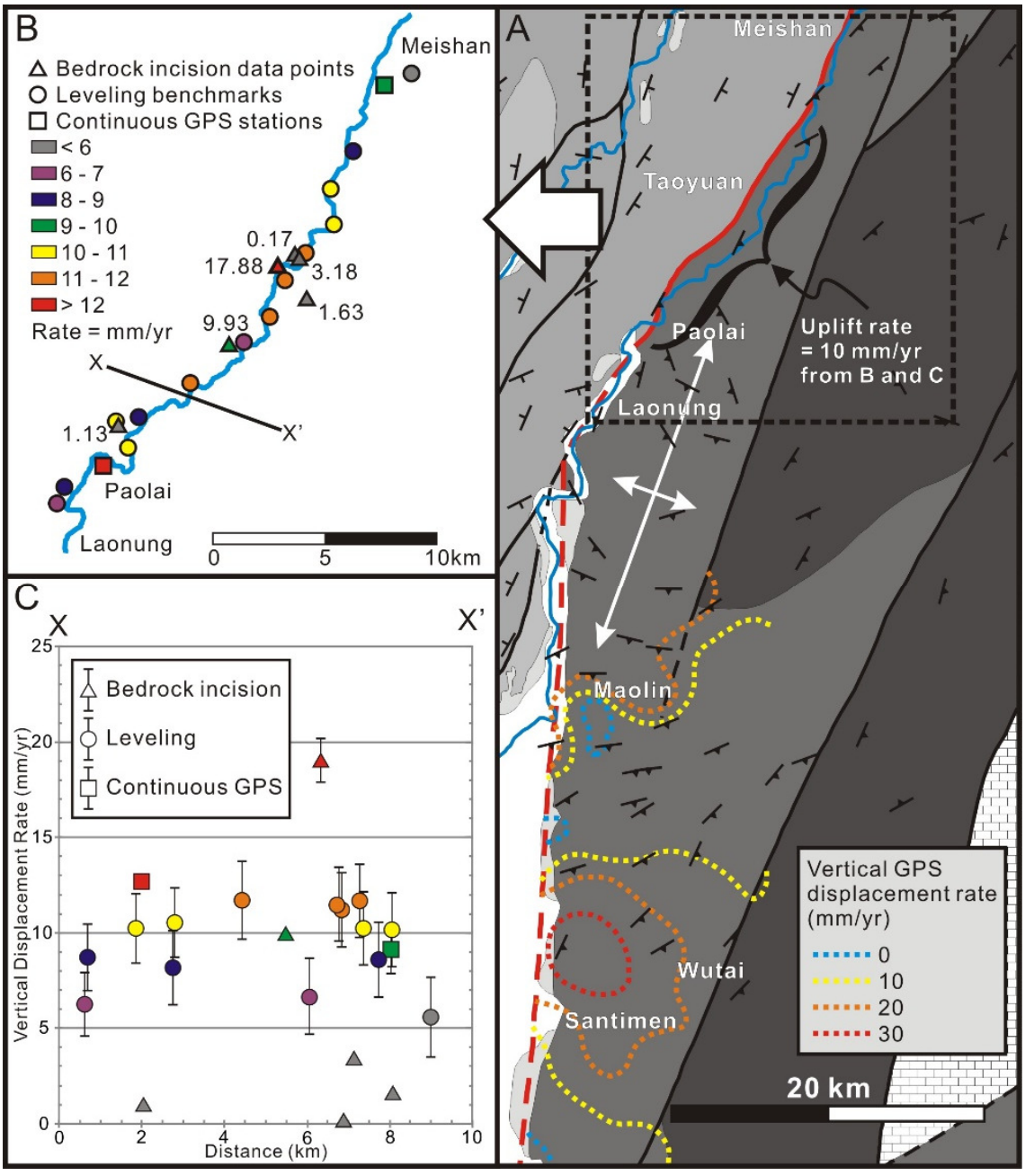
B
Bedrock incision data points
Leveling benchmarks
Continuous GPS stations
< 6
6 - 7
8 - 9
9 - 10
10 - 11
11 - 12
> 12
Rate = mm/yr
Meishan
0.17
17.88
3.18
1.63
9.93
X
X'
1.13
Paolai
Laonung
0
5
10km
C
X
X'
Bedrock incision
Leveling
Continuous GPS
Vertical Displacement Rate (mm/yr)
Distance (km)
A
Meishan
Taoyuan
Paolai
Uplift rate
= 10 mm/yr
from B and C
Laonung
Maolin
Wutai
Santimen
Vertical GPS
displacement rate
(mm/yr)
0
10
20
30
20 km

The penetrative cleavage in the hanging walls of the northern Chaochou and Tulungwan faults also displays an anomalous pattern where these two faults intersect. For example, throughout the slate belt of the Central Range the penetrative cleavage is a slaty cleavage that consistently strikes NNE and dips moderately to the ESE (Crespi et al., 1996; Fisher et al., 2007; Ho, 1986, 1995; Tillman and Byrne, 1995). In the area of the junction between the Chaochou and Tulungwan Faults, however, the cleavage forms a regional-scale antiform approximately ~45 km by ~10 km with a steep to overturned northwest limb. A Pi diagram of cleavage from the area shown in Figure. 1.5A reveals a fold axis that plunges 30° toward the SSW. The regional-scale fold therefore appears to intersect both the northern Chaochou and Tulungwan Faults at relatively low angles (Figure. 1.2).

To test the possibility that the cleavage has been folded, we used the geometry of the cleavage and an associated stretching lineation as markers and calculated the rotation axis that moves both features back to their interpreted initial orientations. Detailed and regional-scale studies of the cleavage in the slate belt of the Central Range show that the cleavage-related stretching lineation, defined by strain shadows and elongate syn-cleavage phyllosilicates, plunges consistently to the southeast (Crespi et al., 1996; Tillman and Byrne, 1995). In contrast, the stretching lineations in the area of the northern Chaochou and Tulungwan Faults show a systematic pattern with a southeast plunging lineation recorded in the east dipping limb of the antiform, consistent with the previously recognized general pattern. On the west-dipping limb, however,

the stretching lineation plunges west and southwest (Figures. 1.2 and 1.5B). If we assume that the cleavages and lineations were originally parallel, a common rotation axis can be identified by plotting the perpendicular bisectors of the great circle segments for different pairs of lineations and cleavage poles from the east and west-dipping limbs. The results show a rotation axis that plunges gently SSW, essentially parallel to the *Pi* axes defined by the cleavage poles and consistent with the interpretation that the antiform is a post-cleavage structure (Figure. 1.5C).

Identification of the post-cleavage antiform raises the question of how it formed and what structures accommodated its formation. We address how the fold formed in a later section and focus in the following section on evaluating what structures accommodated the formation of the regional-scale fold. One possibility, based on the absence of a crenulation cleavage anywhere in the field area and the relative abundance of late stage brittle faults, is that folding was accommodated by displacements on the abundant brittle faults. To evaluate this possibility we analyzed the fault kinematics of all of the faults in the field area, looking for a suite of faults consistent NW shortening and fold formation.

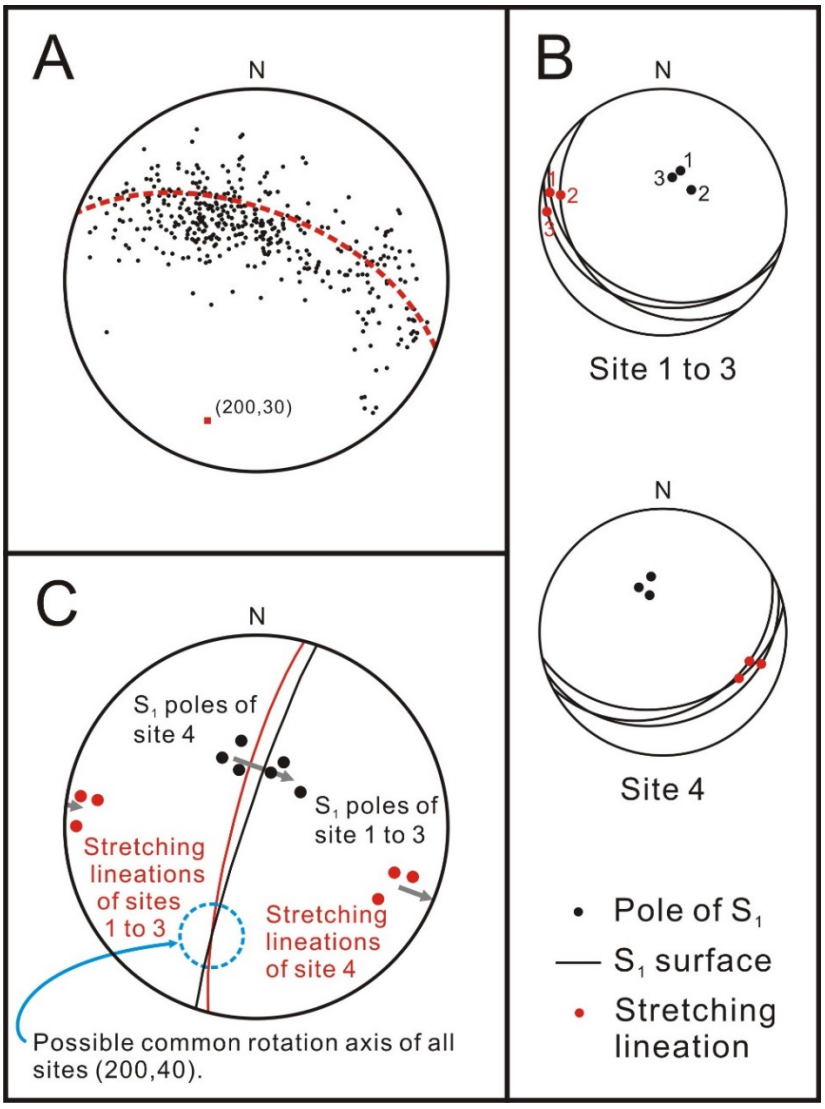

Figure. 1.5. Pi diagram of folded cleavages and stretching lineation and rotation axis of the sites. (A) Pi diagram of folded cleavage, the orientation of inferred fold axis from 404 cleavage orientations is (200, 30). (B) Stretching lineation of each site marked by yellow numbers in Figure. 1.2. (C) The rotation axis of the sites 1 to 4. The black solid line is the bisector plane of cleavage poles from sites 1 to 3 and site 4. The red solid line is the bisector plane of stretching lineations from sites 1 to 3 and site 4. Gray arrows are the tracks of rotation. Both the cleavage poles and stretching lineations rotate 20° counterclockwise, and the orientation of the rotational axis is (200, 40), which is close to the inferred fold axis of the Pi diagram. (For interpretation of the references to color in this Figure legend, the reader is referred to the web version of this article.)

1.4.2. Kinematics and paleostress of outcrop-scale faults

In mapping the slate belt in the area of the northern Chaochou and Tulungwan Faults we investigated more than three hundred outcrop-scale faults of which 250 had a defined sense of slip. We also characterized the fault damage zones and recognized two styles of deformation: 1) faults associated with a relatively ductile style of deformation and characterized by outcrop-scale folds, extension veins, laminated shear veins and "stretched" quartz fibers (Figure 1.6) and 2) faults associated with a brittle style of deformation and characterized by fault gauge, breccia and rock-on rock slickenlines (Figure. 1.7). Of the 250 faults with a known slip sense, 95 faults could be classified in one of the two above categories; 48 of the faults were classified as relatively ductile whereas 47 were classified as brittle. Cross-cutting relations of the two groups indicate that the more ductile group is older than the brittle group. In other words, the group of ductile deformation faults represents early stage faults whereas the second group represents late stage faults. Our interpretation is that older, more ductile faults formed at deeper structural levels whereas the younger faults formed at shallower levels.

We used two different methods to analyze the 250 outcrop scale faults with a known sense of slip: kinematics (or P-T axis analyses) and the Gauss stress inversion technique (Zalohar and Vrabec, 2007). The kinematic analysis is a graphical approach that uses the fault and slickenline orientations to determine the P and T axes for a group of faults using the Bingham statistical method (Marrett and Allmendinger,

1990). Each pair of P and T axes lies in a plane containing the slip vector and the normal vector to the fault plane, and make angles of 45° with each of the vectors. No interpretation is involved in the process of determining the kinematic axes of a fault from field measurements because each measurement is converted into a fault plane solution (Marrett and Allmendinger, 1990). The Gauss stress inversion is based on the direct stress inversion technique (Angelier, 1994) where the misfit between slickenlines and the representative stress tensor of a group of faults is minimized (Zalohar and Vrabec, 2007). In addition, the Gauss technique considers the normal and shear stress components on the fault (Zalohar and Vrabec, 2007). Fault populations outside of a user-defined misfit angle are removed from the data set and considered as a second, independent population of faults. The first population with a compatible stress tensor is classified as "phase 1". The second population is analyzed in the same way and resulting in a phase 2 stress tensor. Additional fault populations or phases can also be analyzed; however, we limited our analysis to phases with 10 or more faults. The Gauss stress inversion technique requires a number parameters to be defined, including Δ, $\psi 1$, $\psi 2$ and k, where Δ is the threshold value of compatibility, $\psi 1$ is the angle of internal friction, $\psi 2$ is the angle of friction for sliding on a preexisting fault, and k is the stress parameter that weights the importance of friction (Zalohar and Vrabec, 2007). The kinematic method was used to analyze 95 early and late stage faults whereas the Gauss stress inversion method was used to analyze the 95 early and late stage faults as well as the 250 faults with a known sense of slip.

Figure. 1.6. Early stage fault outcrop. The east-west striking, south dipping fault is in the pillow basalt of the upper Changshan Formation. Laminated quartz fibers indicate the fault motion is right-lateral. Outcrop is near the town of Paolai (23° 6’ 57” North, 120° 42’ 53” East).

Figure. 1.7. Late stage fault outcrop. The northeast-southwest striking, southeast dipping fault is in the lower Changshan Formation. Fragments of quartz veins can be found in the breccia which suggest the fault is a late stage structure. Rock-on-rock slickenlines indicate the fault motion is reverse. Outcrop is near the town of Meishan (23° 15’ 32” North, 120° 5’ 58” East).

The shortening direction revealed by the kinematic analysis shows a well-defined difference between the early and late stage faults. The early stage faults (Figure. 1.8A) show a shortening direction of 310° which is approximately parallel to the plate convergence direction (Yu et al., 1997) and a maximum extension direction that plunges gently northeast. Both kinematic axes are similar to axes obtained from faults in the slate belt along the South-Cross-Island-Highway area that Crespi et al. (1996) considered to have formed late in the development of the cleavage. Our observations of the early stage faults in the Laonung area are consistent with this interpretation. Kinematic analysis of the late stage faults (Figure. 1.8B) shows a shortening direction that trends 293° and a steeply plunging maximum extension direction, which is significantly different from the results from the early stage faults.

Because the number of major shortening events in the development of the faults is unknown, we also used the Gauss stress inversion method (Zalohar and Vrabec, 2007) to separate the faults into different phases and compare the results with the kinematic analysis of the two fault groups as well as with other geologic observations. We first analyzed the combined data set of 95 faults to evaluate the consistency with the kinematics of the faults identified in the field as early or late stage. We then analyzed all 250 faults with a known sense of slip.

Inversion of the 95 faults yielded three phases: Phase 1 contains 43 faults with 27 identified as early stage faults, and 16 identified as late stage faults. This phase yields a maximum shortening direction that

plunges gently 309° (Figure. 1.9A) and a maximum extension axis that plunges gently northeast. Phase 2 contains 22 faults with 11 identified as early stage faults and remaining 11 identified as late stage faults. The maximum shortening direction of the second phase is sub-horizontal and trends 083° (Figure. 1.9B) and the maximum extension axis is plunges gently north. Phase 3 contains 10 faults with 3 of the faults identified as early stage faults and 7 identified as late stage faults. The maximum shortening direction of this phase is 019° (Figure. 1.9C) and the maximum extension plunges steeply to southwest.

Based on the number of early and late stage faults in each phase, we propose the following preliminary interpretations: Phase 1, which contains a higher proportion of early stage faults, correlates with the early stage faults in the kinematic analysis. The shortening and extension directions are also similar for these two families of faults. Phase 2 contains an equal number of early and late stage faults and therefore could represent either population. Phase 3 contains a high proportion of late stage, suggesting that it may represent the late stage population recognized in the kinematic analysis. However, the shortening and extension directions are very different for this phase, suggesting that it may represent a different phase of shortening. In this context, we note that the shortening direction for this phase is similar to the maximum shortening direction of the 2010 Mw 6.3 Jia-Shian earthquake (Ching et al., 2011a; Hsu et al., 2011; Huang et al., 2011; Huang et al., 2013; Lee et al., 2013; Rau et al., 2012), suggesting that northeast-southwest shortening might play an important role in this area. The presence of phase 3 may also explain the difficulty in interpreting

phase 2 faults and the difference in the maximum shortening directions determined from phase 2 of the 95 faults using the Gauss method versus the kinematic analysis of late stage faults. That is, the kinematic method would recognize both Phase 2 and Phase 3 faults as "late stage" whereas the Gauss method recognized Phase 2 and 3 as distinct.

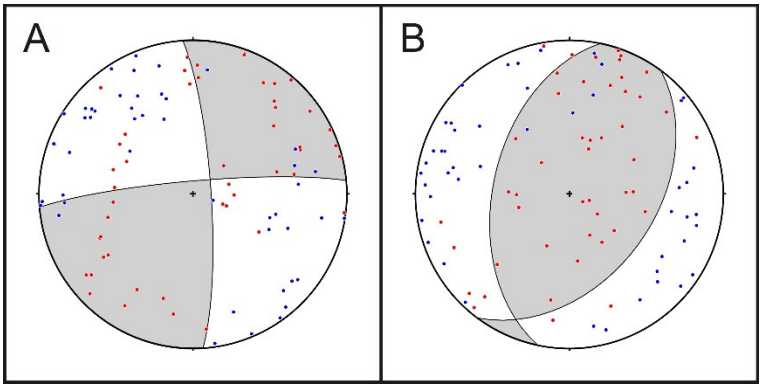

Figure. 1.8. Kinematic P and T axis analysis of field-identified early and late stage faults. Blue dots are P axis and red dots are T axis. (A) Kinematic analysis of 48 field-identified early stage faults, the shortening direction is 310°. (B) Kinematic analysis of 47 field-identified late stage faults, the shortening direction is 293°.

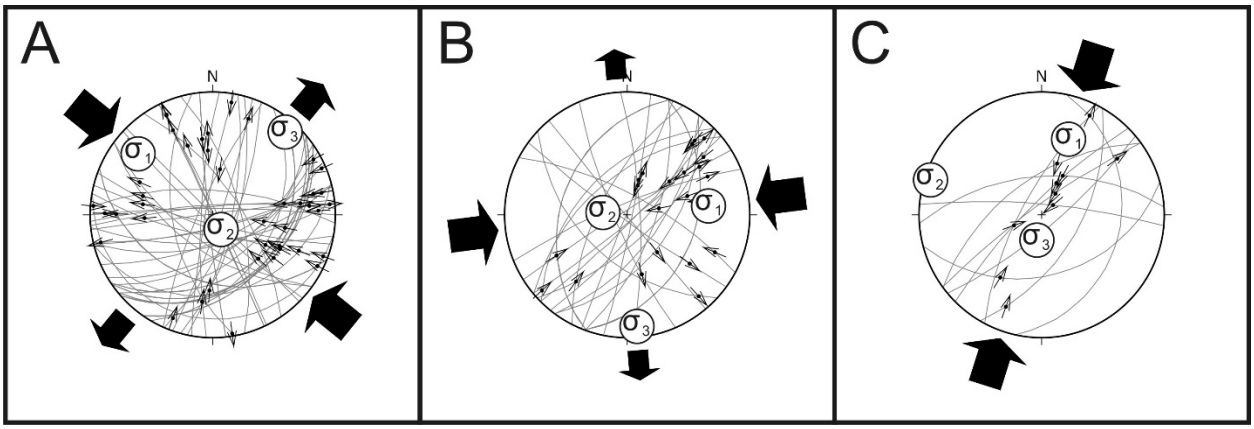

Figure. 1.9. Stress inversion of 95 field-identified early and late stage faults by the Gauss stress inversion method. Results for phase 1 (A) with a shortening direction of 309°, phase 2 (B) with a shortening direction of 083° and phase 3 (C) with a shortening direction of 019°.

After using the Gauss stress inversion to examine the 95 faults, we applied the Gauss method to all of the faults with known kinematics, including those identified as early or late based on field criteria. This larger data set of 250 faults was analyzed using the same parameters as the smaller data set and different phases were identified as possibly early or late depending on the percentage of field-identified faults included in the phase. Phase 1 contains 101 faults, 17 of them are field-identified early stage faults, 22 are field identified late stage faults and 62 faults are without age control. The maximum shortening direction of this phase plunges gently towards 285° (Figure. 1.10A) and the maximum extension direction plunges steeply to the northeast. Phase 2 contains 48 faults, 12 of which were identified as early stage faults, 6 were identified as late stage faults, and 30 faults had no age control. The maximum shortening direction of the second phase is 323° (Figure. 1.10B) and the maximum extension direction gently plunges to the southwest. Phase 3 contains 35 faults; 5 were field-identified early stage faults, 5 were field-identified late stage faults and 25 faults had no age control. The maximum shortening direction of Phase 3 is 083° (Figure. 1.10C) and the maximum extension direction is 57° plunging to the northwest. Phase 4 contains 22 faults, 1 of which was identified as an early stage fault, whereas 7 were identified as late stage faults and 14 faults had no age control. The maximum shortening direction of phase 4 is 187° (Figure. 1.10D) and the maximum extension direction steeply plunges to the west.

Taken together, the kinematic and stress analyses of the 95 faults with inferred age relations and the 250 faults with a known sense of slip suggest three stages of fault development (Table 1.1): 1) northwest-southeast shortening followed by 2) generally east- west shortening and 3) north northeast-south southwest shortening. Recognition of the three stages is based on the relative abundance of field identified early versus late stage faults in the various phases and the orientations of the shortening and extension directions in each phase (Table 1.1). The northwest shortening stage is represented by the faults identified in the field as early stage faults, by phase 1 of the fault population of 95 faults and by phase 2 of the fault population with 250 faults (Table 1.1). East-west shortening is represented by the faults identified in the field as late stage faults, by phase 2 of the fault population with 95 faults and by phases 1 and 3 of the larger fault population. Finally, north northeast-south southwest shortening is represented by phase 3 of the fault population with 95 faults and phase 4 of the larger population of faults.

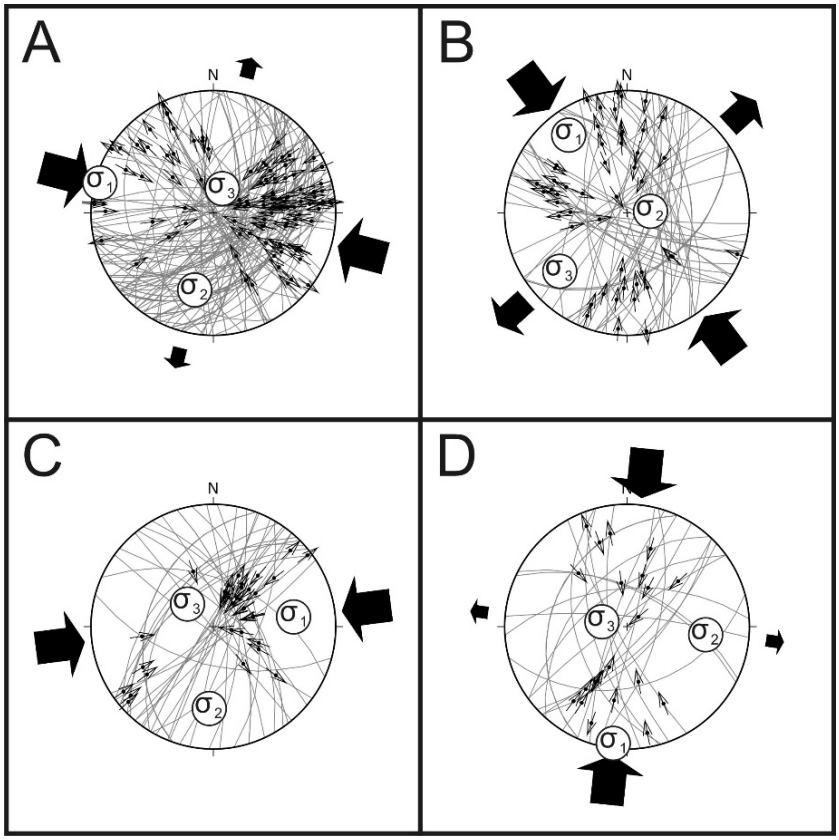

Figure. 1.10. Stress inversion of 250 faults by the Gauss stress inversion method. Results for phase 1 (A) with shortening direction of 285°, phase 2 (B) with shortening direction of 323°, phase 3 (C) with shortening direction of 083°, and phase 4 (D) with shortening direction of 187°.

Table 1.1. Results of kinematic analysis and paleostress inversion.

Faults Identified in the field as early or late (95)						Faults with sense of shear (250)		
	Kinematic Analysis		**Stress Inversion**			**Stress Inversion**		
	Num of Flts	Max Orient.	Phase	Max Orient.	Early/Late	Phase	Max Orient.	Early/Late
Early	48	310	1	309	27/16	1	285	17/22
Late	47	293	2	83	11/11	2	323	12/6
			3	19	3/7	3	83	5/5
						4	187	1/7

1.5. DEVELOPMENT OF THE REGIONAL-SCALE FOLD OF CLEAVAGE

The antiform in the Laonung River area is recognized by the orientations of cleavages in the low-grade metamorphic rocks, which, we propose, was formed as the slate belt was exhumed from depth. To better understand the formation of the antiform, we constructed a northwest-southeast trending cross-section and propose a hypothesis for the structural evolution of this area. The magnitude of east-dipping cleavages in the east end of cross-section is about 40° and changes to 25-30° dipping to the west in the middle of the cross-section. The cleavage is 50-60° west dipping in the western part of the cross-section, and a 5 km wide narrow zone near the Tulungwan Fault has nearly vertical cleavages (Figures. 1.2 and 1.11A).

To better understand the formation of the antiformal structure defined by the cleavage domains, we compared relatively simple fault-bend fold and fault-propagation fold models to the two subdomains of cleavage. For both models we assumed an initial southeast dip of 45° for the cleavage, which represents the typical orientation for cleavage in the slate belt of the Central Range. We then fixed the 45° angle between cleavage and modeled horizontal line (representing bedding in the model) and deformed both “bedding” and cleavage. The results show that the fault-bend fold model does not make the cleavage as steep as the field measurements in the forelimb (Figure. 1.11B). Although the fault-propagation fold model solves this problem, it fails to duplicate the moderately east-dipping cleavages between the forelimb and backlimb (Figure. 1.11C).

Because neither of the two fault-related fold models can satisfy the observations, we considered two folding mechanisms in sequence; an initial stage of fault-bend folding followed by trishear folding (Figure. 1.12). As shown in Figure. 1.12B the slate belt moves from the flat to the ramp, causing rotation of the cleavage, and the footwall also starts to collapse (dashed line). The dashed line represents the precursor of a thrust fault associated with the trishear fold in Figure. 1.12C, which drags the cleavage and forms a narrow zone of steep cleavage near the Tulungwan Fault. We propose that the folding mechanism then changes from fault-bend folding (above the duplex) to trishear folding. The reason for choosing trishear folding as the main mechanism for formation of the cleavage fold shown in Figure. 1.12C is because, 1) the curved displacement component (Erslev, 1991) of the trishear fold model can simulate the changing orientation of cleavage around the fold and 2) deformation in the hanging wall is concentrated in a narrow zone near the fault (Allmendinger, 1998), which is consistent with our observations (Figures. 1.11A and 1.12A). To understand the geometry of this fold, we use a numerical trishear model by Allmendinger et al. (1998) to simulate the geologic profile.

Three additional parameters in the trishear model influence the geometry of the fold: the fault dip angle, the trishear angle and the ratio between the fault tip propagation distance and the hanging wall slip distance (P/S ratio). When the fault dip and trishear angles are small (i.e., less than 45° and 90° respectively) the distance between the upper boundary of the triangle deformation zone and the overturned layer is

relatively narrow, which is consistent with the deformation zone we observe in the study area. We therefore used maximum fault dip and the trishear angles of 45° and 90°, respectively, for the model. The P/S ratio determines how rapidly the fault tip propagates relative to the slip on the fault itself (Allmendinger, 1998). In general, a fault with lower P/S ratio cuts through less strata, a fault with higher P/S ratio cuts through more strata. We suggest the P/S ratio of Tulungwan Fault in this area is low because the tip of Tulungwan Fault does not appear to have penetrated the surface because: 1) there are series of shear zones instead of one major fault observed in the Laonung River, and 2) the rock changes gradually from units of the unmetamorphosed fold-and-thrust belt to slate belt instead of a sharp boundary between the two different tectonostratigraphic units.

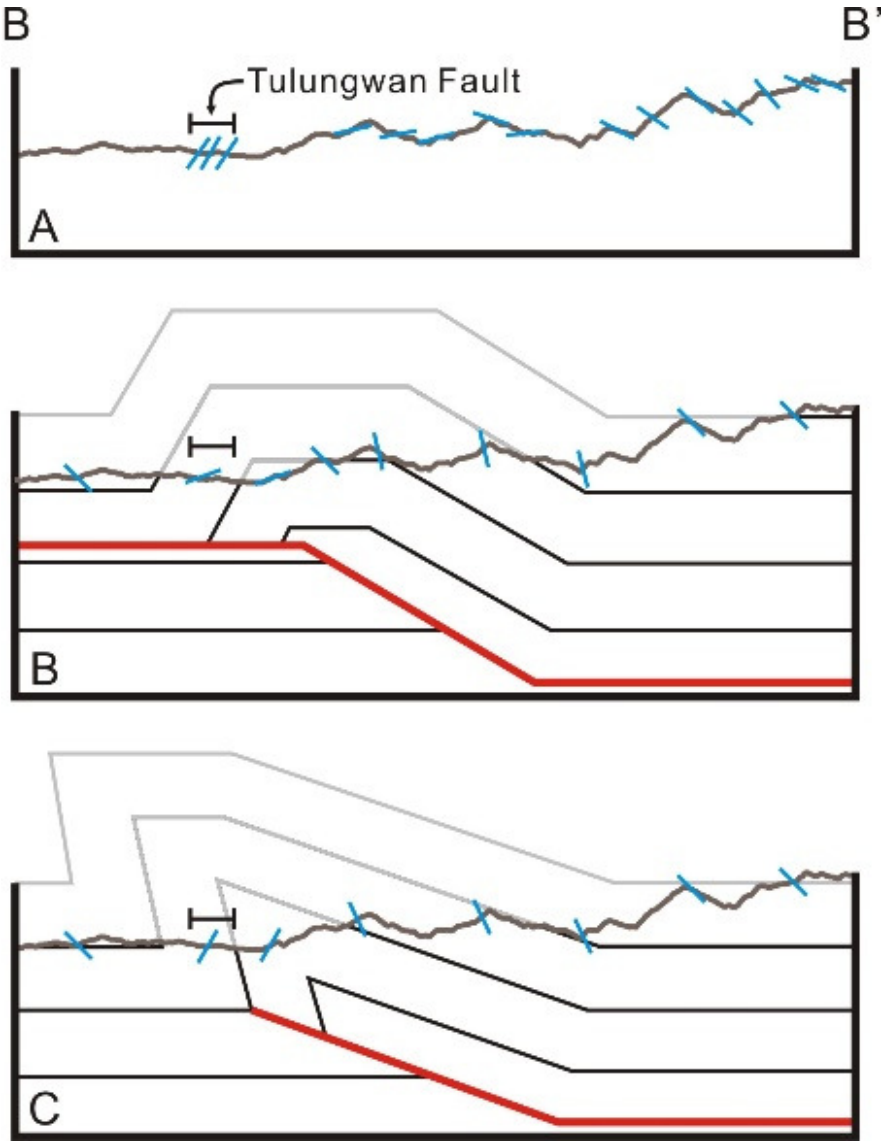

Figure. 1.11. Kinematic models for folding the cleavage. (A) Cross-section of cleavage of line B-B' in Figure. 1.2. (B) Modeled cleavage using fault bend fold model. (C) Modeled cleavage using fault propagation fold model.

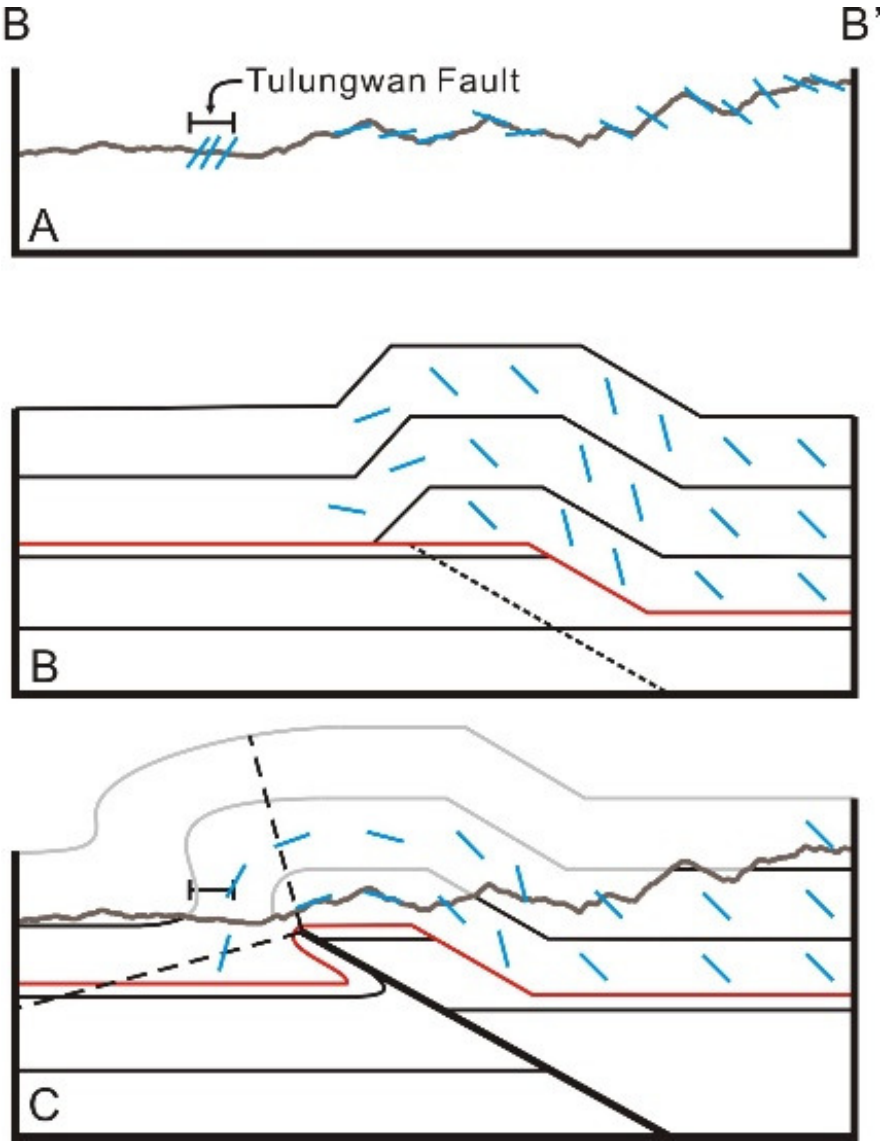

Figure. 1.12. Proposed model for the evolution of the antiform in the slate belt. (A) Cross-section of cleavage of line B-B' in Figure. 1.2. (B) The slate belt moves from the ramp (possibly representing the seaward edge of the continental margin) to the flat. Blue lines represents the slaty cleavage planes, dashed line represent the collapsed floor thrust. (C) Formation of the trishear fold. The dashed lines represent the trishear deformation triangle (90° in this case), the black solid line represents the active crustal scale fault. Note the cleavage in the Tulungwan Fault area is dragged and became high angle west dipping cleavage. (For interpretation of the references to color in this figure legend, the reader is referred to the web version of this article.)

1.6. DISCUSSION

The recognition of an active, regional-scale antiform at the junction of the northern Chaochou and Tulungwan Faults suggests that one or both of these structures may be active and possibly accumulating strain. To put the development of the cleavage antiform in regional context, we constructed a 2D crustal-scale cross-section of the P-wave velocity structure in this area of the Central Range using the "local" tomography model published by Kuo-Chen et al. (2012). The section shows a prominent inflection in P-wave velocities in the lower crust at a distance of 150 km and a smaller, more open inflection in the upper crust at 110 km (Figure. 1.13). We interpret these inflections to be inversions in the velocity structure related to thrusting and therefore draw a smooth line connecting the inflection points. To the west, the depth of the detachment beneath the fold-and-thrust belt is based on the published cross-sections (Shyu et al., 2005). The Tulungwan-Chaochou fault system is interpreted to be a splay fault originating from this regional detachment. A second splay fault is shown to the east that, in the field, places Eocene slates of the Pilushan Formation on Miocene slates of the Changshan Formation.

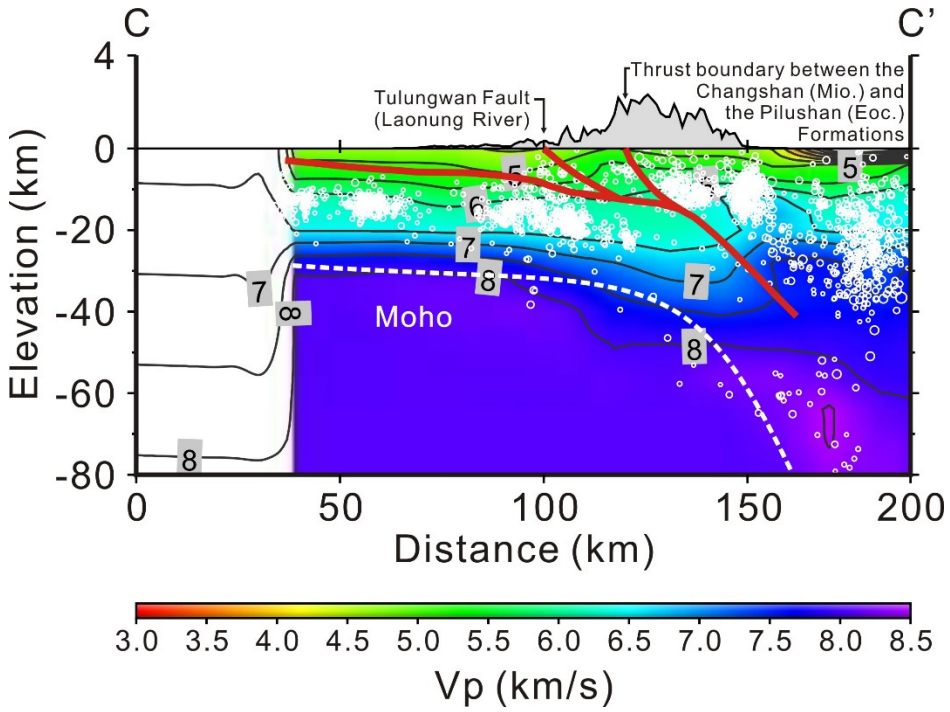

Figure. 1.13. Tomography cross section in the Laonung River area, location is line C-C' in Figure. 1.1. Red lines are the detachment fault and the splay fault. White open circles are background seismicity. The Moho surface is the white dashed line, which generally follows the 7.5 km/s contour to about the 125 km mark where it dips east 60°, following the top of the high velocity mantle (seen in the "regional" profiles of Kuo-Chen et al., 2012). The horizontal and vertical units are in kilometers. (For interpretation of the references to color in this figure legend, the reader is referred to the web version of this article.)

1.7. CONCLUSIONS

Analysis of geological, structural and geodetic data from the southern Central Range reveals a multiple deformation history of the slate belt that may still be active. The geometry of deformed cleavage shows a regional-scale antiform and paleo-stress analyses of brittle, outcrop-scale faults in the antiform area indicate a shortening direction that is approximately perpendicular to the fold axis. River incision rates and recent leveling data along the Laonung River, which crosses the east end of the antiform, suggest an uplifting dome, consistent with an active structure. We propose that the antiform is forming at the tip of a low-angle thrust, the Tulungwan-Chaochou fault system that splays from a regional scale detachment. The deformed slates identified along the Laonung River Valley may therefore represent an overturned-forelimb of the regional-scale antiform. The 2010 Mw 6.3 Jia-Shian earthquake demonstrates that this area of the slate belt has the potential for seismic deformation. However, the relation of this earthquake to the faults mapped in the seismic tomography and to the active deformation associated with the antiform remain unclear and warrant further study.

1.8. REFERENCES

Allmendinger, R.W., 1998. Inverse and forward numerical modeling of trishear fault-propagation folds. Tectonics 17, 640-656.

Angelier, J., 1994. Fault slip analysis and paleostress reconstruction. In: Continental Deformation. Pergamon Press, Oxford, pp. 53-100.

Beyssac, O., Simoes, M., Avouac, J.P., Farley, K., Chen, Y.G., Chan, Y.C., Goffe, B., 2007. Late Cenozoic metamorphic evolution and exhumation of Taiwan. Tectonics 26, TC6001.

Byrne, T., Chan, Y.C., Rau, R.J., Lu, C.Y., Lee, Y.H., Wang, Y.J., 2011. The Arce continent collision in Taiwan. In: Brown, D., Ryan, P.D. (Eds.), Arc-Continent Collision. Springer, Berlin Heidelberg, pp. 213-245.

Chang, L.S., 1972. Eocene/Miocene hiatus and N conglomerate in the Central Range of Taiwan. Proc. Geol. Soc. China 15, 93-98.

Chen, C.H., 2000. Geologic map of Taiwan. Central Geological Survey, Ministry of Economic Affairs, Taiwan scale 1:500,000.

Chen, H.I., 2006. Crustal deformation analysis of southern Taiwan: GPS observations in southern Taiwan from 1995 to 2005 (in Chinese). Master's thesis. National Cheng Kung University, p. 144.

Chen, C.H., Wang, C.H., 1995. Explanatory notes for the metamorphic facies map of Taiwan, second ed. Central Geological Survey, Ministry of Economic Affairs, Taiwan.

Chen, W.S., Chen, Y.C., Yu, N.T., Yen, I.C., Yang, B.C.C., Shih, T.S., 2005. Stratigraphic and tectonic geomorphic studies along the Chao Chou Fault, southern Taiwan-reevaluating fault characteristics and location. In: Special Publication of the Central Geological Survey, vol. 16, pp. 75-90.

Cheng, W.B., 2004. Crustal structure of the high magnetic anomaly belt, western Taiwan and its implications for continental margin deformation. Mar. Geophys. Res. 25, 79-83.

Ching, K.E., Rau, R.J., Lee, J.C., Hu, J.C., 2007. Contemporary deformation of tectonic escape in SW Taiwan from GPS observations, 1995e2005. Earth Planet. Sci. Lett.262, 601-619.

Ching, K.E., Johnson, K.M., Rau, R.J., Chuang, R.Y., Kuo, L.C., Leu, P.L., 2011a. Inferred fault geometry and slip distribution of the 2010 Jiashian, Taiwan, earthquake is consistent with a thick-skinned deformation model. Earth Planet. Sci. Lett. 301, 78-86.

Ching, K.E., Hsieh, M.L., Johnson, K.M., Chen, K.H., Rau, R.J., Yang, M., 2011b. Modern vertical deformation rates and mountain building in Taiwan from precise leveling and continuous GPS observations, 2000e2008. J. Geophys. Res. 116, B08406.

CPC Corporation, 1989. Geologic map of western Taiwan, Tainan sheet. Taiwan Petroleum Exploration Division, CPC Corporation scale 1: 100,000.

Crespi, J., Chan, Y.C., Swaim, M., 1996. Synorogenic extension and exhumation of the Taiwan hinterland. Geology 24, 247-250.

Dahlen, F.A., 1990. Critical taper model of fold-and-thrust belts and accretionary wedges. Annu. Rev. Earth Planet. Sci. 18, 55-99.

Davis, D., Suppe, J., Dahlen, F.A., 1983. Mechanics of fold-and-thrust belts and accretionary wedges. J. Geophys. Res. 88, 1153-1172.

Erslev, E.A., 1991. Trishear fault-propagation folding. Geology 19, 617-620.

Fisher, D.M., Willett, S., Yeh, E.C., Clark, M.B., 2007. Cleavage fronts and fans as reflections of orogen stress and kinematics in Taiwan. Geology 35, 65-68.

Fuller, C., Willett, S.D., Fisher, D.M., Lu, C.Y., 2006. A thermo mechanical wedge model of Taiwan constrained by fission-track thermo chronometry. Tectonophysics 425, 1-24.

Ho, C.S., 1986. A synthesis of the geologic evolution of Taiwan. Tectonophysics 125, 1-16.

Ho, S.T., 1995. Study of stratigraphy and geologic structure along the route form Santi to Chihpenchushan, south Taiwan (in Chinese). Master's thesis. National Taiwan University, p. 152.

Hsieh, M.L., Chyi, S.J., 2010. Late Quaternary mass-wasting records and formation of fan terraces in the Chen-yeo-lan and Lao-nung catchments, central-southern Taiwan. Quat. Sci. Rev. 29, 1399-1418.

Hsu, S.K., Liu, C.S., Shyu, C.T., Liu, S.Y., Sibuet, J.C., Lallemand, S., Wang, C., Reed, D.L., 1998. New gravity and magnetic anomaly maps in the Taiwan-Luzon region and their preliminary interpretation. Terr. Atmos. Ocean. Sci. 9, 509-532.

Hsu, Y.J., Yu, S.B., Kuo, L.C., Tsai, Y.C., Chen, H.Y., 2011. Coseismic deformation of the 2010 Jiashian, Taiwan earthquake and implications for fault activities in southwestern Taiwan. Tectonophysics 502, 328-335.

Huang, H.H., Wu, Y.M., Lin, T.L., Chao, W.A., Shyu, J.B.H., Chan, C.H., Chang, C.H., 2011. The preliminary study of the 4 March 2010 Mw 6.3 Jiasian, Taiwan earthquake sequence. Terr. Atmos. Ocean. Sci. 22, 283-290.

Huang, M.H., Dreger, D., Bürgmann, R., Yoo, S.H., Hashimoto, M., 2013. Joint inversion of seismic and geodetic data for the source of the 2010 March 4, Mw 6.3 Jia-Shian, SW Taiwan, earthquake. Geophys. J. Int. 193, 1608-1626.

Jahn, B., Chi, W., Yui, T., 1992. A late Permian formation of Taiwan (marbles from Chia-Li Well No. 1): Pb-Pb isochron and Sr isotopic evidence, and its regional geological significance. J. Geol. Soc. China 35, 193-218.

Ji, J., Browne, P.R.L., 2000. Relationship between illite crystallinity and temperature in active geothermal systems of New Zealand. Clays Clay Minerals 48, 139-144.

Kuo-Chen, H., Wu, F.T., Roecker, S.W., 2012. Three-dimensional P velocity structures of the lithosphere beneath Taiwan from the analysis of TAIGER and related seismic data sets. J. Geophys. Res. Solid Earth 117, B6.

Lee, J.C., Chu, H.T., Angelier, J., Chan, Y.C., Hu, J.C., Lu, C.Y., Rau, R.J., 2002. Geometry and structure of northern surface ruptures of the 1999 Mw=7.6 Chi-Chi Taiwan earthquake: influence from inherited fold belt structures. J. Struct. Geol. 24, 173-192.

Lee, Y.H., Chen, C.C., Liu, T.K., Ho, H.C., Lo, W., Lu, H.Y., 2006. Mountain building mechanism in southern Central Range of Taiwan orogenic belt e from accretionary wedge deformation to arc-continental collision. Earth Planet. Sci. Lett. 252, 413-422.

Lee, S.J., Mozziconacci, L., Liang, W.T., Hsu, Y.J., Huang, W.G., Huang, B.S., 2013. Source complexity of the 4 March 2010 Jiashian, Taiwan, Earthquake determined by joint inversion of teleseismic and near field data. J. Asian Earth Sci. 64, 14-26.

Li, P.N., 2008. Neotetonics of Hengchun area, southern Taiwan (in Chinese). Master's thesis. National Taiwan University, p. 92.

Lin, W.H., 1999. On the Laonunghsi fault e a boundary fault between the Paleogene and the Neogene strata, southern Taiwan. Bull. Central Geol. Surv. 12, 1-24.

Liu, T.K., Hsieh, S., Chen, Y.G., Chen, W.S., 2001. Thermo-kinematic evolution of the Taiwan oblique-collision mountain belt as revealed by zircon fission track dating. Earth Planet. Sci. Lett. 186, 45-56.

Liu, Y.C., Chen, P.T., Huang, C., Yen, I.C., Lu, S.T., 2009. Resent survey results of Chaochou fault. Annu. Rep. Central Geol. Surv. 2008, 35-36.

Lock, J., 2007. Interpreting low-temperature thermo chronometric data in fold-and-thrust belts: an example from the Western Foothills, Taiwan. Ph.D. thesis. University of Washington, p. 196.

Malavieille, J., 2010. Impact of erosion, sedimentation, and structural heritage on the structure and kinematics of orogenic wedges: analog models and case studies. GSA Today 20, 4-10.

Marrett, R., Allmendinger, R.W., 1990. Kinematic analysis of fault-slip data. J. Struct. Geol. 12, 973-986.

Moore, G.F., Park, J.O., Bangs, N.L., Gulick, S.P., Tobin, H.J., Nakamura, Y., Sato, S., Yoro, T., Tanaka, H., Uraki, S., Kido, Y., Sanada, Y., Kuramoto, S., Taira, A., 2009. Structural and seismic stratigraphic framework of the NanTroSEIZE Stage 1 transect. In: Structural and Seismic Stratigraphic Framework of the Nan-TroSEIZE Stage 1 Transect: Proc. IODP 314/315/316, Integrated Ocean Drilling Program Management International.

Park, J.O., Tsuru, T., Kodaira, S., Cummins, P., Kaneda, Y., 2002. Splay fault branching along the Nankai subduction zone. Science 297, 1157-1160.

Rau, R.J., Lee, J.C., Ching, K.E., Lee, Y.H., Byrne, T.B., Chen, R.Y., 2012. Subduction-continent collision in southwestern Taiwan and the 2010 Jiashian earthquake sequence. Tectonophysics 578, 107-116.

Sample, J.C., Fisher, D.M., 1986. Duplex accretion and underplating in an ancient accretionary complex, Kodiak Islands, Alaska. Geology 14, 160-163.

Shyu, J.B.H., Sieh, K., Chen, Y.G., Liu, C.S., 2005. Neotectonic architecture of Taiwan and its implications for future large earthquakes. J. Geophys. Res. 110, B8.

Strasser, M., Moore, G.F., Kimura, G., Kitamura, Y., Kopf, A.J., Lallemant, S., Park, J.O., Screaton, E.J., Su, X., Underwood, M.B., 2009. Origin and evolution of a splay fault in the Nankai accretionary wedge. Nat. Geosci. 2, 648-652.

Sung, Q., Lin, C.W., Lin, W.H., Lin, W.C., 2000. Explanatory text of the geologic map of Taiwan, Chiahsien. Central Geological Survey, Ministry of Economic Affairs.

Suppe, J., 1981. Mechanics of mountain building and metamorphism in Taiwan. In: Memoir of the Geological Society of China, vol. 4, 67-89.

Teng, L.S., 1990. Geotectonic evolution of late Cenozoic arc-continent collision in Taiwan. Tectonophysics 183, 57-76.

Tillman, K.S., Byrne, T.B., 1995. Kinematic analysis of the Taiwan slate belt. Tectonics 14, 322-341.

Tsao, S., 1996. The geological significance of illite crystallinity, zircon fission-track ages and K-Ar ages of metasedimentary rocks of the Central Range (in Chinese). Ph.D. thesis. National Taiwan University, p. 272.

Wiltschko, D.V., Hassler, L., Hung, J.H., Liao, H.S., 2010. From accretion to collision: motion and evolution of the Chaochou Fault, southern Taiwan. Tectonics 29 (2).

Yang, G.S., 1986. A geomorphological study of active faults in Taiwan: Especially on the relation between active faults and geomorphic surfaces (in Chinese). Ph. D. thesis. Chinese Culture University, p. 178.

Yen, T., 1953. On the occurrence of the late Paleozoic fossils in the metamorphic complex of Taiwan. Bull. Geol. Surv. Taiwan 4, 23-26.

Yu, S.B., Cheng, H.Y., Kuo, L.C., 1997. Velocity field of GPS stations in the Taiwan area. Tectonophysics 274, 41-59.

Zalohar, J., Vrabec, M., 2007. Paleostress analysis of heterogeneous fault-slip data: the Gauss method. J. Struct. Geol. 29, 1798-1810.

CHAPTER 2

Tectonic foliation and landslide distribution in an active orogen, example from the southern Central Range

2.1 INTRODUCTION

Landslides can be triggered by earthquakes, strong rainfall, or snow melting (Wieczorek, 1996). The distribution of landslides in a particular area, however, can also be influenced by the local strength of the rocks or geological structures (Chen et al., 2009; Guzzetti et al., 2008). For example, steep hill slopes are more susceptible to failure even in the absence of external events. Slopes that are parallel to a plane within any coherent rock like bedding or other planner structures, defining a dip slope, can also make catastrophic landslides (Chang et al., 2005; Chen et al., 2005a; Hung, 2000; Tang et al., 2009).

Typically, dip slope failure is caused by the failure of a weak bedding surface in sedimentary rock layers, however, any planner geological structure within a rock may induce failure (Chigira, 1992). In this study, we demonstrate that tectonic foliation plays an important role in slope failure similar to weak bedding planes in a sedimentary rock.

To understand how tectonic foliation influences dip slope failure, we compiled data from the southern Central Range of Taiwan where this area has 1) good coverage of structure fabric measurements, 2) abundant landslides caused by heavy rainfall, and 3) a series of aerial photos and satellite images taken for the purpose of landslide mapping.

Beside hill slope and precipitation, here, we propose that the tectonic foliation is another factor that influences the distribution of landslides in the slate region of the southern Central Range. In the two major

rock units in the southern Central Range: slate and schist, landslides tend to occur in the dip slope area in the slate region and tend to occur in the scarp slope area in the schist region. We propose that the landslide pattern is a result of different anisotropies in rocks with different degrees of metamorphism. Slate has a better developed anisotropy which appears to provide a weaker failure plane compared to the schist, so the dip slope failure is more common in the slate region of the southern Central Range of Taiwan.

2.2 STUDY AREA AND GEOLOGICAL SETTING

The southern Central Range represents the southern extent of the Taiwan arc-continental collision, which sits on a convergent boundary between Philippine Sea and Eurasian Plates with a relatively high convergence rate of 82 mm per year since 5 Ma (Teng, 1990; Yu et al., 1997, see Figure 2.1). There are two tectonostratigraphic units in the study area that can be divided into three rock units. These are: the Tananao Metamorphic Complex which is composed of pre-Tertiary schist, and the Central Range slate belt which is composed of Eocene and Miocene slate sub-belts. The Eocene slate belt crops out on the east and west of the schist, whereas the Miocene slate encompasses both the Eocene slate and the schist (Ho, 1986. see Figure 2.2).

The three rock units have different degrees of cleavage devolvement. The Miocene slate has the lowest peak metamorphic temperature of the three units and the cleavage in this unit changes from north to south. The cleavage in the northern part of the Miocene slate has penetrative cleavage and the southern part of the slate has mostly pencil cleavage (Chen et al., 2005b; Lin, 1999; Sung et al., 2000). The Eocene slate has well-developed penetrative cleavage, and includes relatively thick meta-sandstones and meta-conglomerates (Ho, 1986). The Eocene slate occupies most of the ridge crest in the southern Central Range, which suggests that the rock strength is the highest of the three units. The schist belt is located east of the ridge crest and has multiple cleavages, including a late crenulation cleavage that generally dips to the

northwest, which is opposite the dip direction of the cleavage in the adjacent Eocene and Miocene slate units to the west.

The geometry of tectonic foliation in the study area can be grouped into three major groups by their dip directions: northwest, southeast, and other (Figure 2.3). The northwest dipping domain is mainly distributed east of the ridge crest, including the schist and Eocene slate. The southeast dipping domain is mainly distributed west of the ridge crest and the southern part of the study area, including Eocene and Miocene slate. The geometry of the tectonic foliation in these two domains has been described as a fanning structure, and could be a result of post-cleavage deformation (Crespi et al., 1996; Fisher et al., 2007). The third domain, contains a variety of dips and occurs in the southern part of the field area where the metamorphic grade is relatively low and a penetrative cleavage is poorly developed.

The study area is 4795.4 km^2 and covers all the southern Central Range south of the South-Cross-Island-Highway (SXIH). The ridge crest runs approximately north-south to the south of Mt. Guan (highest peak in the study area at 3,668 m) and then turns to northeast-southwest north of Mt. Guan (Figure 2.4).

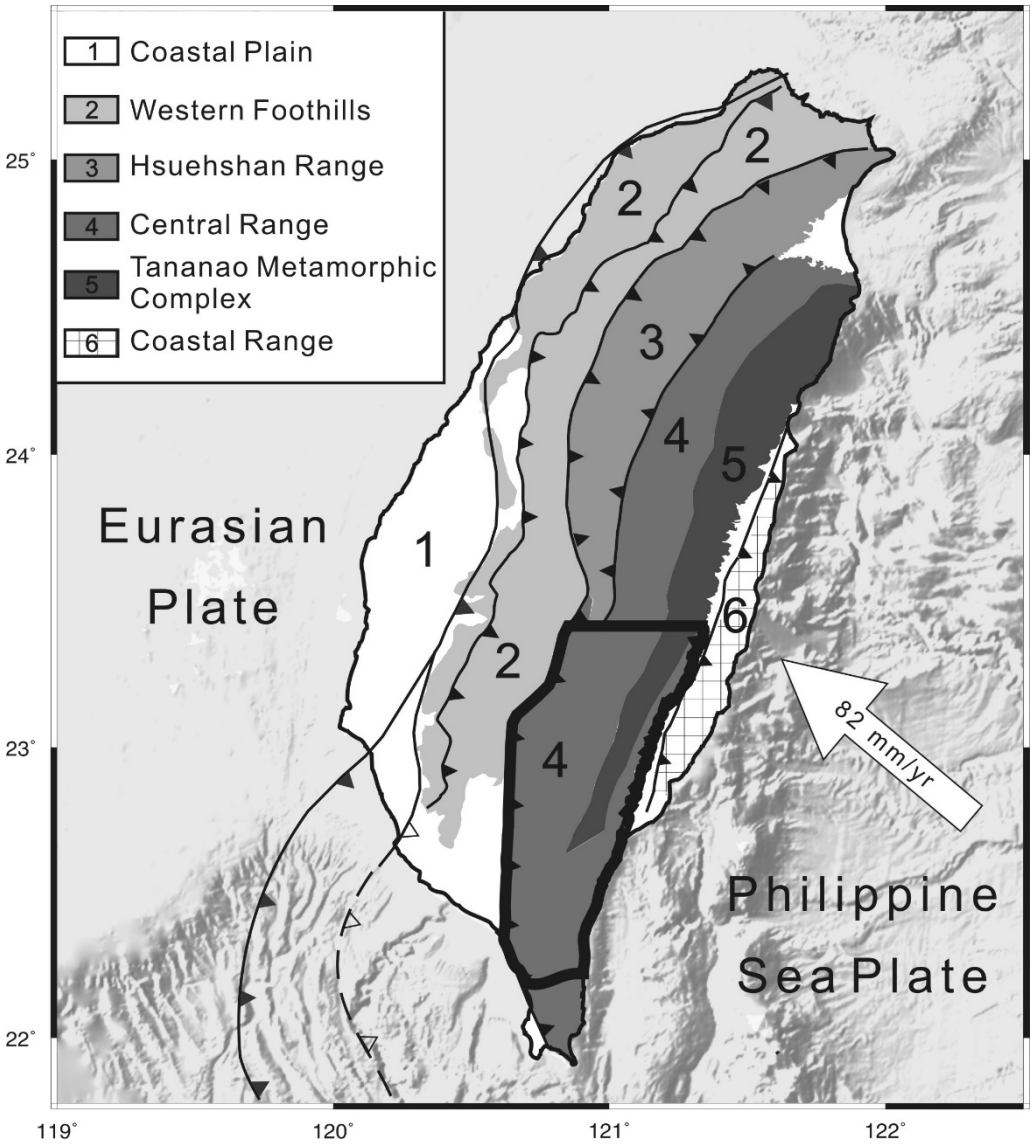

Figure 2.1. Tectonostratigraphic of Taiwan modified from Lee et al. (2002). The numbers represent different tectonostratigraphic units. 1 = Coastal Plan; 2 = Western Foothills; 3 = Hsuehshan Range; 4 = Central Range; 5 = Tananao Metamorphic Complex; 6 = Coastal Range. The Central Range is composed of slate and other lower grade metamorphic rock, and the Tananao Metamorphic Complex is mostly composed of schist. The solid line outlined the study area in the following figures. The white arrow represents the convergent direction and rate between Philippine Sea Plate and Eurasian Plate (Yu et al., 1997). The velocity is related to the Paisha station, S01R, located in the Chinese continental margin.

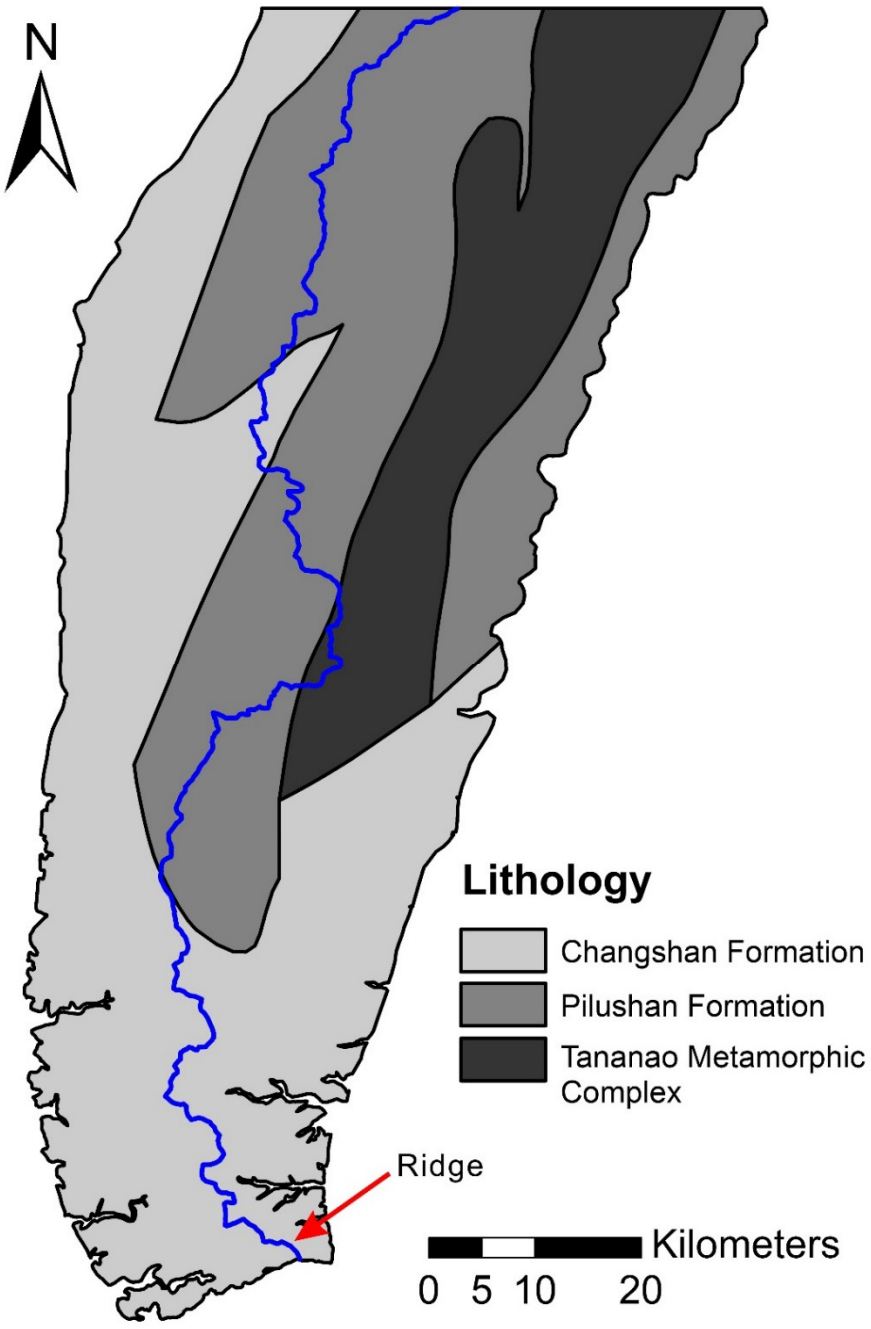

Figure 2.2. Geological map of study area modified from Chen (2000). The slate region contains Changshan Formation (Miocene slate) and Pilushan Formation (Eocene slate). The schist region contains Tananao Metamorphic Complex, which is pre-Tertiary schist. The ridge crest is marked by blue line.

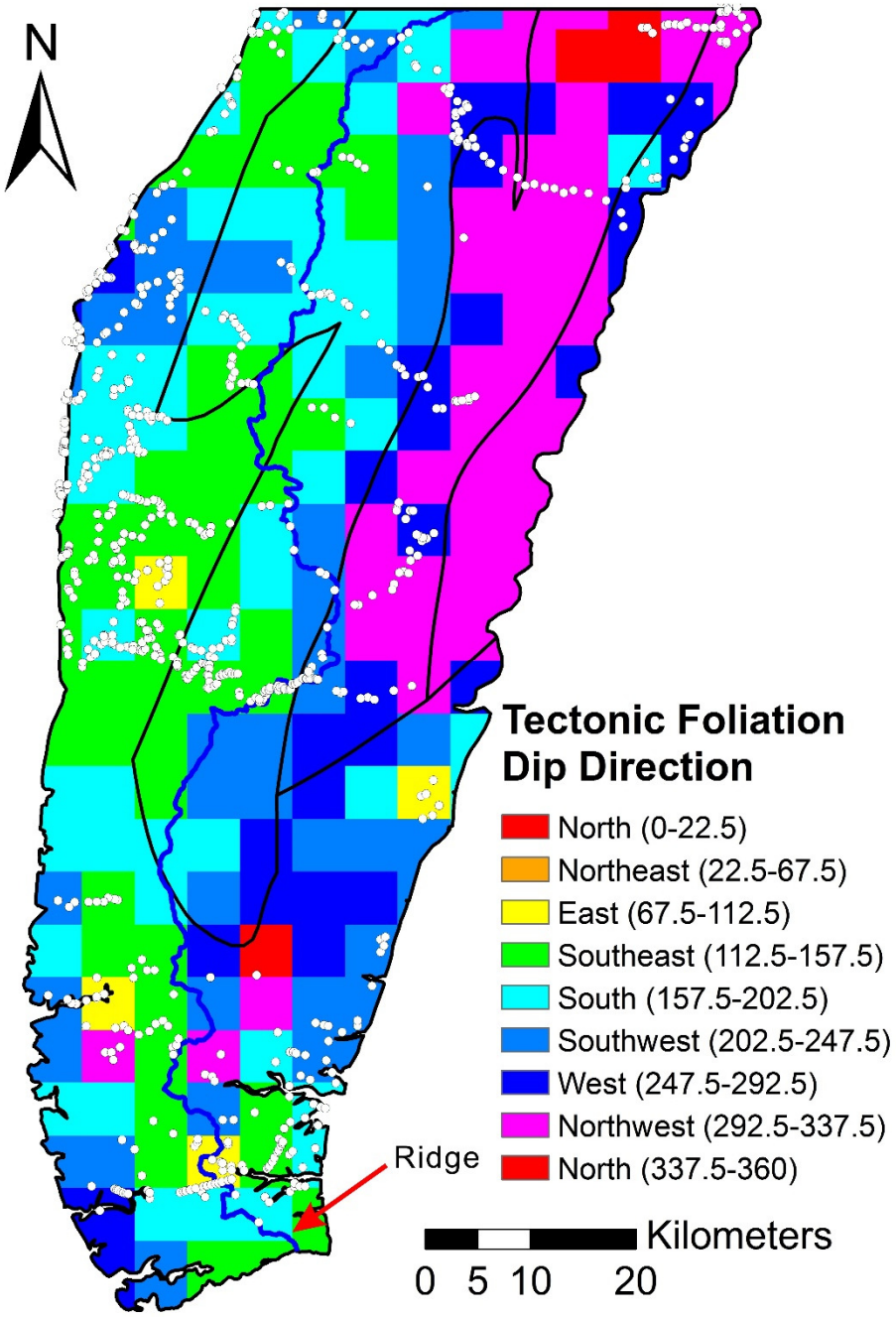

Figure 2.3. Map of dip direction of tectonic foliation. White circles are the cleavage measurement data locations. Note the foliation in the schist region and a strip of slate east of schist is mostly dip to the east. The slate west of schist is mostly dip to south and southeast, and the slate south of the schist is mostly dip to southwest to west.

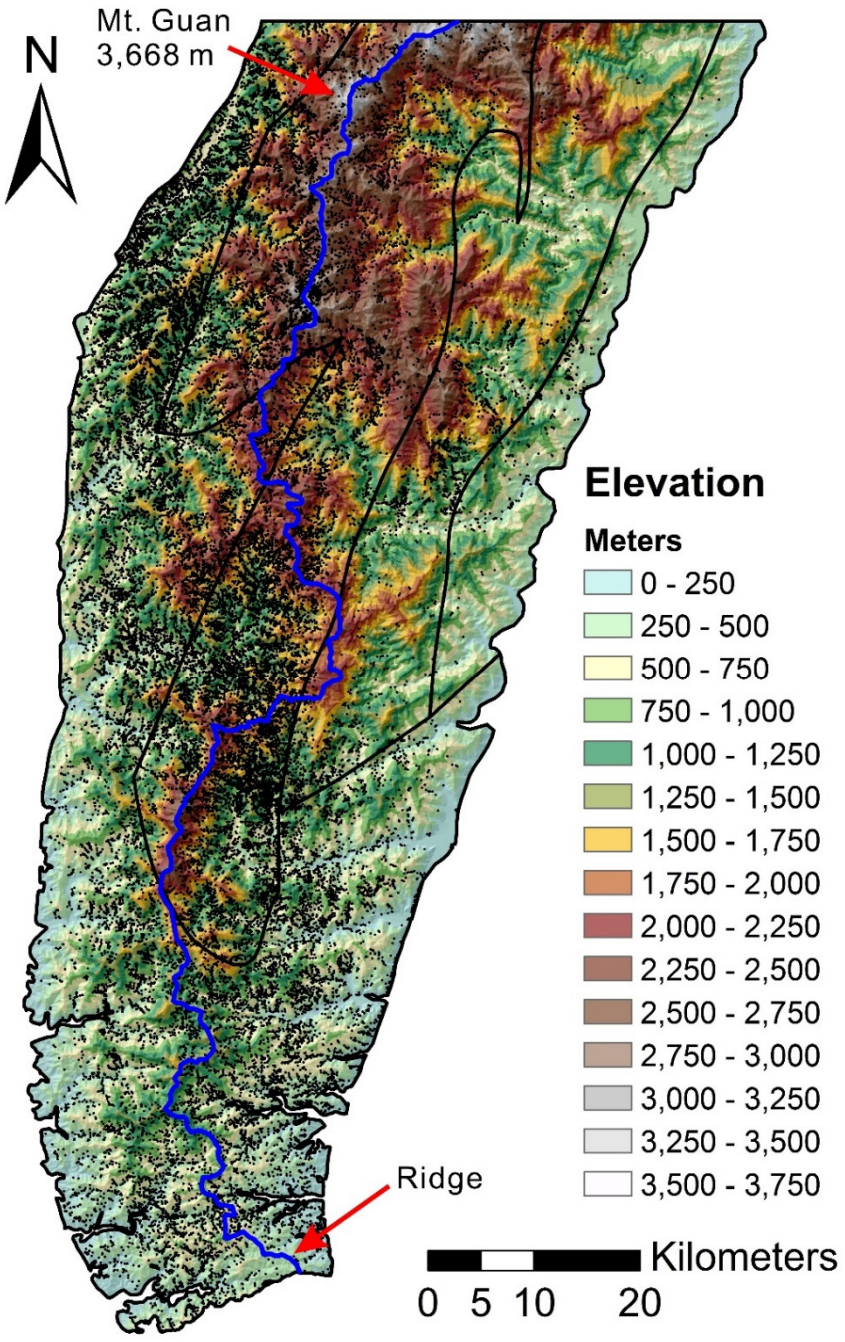

Figure 2.4. Map of elevation and landslide centroid location. There are 38,686 landslides in the study area, 36,664 landslides are in the slate region and 2,022 landslides in the schist region. The highest peak in the study area is the Mt. Guan, which is 3,668 meters in height.

The Central Geological Survey of Taiwan has recognized 38,686 landslides in the study area, with 36,664 of these occurring in the slate and 2,022 in the schist. A log-log plot with $10^{0.2}$ bin width of the landslides in the field area (Figure 2.5) shows the size distribution of landslides in both areas. The smallest landslide in the slate units is 103 m^2 and the largest is 1,296,984 m^2; while the smallest landslide in the schist is 123 m^2 and largest is 889,252 m^2. Both of the plots show the landslide density decreases at 630 m^2, which is similar to a post-Morakot landslide size distribution plot of southern Taiwan by Lin et al. (2011a). These distributions are also similar to the distribution of landslides triggered by different events around the world (Malamud et al., 2004). Both of the studies show similar pattern and the landslide area of the highest probability of landslide is located near 600 m^2. This result suggests the different lithological units in southern Taiwan might not influence the size of landslide, and that the landslide pattern is similar to the other areas in the world.

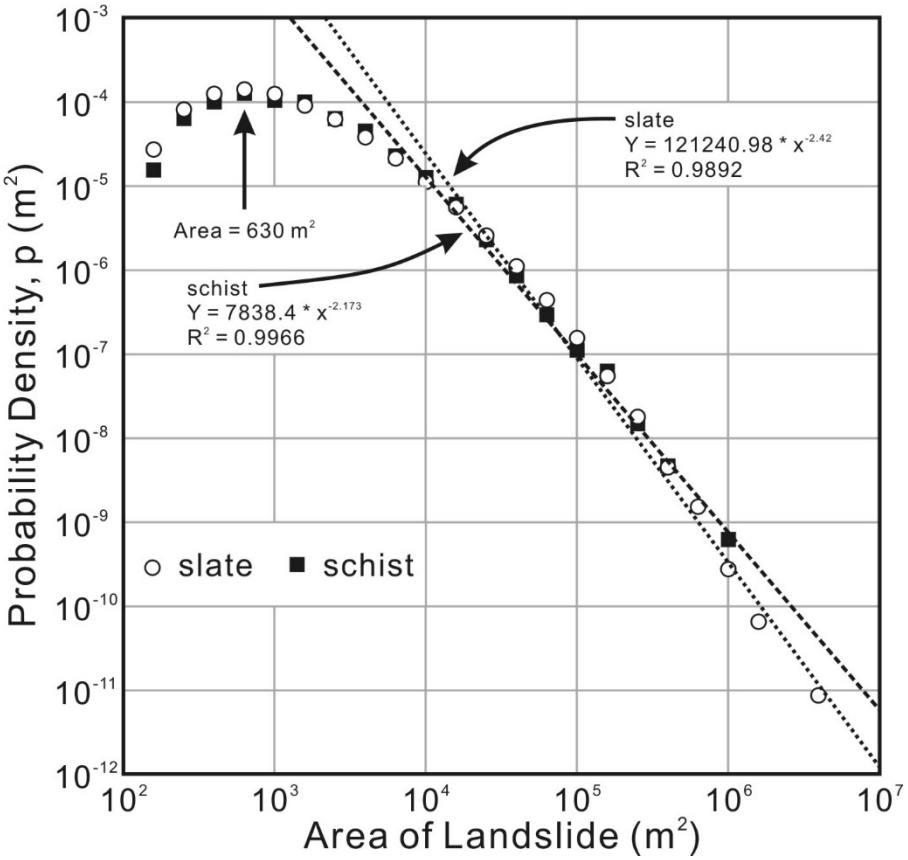

Figure 2.5. Landslide probability density plot. The power law fit equation of slate and schist are similar, and both of the coefficient of determination are close to 1.

2.3 METHOD

The landslides analyzed in this study are from a landslide catalog made by the Central Geological Survey of Taiwan. The coverage of this catalog is island wide and contains landslide polygons, a method used to identify landslides via aerial photos or satellite image, determine their areas in m^2, and document the coordinates of the centroid point of each landslide (Central Geological Survey, 2013). The resolution of the aerial photos is 50cm, and 8m for satellite images. The satellite images were taken by the FORMOSAT-2 satellite which carries multispectral sensor covering wavelength from visible to near-infrared (Lin et al., 2011a). The landslides are manually selected by identifying the non-vegetated areas in the aerial photos and by using normalized difference vegetation index (NDVI) method (Central Geological Survey, 2013) to determine the non-vegetated areas in the satellite images.

The aerial photos and satellite images in the study area were taken at two different times: before and after the typhoon Morakot which arrived in Taiwan on 8 August 2009. The aerial photos in the northeastern part of slate region were taken before typhoon Morakot, the photos in the western and southern area of the slate were taken after typhoon Morakot, and the aerial photos in the schist region were taken before the typhoon Morakot. There are some areas in the southern Central Range were not covered by aerial photos, so the Central Geological Survey use satellite images that were taken after typhoon Morakot to cover those areas.

To understand the relation between the distribution of landslides and dip-slope, we compared the hill slope direction with cleavage dip direction at the centroid point location of each landslide inventoried. In this study, we use θ_D to define the angle between the direction of hill slope and the direction of cleavage dip. The hill slope direction is calculated from a 40m grid digital elevation model (DEM, see Figure 2.4) by the Spatial Analyst Tool of ArcGIS 10.2. The DEM was created by the Center for Space and Remote Sensing Research at National Central University in Taiwan, and the dip directions of cleavage were compiled from available geological maps and other field-based investigation reports (Hu and Liu, 1987; Lee, 1977; Lin et al., 2011b; Lin, 1999; Sung, 1991; Sung et al., 2000). We use the Spatial Analyst Tool of ArcGIS to construct two grids using the inverse distance weighted (IDW) method; one grid shows the cleavage dip azimuths (Figure 2.3) while the other shows the hill slope dip azimuth (Figure 2.6). The grid of cleavage dip azimuth was constructed with 5km node interval, and the grid of hill slope dip azimuth was constructed with 80m node interval. The 5km interval for cleavage dip direction is the maximum average distance between cleavage measurement points with the same dip direction. The 80m interval for slope direction is the result of program's computation limit because the number of grids exceeds the program's memory allocation limitation when the grid interval is less than 80m. We then subtracted the grid of cleavage dip azimuth by the grid of hill slope azimuth, which yielded a preliminary θ_D. (see Figure 2.7).

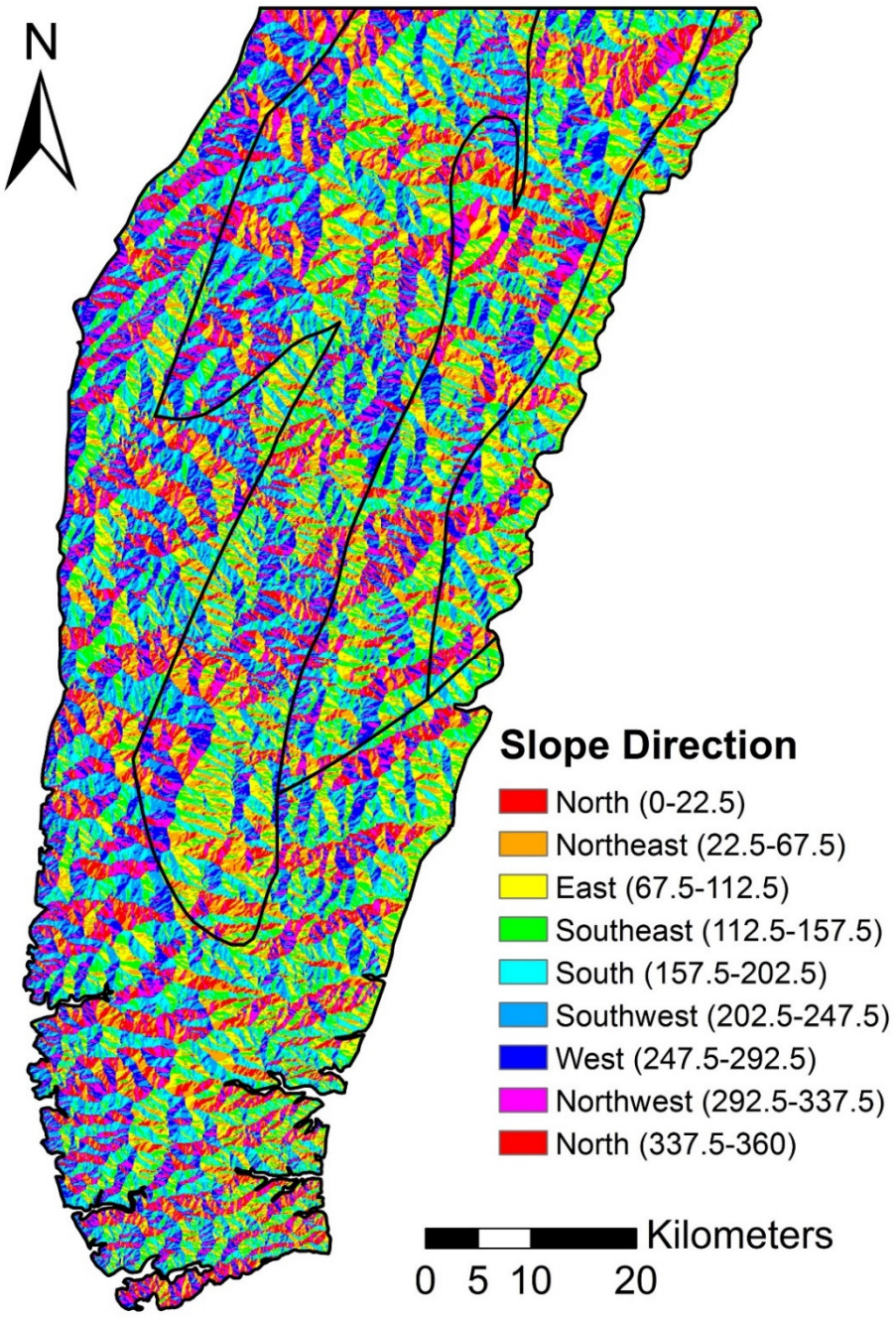

Figure 2.6. Map of slope direction.

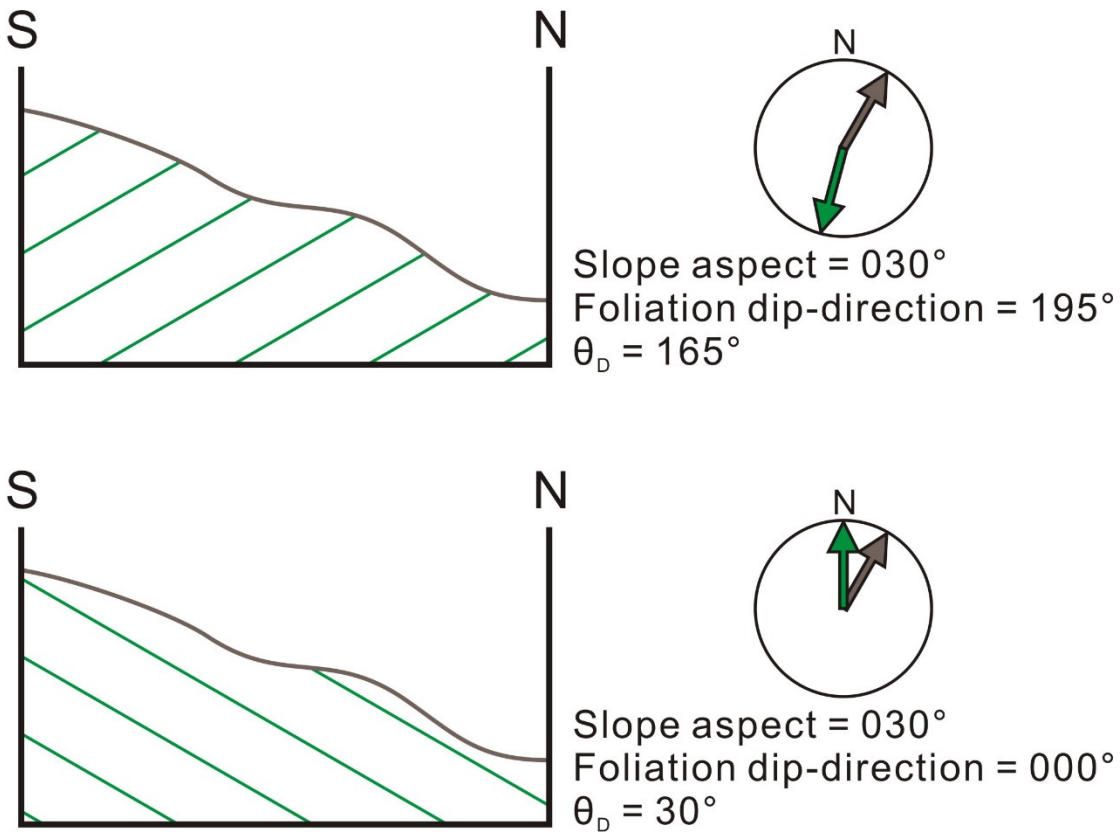

Figure 2.7. Illustration of the calculation of θ_D. The upper figure is an example of higher θ_D, and the lower figure is an example of lower θ_D.

If the absolute value of azimuth is larger than 180°, we then subtracted the angle by 180°. After calculating the θ_D value of each grid, we constructed another grid representing θ_D with a resolution of 80m. The grid represents a dip-slope structure when θ_D is 0, and the grid represents a scarp slope structure when the θ_D is 180 (Figure 2.8).

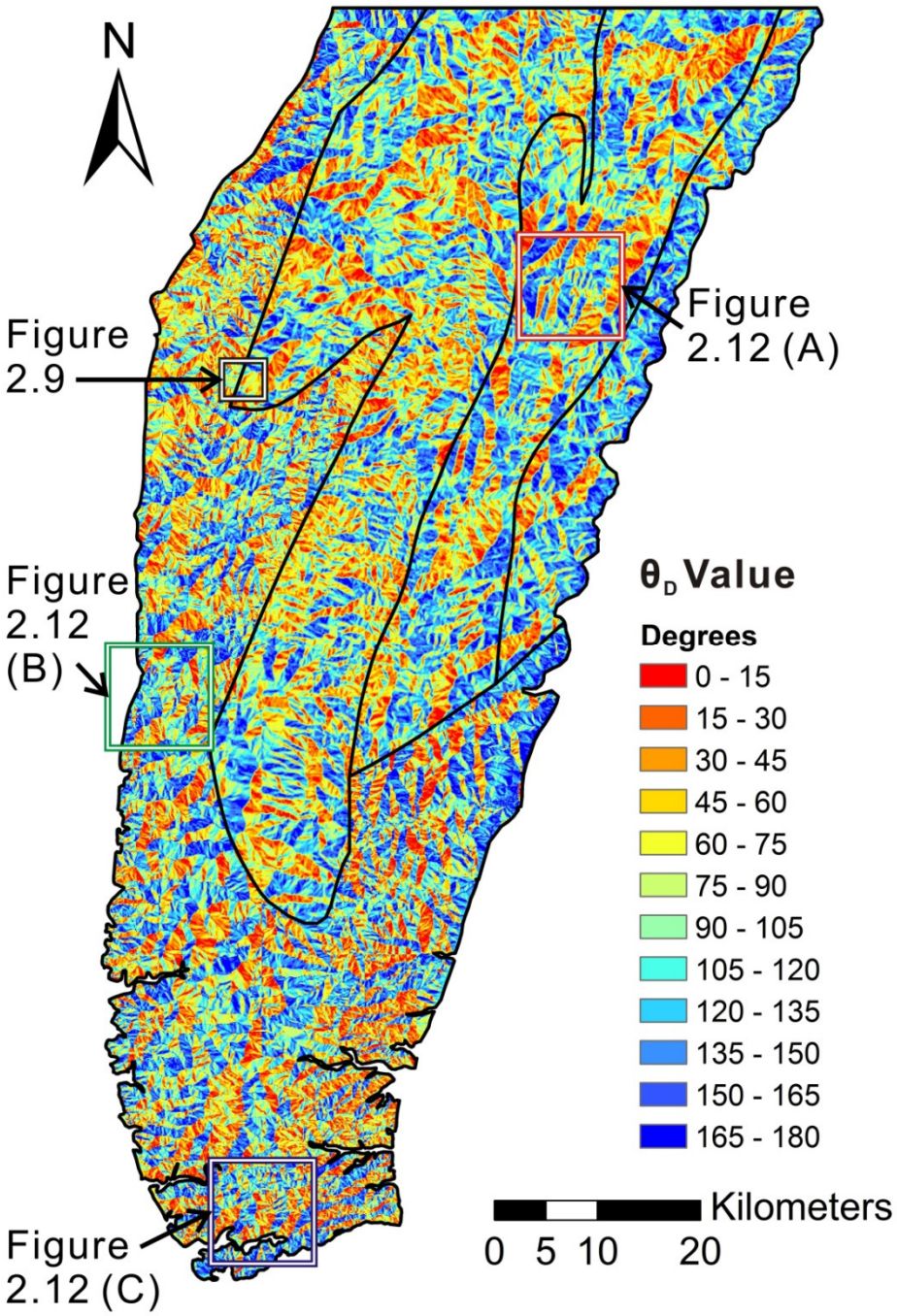

Figure 2.8. Map of θ_D value. The black rectangular is the example area of the relation of θ_D and landslides in a satellite image in Figure 2.9, the red square is the example area of schist in Figure 2.12, the green square is the example area of higher metamorphism grade slate in Figure 2.12, and the blue square is the example area of lower metamorphism grade slate in Figure 2.12.

An example of using θ_D in the slate region is shown in the Figure 2.9. The cleavage generally dips south in this area, and most of the higher θ_D value contours are distributed on the north-facing slopes, lower θ_D value contours are distributed in the south-facing slopes. The landslides are mostly distributed in the south facing slopes which is consistent with the locations of lower θ_D value contours because the cleavage generally dips southward in this area. The north facing slope in the upper right corner of the image (encompassed by the 150° contour) has no landslides on it, which shows that steep hill slopes are not necessary associated with a higher density of landslide.

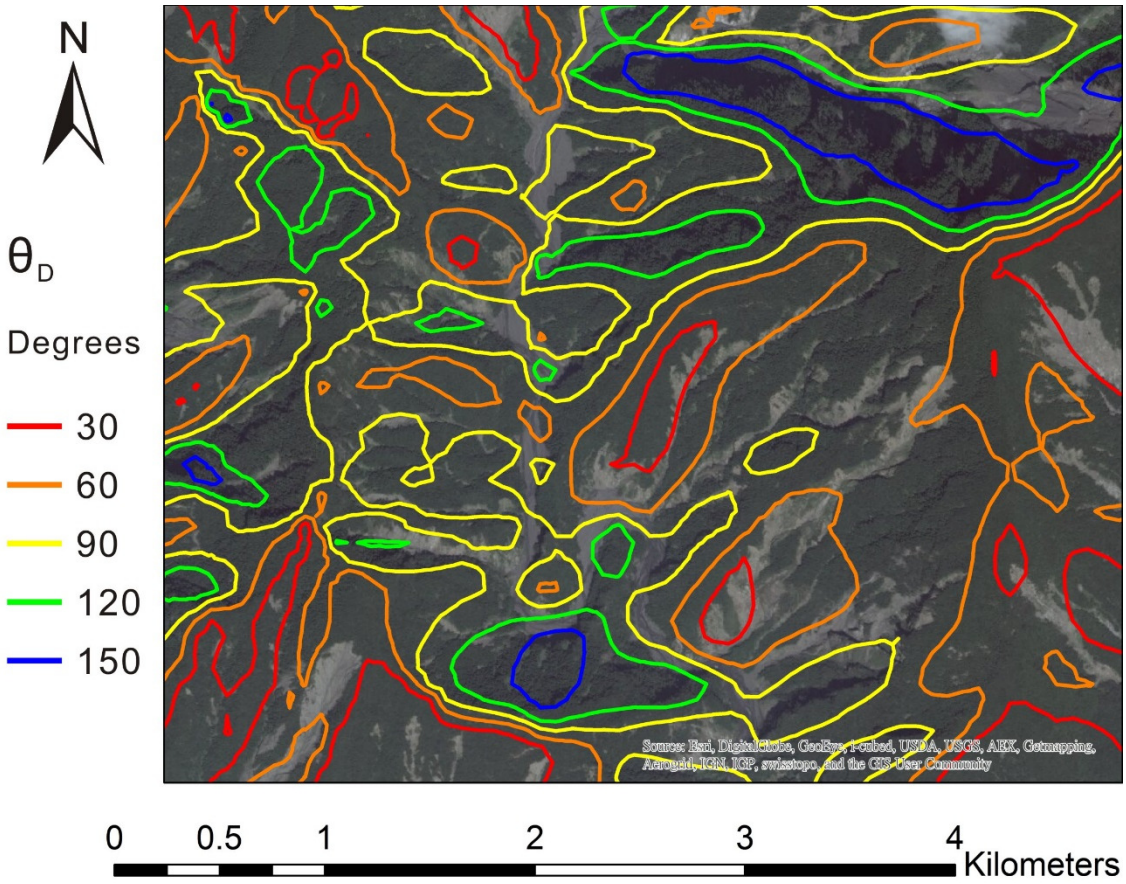

Figure 2.9. Satellite image of schist area. The dip direction of foliation in this area is generally to the south. Note the higher θ_D value are mostly located in the north facing slope and the lower θ_D value are mostly located in the south facing slope. The landslides are mostly occurred in the south facing slope, which suggests the θ_D value is a strong factor of landslide in this area.

2.4 RESULTS

The probability density histograms show the difference in θ_D values for the whole field area compare to θ_D values for areas with landslides (Figure 2.10). In areas underlain by slate, landslides are more common at low θ_D values (e.g. less than 90°) then at high values. That is, landslides appear to form preferentially in areas where the topographic slope and cleavage dip directions are sub-parallel. In contract, the schist landslide are more common in areas with high θ_D values where the slope and cleavage dip in opposite directions.

In the slate region (histogram A), the probability density percentage of landslides is about 1% higher than the percentage of whole area in the slate region when θ_D value is equal to 0° to 90°. The percentage of landslide decreases from 90° to 180°. The percentage of landslides is 0.2% higher than the percentage of the whole area in the bin of 90° to 105°, and the percentage of landslides is less than the percentage of the whole area while 105° to 180°. The difference of percentage between landslides and whole area increase from 105° to 180°, and the percentage of landslides is lowest in the bin of 165° to 180°. The θ_D value of the whole slate region distributes between 7.5 to 8.8%, and the θ_D value of landslide ranges from 6.6 to 9.8%. There is 9.8% of the landslides, which is the largest group of landslides in the slate area with the same θ_D value, occurring in the areas with θ_D value from 75° to 90°. The median of θ_D value of the whole slate area is 92.9°, and the median of θ_D value of the landslides in the slate is 80.0°. The result represents most of the

landslides in the slate occurred in the area with less than 80°, and it suggests the landslides in the slate region prefer to occur in the lower θ_D value area.

The histograms of θ_D values show different pattern in the schist region (histogram B). The percentage of whole area is higher than the percentage of landslides from 0° to 105°. The difference between landslides and whole area is 3.5% in 0° and 0.6% in 105°. The percentage of landslide become larger than the whole area between 105° to 180°, which ranges from 2.4 to 4.1%. The median of θ_D value of schist region is 97.2°, and the median of θ_D value of landslide is 116.2°. The θ_D value of the schist region ranges between 7.7 to 9.3%, and the θ_D value of landslides ranges from 4.2 to 13.0%. There is 13.0% of the landslides occurring in the areas with θ_D value between 135° to 150°, and it represents the largest group of landslides in the slate area with the same θ_D value. The median of landslides in schist region is 116.2°, higher than the regional θ_D value, and thus it indicates the landslides in the schist region tend to occur in the higher θ_D value area.

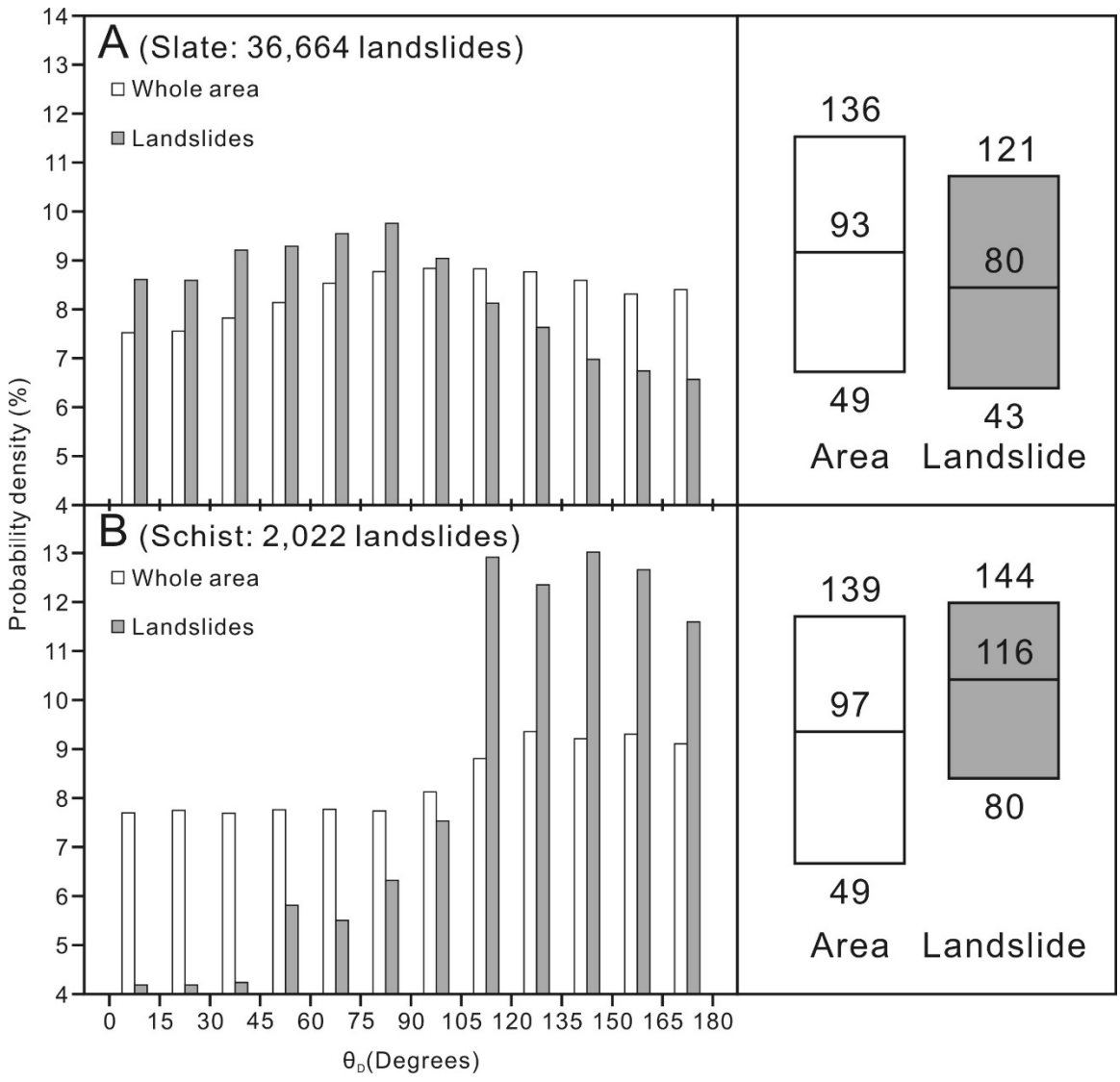

Figure 2.10. Probability density histograms and box plot of θ_D value in slate and schist area.

The histogram of landslide probability and slope have different pattern from the histogram of landslide probability and θ_D. The slope distribution histogram between landslides and whole area of the slate and schist shows similar pattern. Most of the landslides in the slate are occurred in the bins between 20° and 30°, and most of the landslides in the schist occurred in the bins between 30° and 40° (Figure 2.11), and suggests the landslide occurs in the areas with ~30° slope despite different lithological units. The result suggest the slope in both of slate and schist plays same role in the landslide probability.

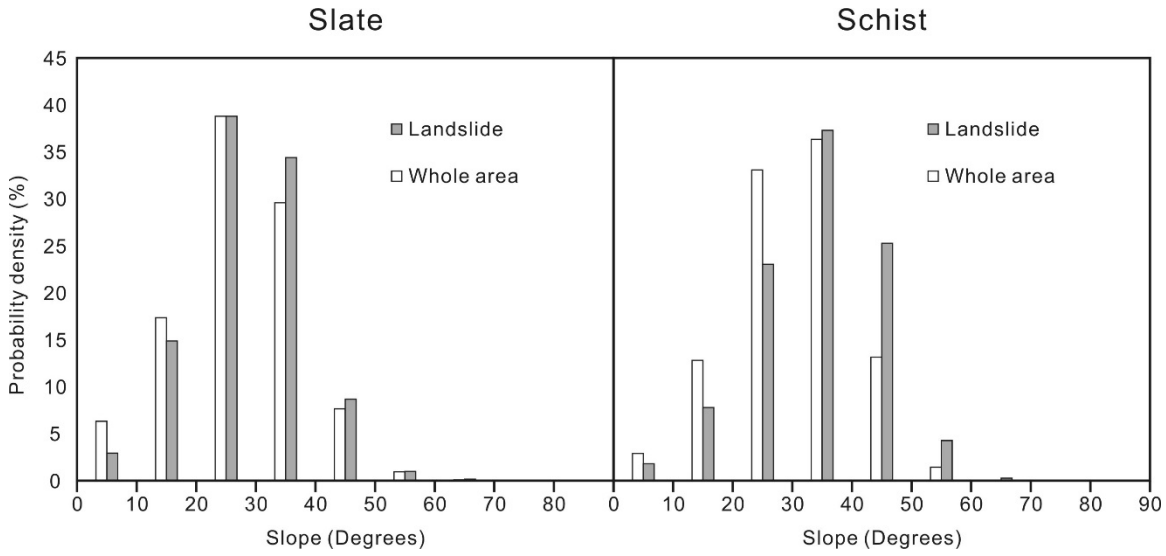

Figure 2.11. Probability density histograms of hill slope in slate and schist area.

2.5 DISCUSSION AND CONCLUSION

The result presented above suggest that the landslides in the slate tend to occur in the areas with lower θ_D whereas landslides in the areas underlain by schist tend to occur where θ_D is higher, and thus we propose this is a significant result of understanding the role of tectonic cleavage in the distribution of landslides.

To understand how the anisotropy influences the landslide patterns in more detail, we selected three smaller areas to make probability density histograms (areas locations are marked in Figure 2.8, histograms in Figure 2.12). Histogram A is from the schist region where the cleavage generally dips northwest, and histogram is similar pattern to the histogram in Figure 2.10. The probability density percentage of whole area is about 5% to 10% higher than the percentage of landslide when the θ_D value is lower than 45°, and the difference of percentage between landslides and whole area decreases when the θ_D value is larger than 45°. The percentage of the landslide increases and become larger than the whole area when the θ_D value is greater than 105°. The percentage of landslide area is 24.4% when the θ_D value between 165° and 180°, while the whole area is 12.7% in the same range of θ_D value. The median of the θ_D value in this area is 100°, and the median of the θ_D value of the landslides is 138°. There is 24.4% of the landslides occurring in the areas with θ_D value between 165° and 180°, and it represents the largest group of landslides in the slate area with the same θ_D value. We suggest this area is the end member of landslides in the high θ_D value. This

result indicates the landslides tend to occur in the place where cleavage dips opposite to the direction of slope.

Histogram B is from higher metamorphism grade slate, which displays a well-developed slaty cleavage and the histogram is similar to the histogram in Figure 2.10. The probability density percentage of landslides is about 1% to 5% higher than the percentage of whole area when the θ_D value is lower than 105°. The percentage of the landslide decreases and become less than the percentage of whole area when the θ_D value is greater than 105°. The differences of percentage between landslide and whole area increase along with the θ_D value between 105°and 150°. The percentage of landslide area is 1.8% when the θ_D value between 165° and 180°, while the percentage of the whole area is 7.4% in the same range of θ_D value. The median of the θ_D value in this area is 97°, and the median of the θ_D value of the landslides is 80°. There is 14.6% of the landslides occurring in the areas with θ_D value between 90° and 105°, and it represents the largest group of landslides in the slate area with the same θ_D value. The histogram shows the landslides in this area tend to occur in the lower θ_D value area, and the percentage of landslide decreases when the cleavage dip direction is against the slope direction, which is opposite to the landslide pattern in the schist.

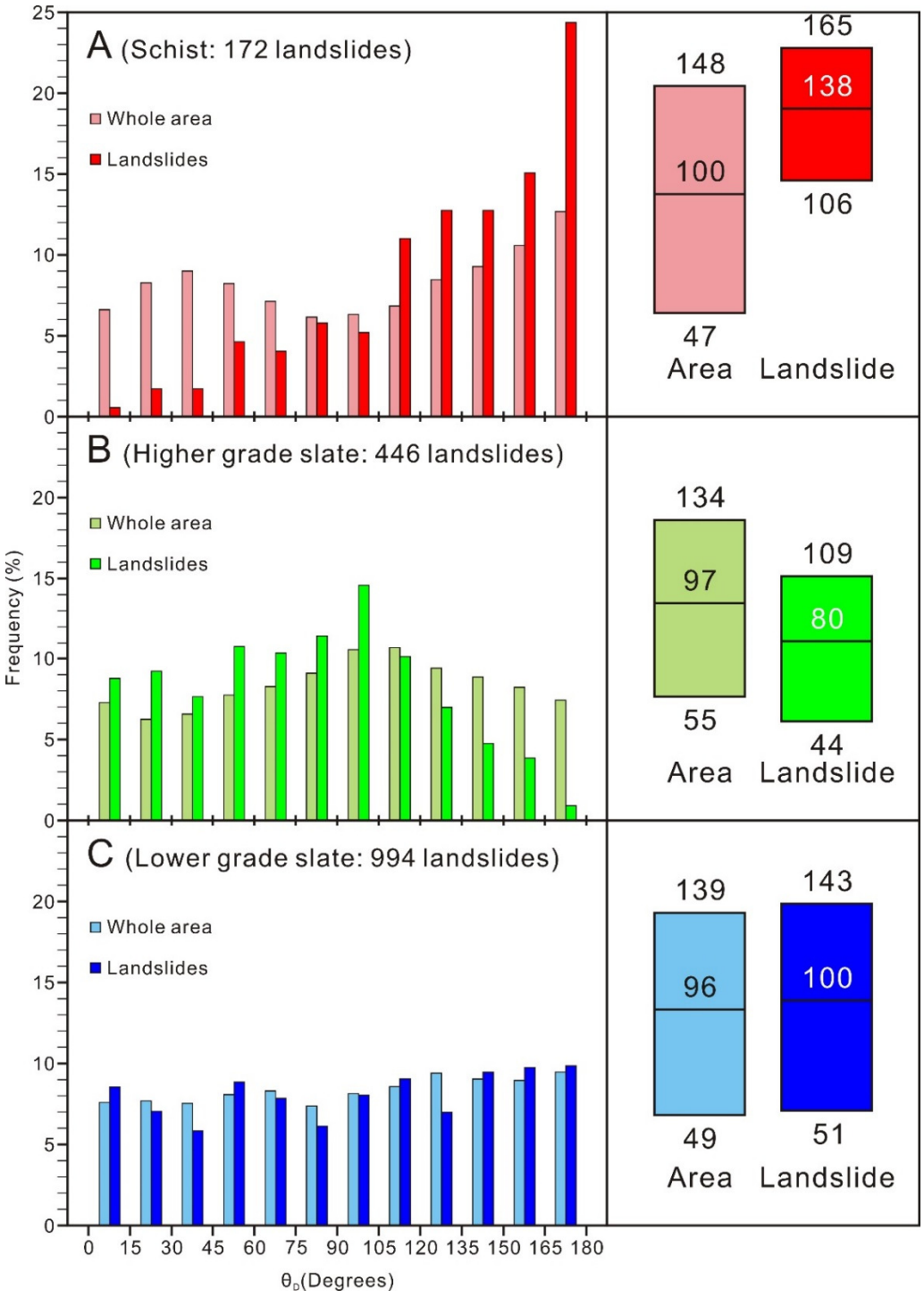

Figure 2.12. Probability density histograms and box plot of θ_D value in schist (A), higher metamorphism grade slate (B), and lower metamorphism slate (C). Data location map see Figure 2.8.

Finally, histogram C is from lower metamorphism slate and the tectonic fabric is less well developed and a pencil cleavage is more common rather than a well-developed slaty cleavage. The histogram shows no significant differences between whole area and landslides, in other words, the deference of probability density percentage between whole area and landslide landslides ranges only from 0.3 to 1.7%. The result suggests that the landslides have no preference of θ_D value, which is different from the slate with well-developed cleavage and schist.

These three histograms show two end members: in areas underlain by schist, landslides occur at high θ_D values whereas in areas underlain by well-developed slate, landslides occur at low θ_D values. Although there are multiple ways of interpreting these results, one possibility is that the results reflect the shear strength of the dominant fabric anisotropy. For example, the cleavage in slate belt appears to be relatively weak due to the lack of cohesion between the cleavages whereas the cleavage in the schist appears to be relatively strong. These interpretations are consistent with field and thin-section observations that show the cleavage in the slate belt to be penetrative and homogeneous at a regional scale. Interestingly, the rocks in the slate belt appear to be relatively strong as they support essentially all of the high peaks in the Central Range. In contrast, the fabric in the schist is a crenulation cleavage and rarely forms a planar, penetrative fabric, consistent with the low θ_D values in areas with few landslides. The dominance of landslides at high θ_D values in the schist may reflect the generally steeper east dipping slopes along the east flank of the range.

Finally, areas underlain pencil cleavage, which represents a poorly developed fabric with a weak anisotropy and shows no correlation with the distribution of landslides. We suggest, therefore, slope failure in the schist might be dominated by the hill slopes gradient, so it has less relation to the weak bedding or cleavage surface. The landslides in the slate with pencil cleavage have different pattern because the rock is relative homogeneous and the cleavage is not continuous enough to be a weak sliding plane. In other words, the landslides don't have to be the dip-slope failure and could be any kind of rock fall.

To sum up, landslides underlain by slate, with a well-developed cleavage, tend to occur in the areas with small θ_D values, whereas landslides in underlain by schist where multiple cleavages are present tend to occur in the areas with large θ_D value, and, finally, in areas with a poor-developed cleavage, landslide distributions have no prefer θ_D value. In conclusion, the θ_D value can be a useful tool to determine the probability of landslide occurrence in a metamorphic terrain and could help the estimate the volume of erodible material in a mountain range.

2.6 REFERENCE

Central Geological Survey (Taiwan), 2013. Geological Investigation and Database Construction for Upstream of Flood-Prone Area. 192 pp. (in Chinese).

Chang, K.-J., Taboada, A., Chan, Y.-C., 2005. Geological and morphological study of the Jiufengershan landslide triggered by the Chi-Chi Taiwan earthquake. Geomorphology 71, 293-309.

Chen, C.-H., 2000. Geologic Map of Taiwan. Central Geological Survey, Ministry of Economic Affairs.

Chen, C.-H., Ke, C.-C., Wang, C.-L., 2009. A back-propagation network for the assessment of susceptibility to rock slope failure in the eastern portion of the Southern Cross-Island Highway in Taiwan. Environmental geology 57, 723-733.

Chen, R.-F., Chan, Y.-C., Angelier, J., Hu, J.-C., Huang, C., Chang, K.-J., Shih, T.-Y., 2005a. Large earthquake-triggered landslides and mountain belt erosion: the Tsaoling case, Taiwan. Comptes Rendus Geoscience 337, 1164-1172.

Chen, W.-S., Chen, Y.-C., Yu, N.-t., Yen, I.-C., Yang, B.C.-C., Shih, T.-S., 2005b. Stratigraphic And Tectonic Geomorphic Studies Along The Chao Chou Fault, Southern Taiwan-Reevaluating Fault Characteristics And Location. Special Publication of the Central Geological Survey 16, 75-90.

Chigira, M., 1992. Long-term gravitational deformation of rocks by mass rock creep. Engineering Geology 32, 157-184.

Crespi, J., Chan, Y.-C., Swaim, M., 1996. Synorogenic extension and exhumation of the Taiwan hinterland. Geology 24, 247-250.

Fisher, D.M., Willett, S., Yeh, E.-C., Clark, M.B., 2007. Cleavage fronts and fans as reflections of orogen stress and kinematics in Taiwan. Geology 35, 65-68.

Guzzetti, F., Peruccacci, S., Rossi, M., Stark, C.P., 2008. The rainfall intensity–duration control of shallow landslides and debris flows: an update. Landslides 5, 3-17.

Ho, C.S., 1986. A synthesis of the geologic evolution of Taiwan. Tectonophysics 125, 1-16.

Hu, H.N., Liu, H.D., 1987. Geologic Road Map from Meishan to Yakou along the Southern Cross-Island Highway. Central Geological Survey, Taipei, Taiwan, R.O.C.

Hung, J.-J., 2000. Chi-Chi earthquake induced landslides in Taiwan. Earthquake Engineering and Engineering Seismology 2, 25-33.

Lee, C.T., 1977. Structural geology of Likuan region, South Cross Island Highway (In Chinese). National Taiwan University, Taipei, Taiwan, R.O.C.

Lee, J.-C., Chu, H.-T., Angelier, J., Chan, Y.-C., Hu, J.-C., Lu, C.-Y., Rau, R.-J., 2002. Geometry and structure of northern surface ruptures of the 1999 Mw=7.6 Chi-Chi Taiwan earthquake: influence from inherited fold belt structures. Journal of Structural Geology, 173-192.

Lin, C.-W., Chang, W.-S., Liu, S.-H., Tsai, T.-T., Lee, S.-P., Tsang, Y.-C., Shieh, C.-L., Tseng, C.-M., 2011a. Landslides triggered by the 7 August 2009 Typhoon Morakot in southern Taiwan. Engineering Geology 123, 3-12.

Lin, C.-W., Lin, W.-H., Kao, M.-C., 2011b. Chaozhou, Explanatory text of the geologic map of Taiwan. Central Geological Survey, Chungho.

Lin, W.-H., 1999. On The Laonunghsi Fault - A Boundary Fault Between The Paleogene And The Neogene Strata, Southern Taiwan. Bulletin of the Central Geological Survey 12, 1-24.

Malamud, B.D., Turcotte, D.L., Guzzetti, F., Reichenbach, P., 2004. Landslides, earthquakes, and erosion. Earth and Planetary Science Letters 229, 45-59.

Sung, Q., 1991. Geological Map and the explanatory text for the Hengchun peninsula, south Taiwan, on scale 1: 50000. Central Geological Survey, MOEA, Taiwan.

Sung, Q., Lin, C.-W., Lin, W.-H., Lin, W.-C., 2000. Chiahsien, Explanatory text of the geologic map of Taiwan. Central Geological Survey, Chungho.

Tang, C.-L., Hu, J.-C., Lin, M.-L., Angelier, J., Lu, C.-Y., Chan, Y.-C., Chu, H.-T., 2009. The Tsaoling landslide triggered by the Chi-Chi earthquake, Taiwan: insights from a discrete element simulation. Engineering Geology 106, 1-19.

Teng, L.S., 1990. Geotectonic evolution of late Cenozoic arc-continent collision in Taiwan. Tectonophysics 183, 57-76.

Wieczorek, G.F., 1996. Landslide triggering mechanisms. AK Turner and RL Schuster, op. cit, 76-90.

Yu, S.-B., Cheng, H.-Y., Kuo, L.-C., 1997. Velocity field of GPS stations in the Taiwan area. Tectonophysics 274, 41-59.

CHAPTER 3

Geomorphic indices and differential uplift patterns in the southern Central Range

3.1 INTRODUCTION

Taiwan is an active orogen resulting from the oblique convergence between the Philippine Sea Plate and the Chinese Continental Margin (Yu et al., 1997). High rates of convergence result in high uplift rates, ranging from a few mm/yr to up to 20 mm/yr based on a recent geodetic survey (Ching et al., 2011). Geodetic benchmarks, however, can be only deployed on the major highways because the rough topography makes the survey and maintenance of benchmarks difficult. Due to the uneven distribution of benchmarks, the surface displacement data is limited to two mountain-crossing highways and the eastern and western edges of the mountain. As a result, the deformation pattern and uplift history in the center of the southern Central Range is not clear.

In order to understand the deformation pattern of the southern Central Range, we use the geomorphic indices to describe the differential uplift patterns of the active orogeny. The geomorphic indices can reflect the surface deformation, which can help reconstruct the deformation pattern in the areas without geodetic measurements. The following two geomorphic indices are used in the study, river steepness index (k_{sn}) and basin asymmetry factor (AF). We first use the two indices to describe the overall surface deformation pattern of the southern Central Range, then we focus on the geomorphic indices in the area of the recently recognized Laonung antiform (see Chapter 1).

3.2 GEOLOGICAL AND GEOMORPHOLOGICAL SETTING

There are six tectonostratigraphic units in Taiwan, and four of them form the orogen. From west to east, they are Western Foothills, Hsuehshan Range slate belt, Central Range slate belt, and Tananao Metamorphic Complex (Ho, 1986, see Figure 3.1 and 3.2). The Western Foothills is an unmetamorphosed fold-and-thrust belt, and it is composed of detrital sedimentary rock age from Oligocene to Pleistocene. The Hsuehshan Range slate belt is composed of Eocene and Oligocene low grade metamorphic rock. The Central Range slate belt can be divided into two sections, one is Miocene slate and another is Eocene slate. Both of the sections are low grade metamorphic rock (prehnite-pumpellyite facies), but the Eocene slate records slightly higher peak metamorphic temperature than the Miocene slate according to the thermochronology data. The Tananao Metamorphic Complex is composed of pre-Tertiary schist and marble, and different sets of crenulation cleavages found in the schist indicates multiple stages of deformation (Chen and Wang, 1995; Fisher et al., 2007; Ho, 1986).

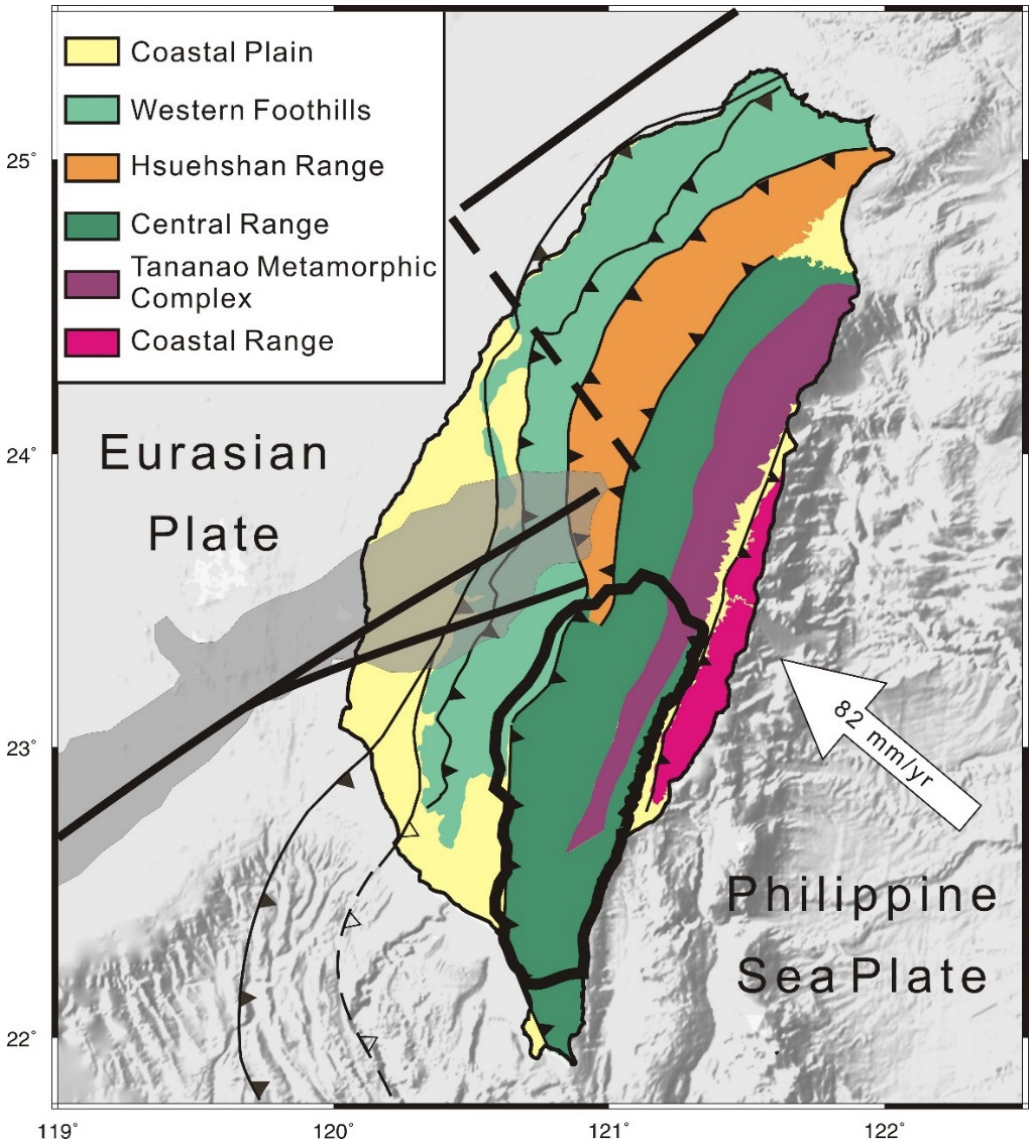

Figure 3.1. Tectonostratigraphic and GPS velocity map of Taiwan modified from Lee et al. (2002) and Yu et al. (1997). The study area is outlined by black line. Black solid lines in the western Taiwan are the interpreted boundary of continental crust based on magnetic anomaly and Mesozoic basement morphology, and the black dashed line is interpreted continental edge fracture zone (Byrne et al., 2011). The shaded area represents the continental margin magnetic anomaly (Cheng, 2004; Hsu et al., 1998). White arrow represents the convergent direction and rate between Philippine Sea Plate and Eurasian Plate (Yu et al., 1997). The velocity is related to the Paisha station, S01R, located in the Chinese continental margin.

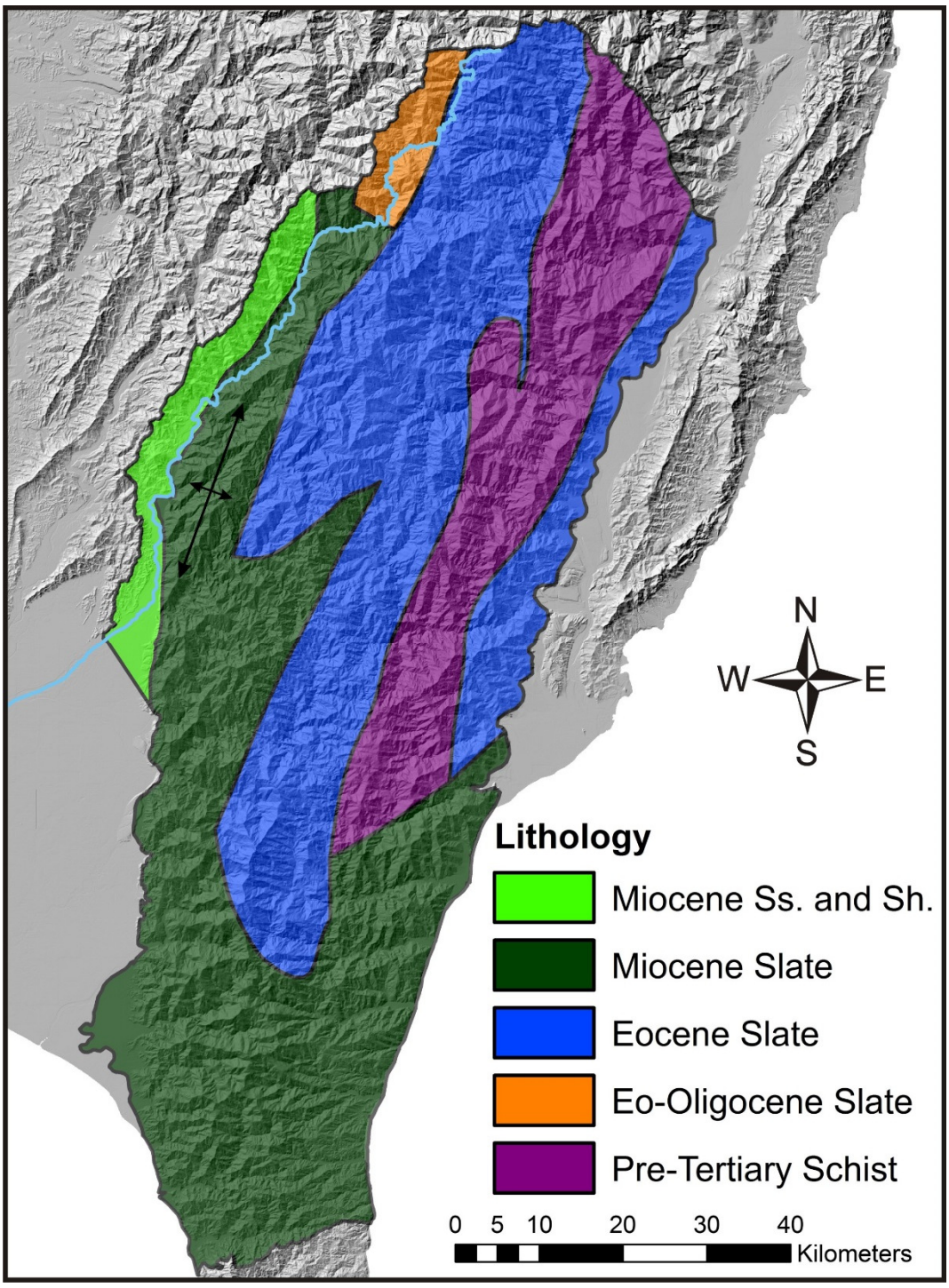

Figure 3.2. Geological map of study area modified from Chen, (2000). The Laonung antiform is in the northwest corner of the Miocene slate.

A recently discovered active antiform is located in the northwest corner of the study area (Huang and Byrne, 2014), which is named the Laonung antiform in this study. The Laonung antiform is composed of Miocene slate, verges to the west and is considered to have formed in brittle environment based on detailed structural studies (see Chapter 1). GPS and stress inversion data show northwest shortening, and geodetic data along the Laonung River, which crosses the antiform at an oblique angle (Ching et al., 2011) show an uplift rate of up to 12 mm/yr (Ching et al., 2011). River incision rates based on dated terraces as old as 2000 years along the Laonung River indicate slightly higher rates of 20 mm/yr (Chapter 1).

East-west topographic profiles show that the slope in eastern Taiwan is steeper than in western Taiwan and the distance from ridge crust to western flank of the orogen is longer than the distance to the eastern flank of the orogen (Suppe, 1981; Willett et al., 2001). Thus, the orogenic belt displays a regional-scale asymmetry in cross section; however, this asymmetrical pattern is less developed in the southern Central Range, which may reflect the relatively younger age of the orogen in this area.

In this study, we focus on the geomorphology of southern Central Range because the orogenic belt forms a single mountain range that is actively emerging above sea level. The central and northern parts of the orogen contain two ranges, the Hsuehshan and Central Ranges; however, how the two mountain belts influence each other during deformation is still not clear. Mt. Yu (the highest peak in Taiwan, 3,952 m) marks the northern edge of the study area whereas the southern edge of the study area is the boundary between metamorphosed Miocene slate and unmetamorphosed sedimentary rock exposed in the Hengchun

Peninsula. The major drainage system in the west flank of the study area is the Laonung River, while the major drainage in the east flank of the study area is the Peinan River. Previous studies of the geomorphology of this region of Taiwan suggest a regional pattern of southward tilting at least along the east side of the southern Central Range (Ramsey et al., 2007). For example, drainage basins on the eastern flank of the range are asymmetric with areas of northern banks larger than the areas of the southern banks. The western flank of the range shows a more complex pattern of basin geometries (Liao, 2003). Based on a combined analysis of basin spacing, basin elongation ratios, basin asymmetries, stream profiles, mountain front sinuosity, hypsometry, and height to width ratio of drainage basin, the northern part of the range appears to be more active than the southern part of the range (Wiltschko et al., 2010).

In addition to these general watershed patterns, Ouimet et al. (2012) have recognized several surfaces of low relief that straddle the ridge crest of the range. Although the origin of the surfaces is still unknown, Ouimet et al. (2013) have proposed that the surfaces represent the remains of an older topographic pattern that has not yet eroded.

3.3 METHOD

Two geomorphic parameters, river steepness index (k_{sn}) and drainage basin asymmetry (AF), are used to evaluate differential uplift in the southern Central Range. k_{sn} values generally relate to uplift rate and

rock erodibility, with higher k_{sn} values reflecting stronger rocks or higher uplift rates. Drainage basin asymmetry records tilting of a drainage basin or bedrock anisotropy within a basin.

3.3.1 River steepness index (k_{sn})

In an active uplift mountain, the profile of river channel can be controlled by the rock uplift rate *U* and erodibility *K*. In a steady state river channel, the uplift rate (*dz*/*dt*) is equal to the difference in the rock uplift erosion rate, *E*, so the relation can be written as:

$$\frac{dz}{dt} = U - E = 0 \tag{1}$$

and erosion rate can be described as the function:

$$E = KA^m S^n \tag{2}$$

where *A* is upstream drainage area, *S* is channel gradient, *K* is erodibility, and *m* and *n* are empirical constants whose ratio (*m*/*n*) is typically ~0.5 (Kirby and Whipple, 2012).

Combining Equation (1) and (2), the channel gradient *S* can be defined as:

$$0 = U - KA^m S^n \tag{3}$$

$$S = \left(\frac{U}{K}\right)^{\frac{1}{n}} A^{\frac{-m}{n}} \tag{4}$$

$$S = k_s A^{-\theta}, \text{ where } k_s = \left(\frac{U}{K}\right)^{\frac{1}{n}}, \text{ and } \theta = \frac{m}{n} \tag{5}$$

where k_s is channel steepness and θ is the concavity index (Wobus et al., 2006). The parameter θ is typically between 0.4 and 0.6 (Kirby and Whipple, 2012) and considered to be independent of the rate of rock uplift (Whipple and Tucker, 1999). River profiles form a straight line when the $\theta = 0$, concave when $\theta > 0$, and convex when $\theta < 0$. Equation (5) describes the slope of a single river channel, however, previous studies have shown that the value of θ varies across different drainage basins. In order to compare the channel steepness in different drainage basins, steepness indices should be normalized using a reference concavity, which is normally calculated from concavities of rivers in the same region:

$$S = k_{sn} A^{-\theta_{ref}} \tag{6}$$

where k_{sn} is the normalized steepness index (normalized to the catchment size) and θ_{ref} is the reference concavity. The river gradient in the upstream is larger than the downstream, and the contributing drainage area in the upstream is smaller than the downstream in a steady state river. In other words, k_{sn} in a steady state river with a given fixed θ_{ref} should have the same value in every segment of the river because the k_{sn} is the ratio of S and A:

$$\frac{S}{A} = k_{sn} \tag{7}$$

The parameter k_{sn} can therefore be used as an indicator of anomalous river segments with either high or low gradients. For example, area of a drainage basin in the downstream segment is larger than upstream, if the river gradient of river in downstream segment is larger than the upstream, then the k_{sn} of that segment will

be higher than the k_{sn} in same location of a steady state river. If the k_{sn} in the upstream is significantly lower than the k_{sn} in the same segment of a steady state river, the topography there could be gentler than the topography of upstream of a steady state river.

The k_{sn} value of the study area was mapped using a MATLAB script written by Whipple et al. (2007) and the topographic data is obtained from the 40 m digital elevation model (DEM) derived from aerial photo pairs and is created by the Center for Space and Remote Sensing Research at National Central University in Taiwan. The k_{sn} value was calculated by the batch profiler script that uses 1 km stream segments on all streams with upstream drainage areas $\geqq 1$ km^2. The raw river profiles calculated from the 40 m DEM were also smoothed using a 250 m moving window, and the channel gradients are calculated at 5 m intervals. The reference concavity θ_{ref} is 0.58 based on the average of θ values in 6 rivers on the west flank of the southern Central Range, where the θ value is extracted from log-transformed slope-area regression profile data. In this study, a grid of k_{sn} with 250 m interval is generated from a scattered point set which were converted from all the river segments in the study area. The grid k_{sn} map was made by the inverse distance weighted (IDW) method using the Spatial Analyst Tool of ArcGIS. The k_{sn} grid provides values in areas without river profile and also helped visualize k_{sn} patterns in the whole study area (Karlstrom et al., 2012; Rosenberg et al., 2014).

3.3.2 Basin asymmetry factor (AF)

Basin asymmetry factors (AF) can indicate the tilting direction of a drainage basin, and can be an indicator to estimate the differential uplift patterns in an active orogen. The basin asymmetry factor, AF, is defined by Hare and Gardner (1985) as:

$$AF = 100\left(\frac{A_r}{A_t}\right) \tag{8}$$

where A_t is the drainage area of the whole drainage basin and A_r is the drainage area to the right bank of the main trunk stream when looking downstream. If AF < 50 then the drainage basin is inferred to have tilted to the right, again looking downstream, similarly, if AF > 50 then basin is inferred to have been tilted to the left. AF ~ 50 indicates a basin symmetrical basin.

3.4 RESULTS AND DISCUSSION

3.4.1 Geomorphic indices in the study area: River steepness index (k_{sn})

Indices of river steepness (k_{sn}) are generally considered to be controlled by rock erodibility and uplift rate (see Equation 5 and 6). In the southern Central Range, k_{sn} values range from low in the southern part of the range to high in the northern part of the range and generally correlate with rock type. For example, high values occur in rivers draining the Eocene and pre-Tertiary metamorphic rocks whereas lower values occur in river reaches draining the lower grade Miocene slate (Figure 3.3 and 3.4). However, an important exception to this general pattern occurs in the northwest corner of the field area in the area of the Laonung River. In this area, low-grade Miocene slate crops out and associated rivers have relatively high k_{sn} values (Figure 3.4). Leveling data along the river also show relatively high rates of uplift (up 12 mm/yr), suggesting that the high rates of uplift are more likely to be the major factor of high k_{sn} value than rock erodibility in this area.

The low relief surfaces that straddle the ridge crest in the Eocene slate correlate with low k_{sn} value consistent with the low erosion rate (0.1 - 0.3 mm/yr) from detrital cosmogenic nuclide analyses cosmogenic analysis and exposure ages on bedrock outcrops (both ^{10}Be, Ouimet et al., 2013). The low relief surfaces sit isolated from landslide-dominated watersheds with high rates of erosion (3 - 5 mm/yr) in

directly adjacent areas (Ouimet et al., 2013). The differential erosion rates and the presence of low relief topography suggest the surface uplift rate is higher than the headwater erosion rate, so the low relief surfaces may be preserved areas of older topography in the southern Central Range of Taiwan.

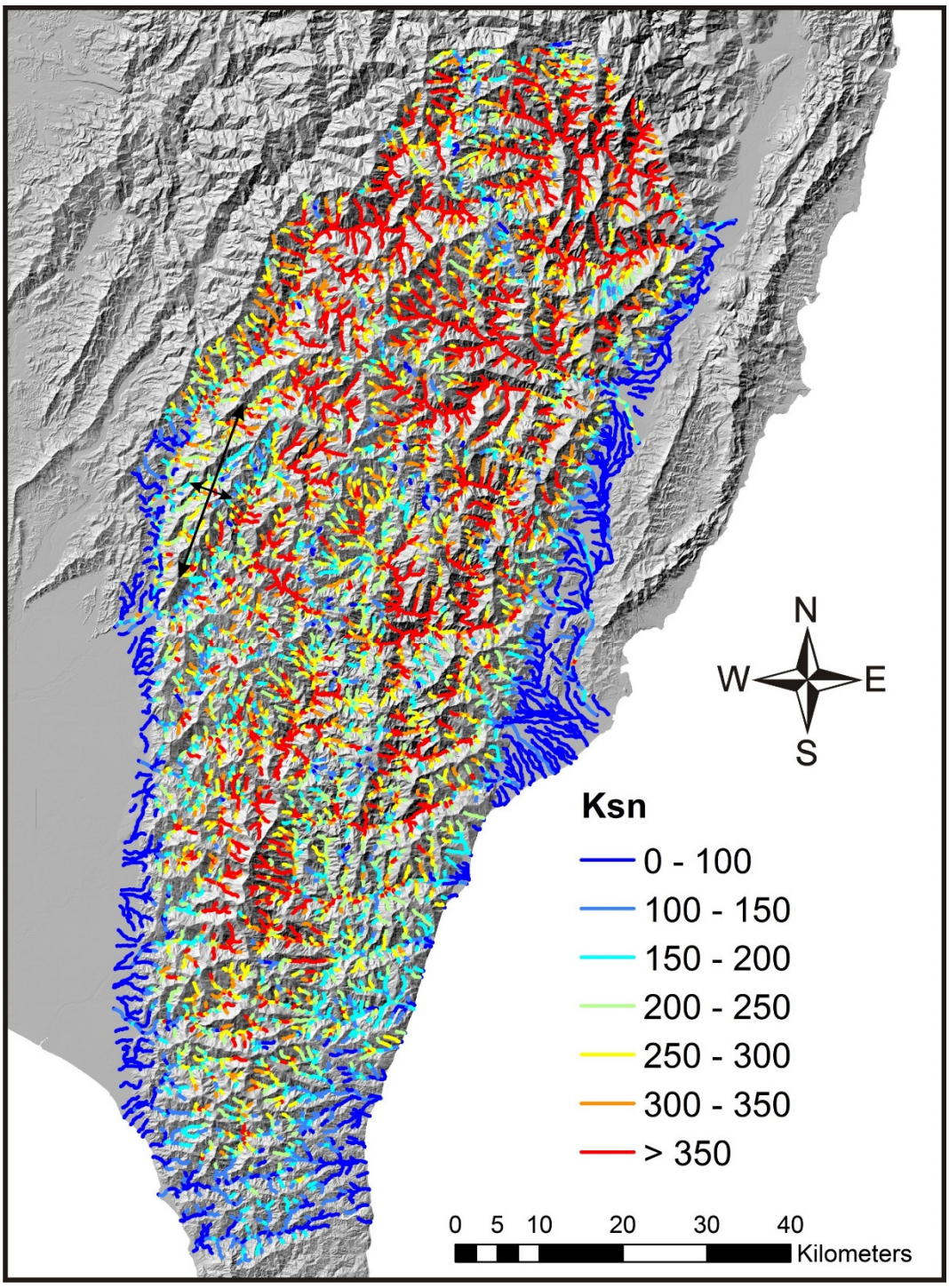

Figure 3.3. k_{sn} segments map of study area

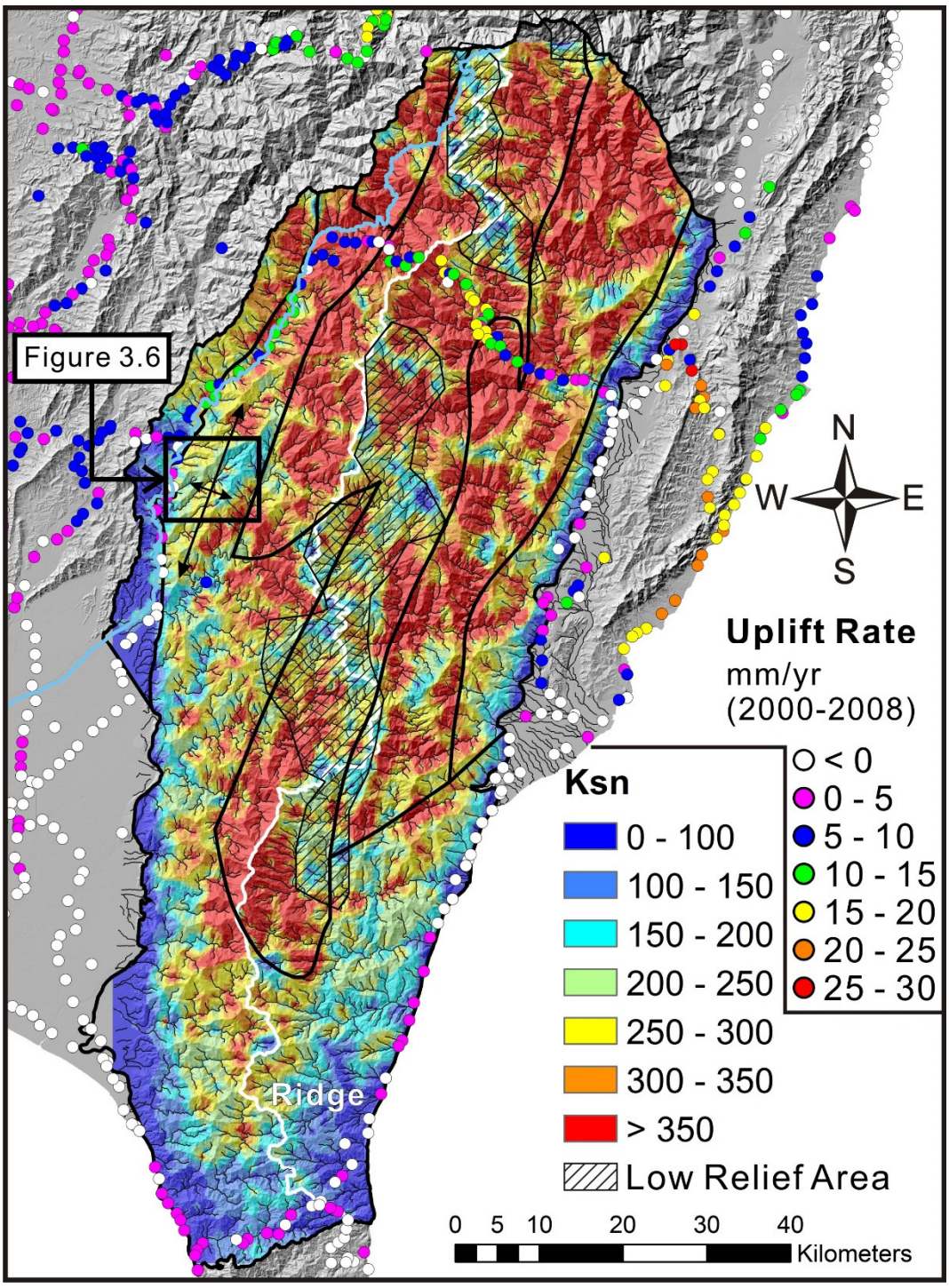

Figure 3.4. Gridded k_{sn} map and recent uplift rate of study area. The uplift data is from Ching et al. (2011). The box shows the location of Figure 3.6.

3.4.2 Geomorphic indices in the study area: Basin asymmetry factor (AF)

The asymmetry factor, AF, map shown in Figure 3.5 is compiled from two studies: Ramsey et al. (2007) who studied the east flank of the range and Liao (2003) who studied the west flank of the range. The two studies also used different basin sizes to calculate the AF values, which makes it difficult to directly compare the results of the two studies. We therefore discuss the AF values on the east and west flanks separately.

Along the eastern flank the basins progressively increase in size from south to north as AF values progressively decrease, indicating more asymmetric basins in the north. Ramsey et al., (2007) studied the asymmetry in some detail and proposed that it reflected significantly higher uplift rates in the north than could be accommodated by regional tilting alone. This conclusion was based on observations from the watersheds, showing constant hill slopes within basins but progressive higher mean slopes between basins from south to north and a uniform incision depth from south to north. Significantly higher rates of uplift in the north are consistent with leveling data along the two highways that cross the range in the north and south (Figure 3.4) and with rates of denudation in the two northern basins. For example, Derrieux et al. (2014) calculated denudation rates for the northernmost basin in Figure 3.5 (equivalent to basin #8 of Ramsey et al. and basin #9 of Derrieux et al., 2014) of about 2.5 mm/yr. The basin to the north of this basin

(not shown in Figure 3.5 but equivalent to basin #9 in Ramsey et al. and basin 8 in Derrieux et al., 2014) has a substantially higher denudation rate of about 5 mm/yr.

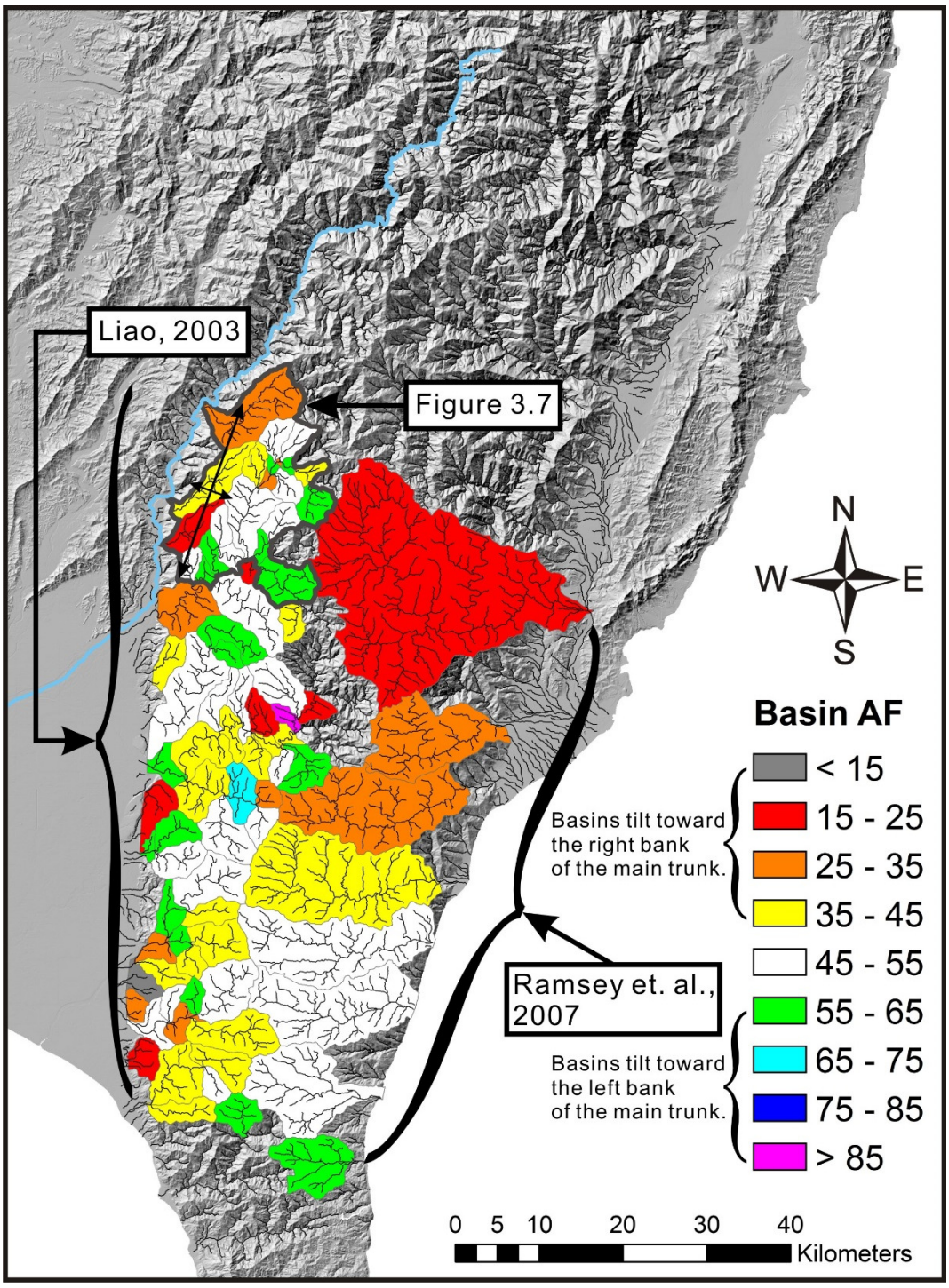

Figure 3.5. The basin asymmetry factor (AF) map of study area. The basin data from the eastern study area is modified from Ramsey et al. (2007), and the basin data from the western study area is modified from Liao (2003). The location of Figure 3.7 is shown in the northern end of the basins.

3.4.3 Geomorphic indices in area of the Laonung antiform: River steepness index (k_{sn})

In order to better understand the relation between uplift rate and k_{sn}, we use the Bangfu River watershed which crosses the Laonung antiform as an example. The entire Bangfu River catchment is in the same lithological unit (Miocene slate) so the erodibility within the river can be considered as a constant. To complete the analysis, we first extracted the k_{sn} segments of the Bangfu River catchment from the batch profiler script, and then plotted the centroid of each river segments on a 110° direction profile which is perpendicular to the axis of the antiform (Figure 3.4). The result shows k_{sn} values around 200 at the river mouth, and slightly higher values near the antiform axis. k_{sn} values then dropping to 150-200 in the upstream part of the catchment. Overall, the k_{sn} data suggest that the river reaches in the central part of the Bangfu River catchment are steeper (i.e. have higher k_{sn} values) than upstream or downstream. These steeper reaches may reflect activity of the Laonung antiform.

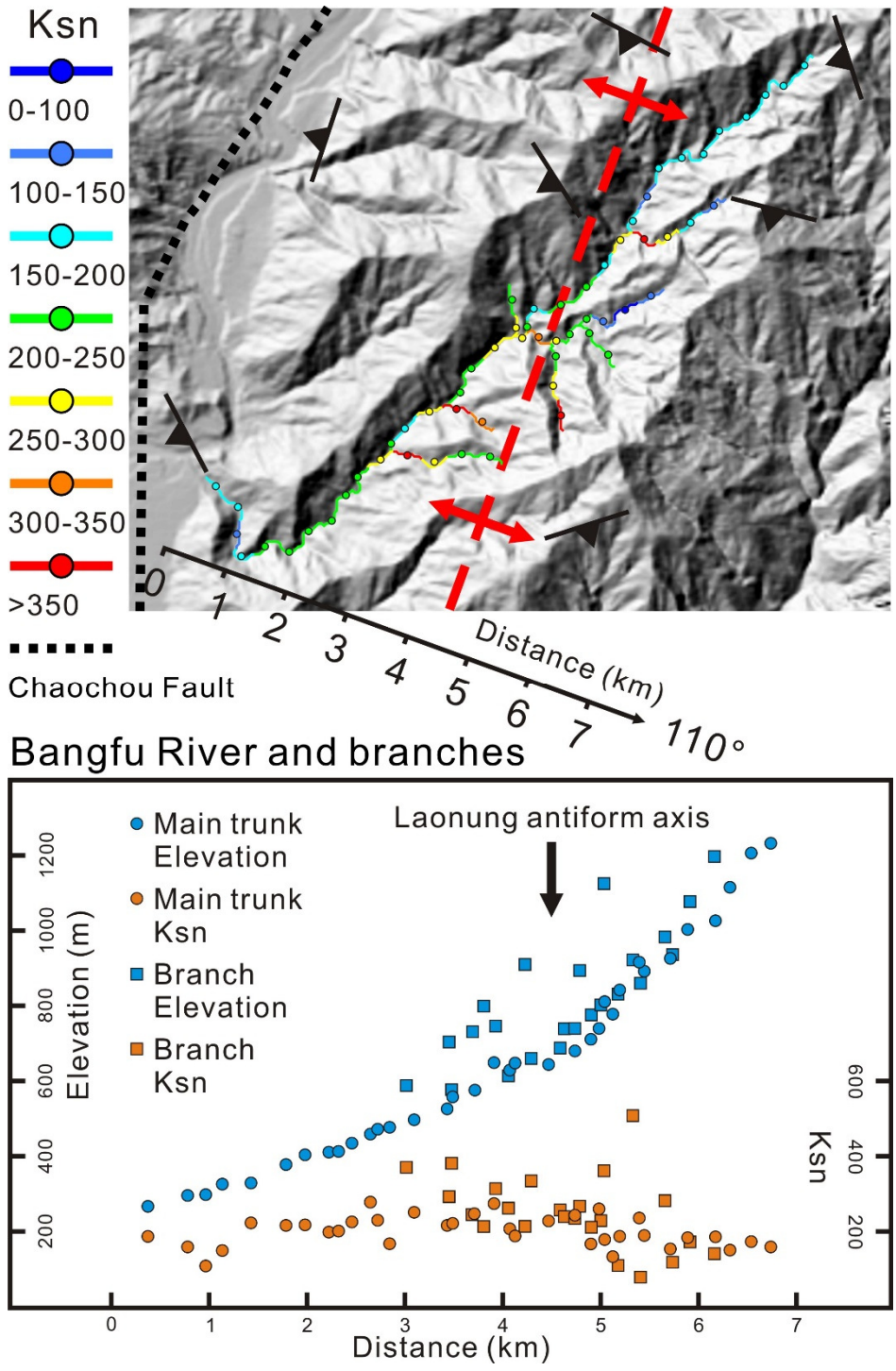

Figure 3.6. The river profile and k_{sn} profile.

3.4.4 Geomorphic indices in area of the Laonung antiform: Basin asymmetry factor (AF)

The basin asymmetry patterns in the area of the Laonung antiform can also be used to evaluate structural activity. For example, AF values in basins along the axis of the antiform are significantly lower than AF values in basins away from the axis (Figure 3.7). The low values, when viewed downstream, suggest tilting to the northwest, which is consistent with the structural and leveling data presented in Chapter 1.

In Chapter 2, we proposed that the distribution of landslides can controlled by the geometry of cleavage in a metamorphic rock region and previous workers have suggested that the AF values could also be controlled by local dip direction of cleavage or strata (Ramsey et al., 2007). In order to clarify whether the AF in the Bangfu River catchment is controlled by structural activity or by the dip direction of cleavage, we use θ_D values to better understand the origin of the AF values in the Bangfu River catchment. The θ_D value is the difference between the dip azimuth of tectonic cleavage and the down slope direction at the same location; that is, when the θ_D value is 0°, the cleavage dip direction is parallel to the slope direction and when θ_D is 180°, the cleavage and slope dip in the opposite direction. θ_D can therefore be used to estimate the potential of the dip-slope landslides in a given area.

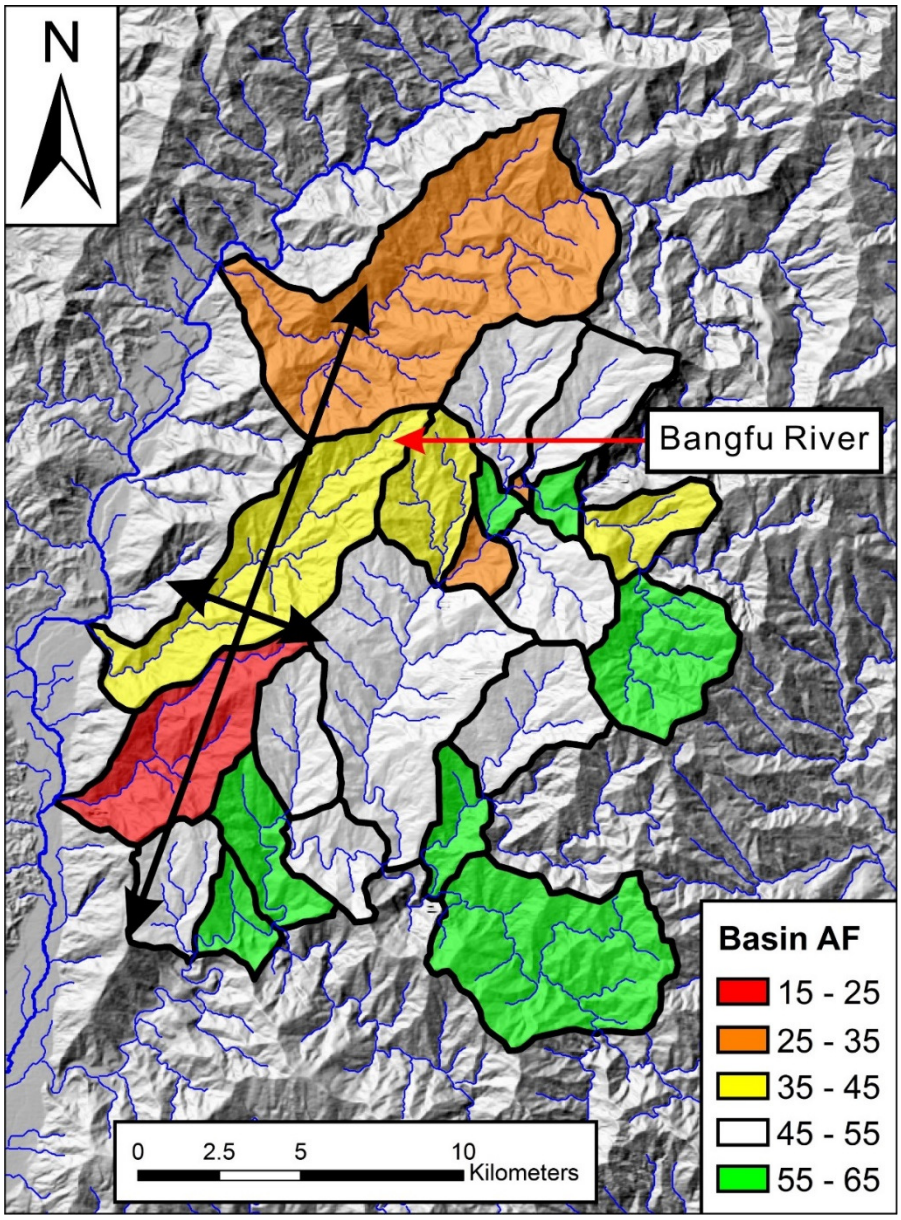

Figure 3.7. The basin asymmetry factor (AF) map of the Laonung antiform area.

Based on the result from Chapter 2 (see Figure 2.10), landslides in the Miocene slate tend to occur in areas where θ_D is less than 105°. So, if the AF in the Bangfu River reflects higher erosion rates related to dip-slope landslides rather than to northwest tilting, then the left bank, which is larger than the right bank, should have a lower θ_D than the right bank. The θ_D histogram shows, however, that both of the banks have similar θ_D distributions; in fact, the right bank has a higher percentage of area with lower θ_D values than the left bank (Figure 3.8). The AF of the Bangfu River, therefore, appears to be controlled by structural activity and tilting (to the northwest) and formation of the Laonung antiform, instead of local structural fabrics.

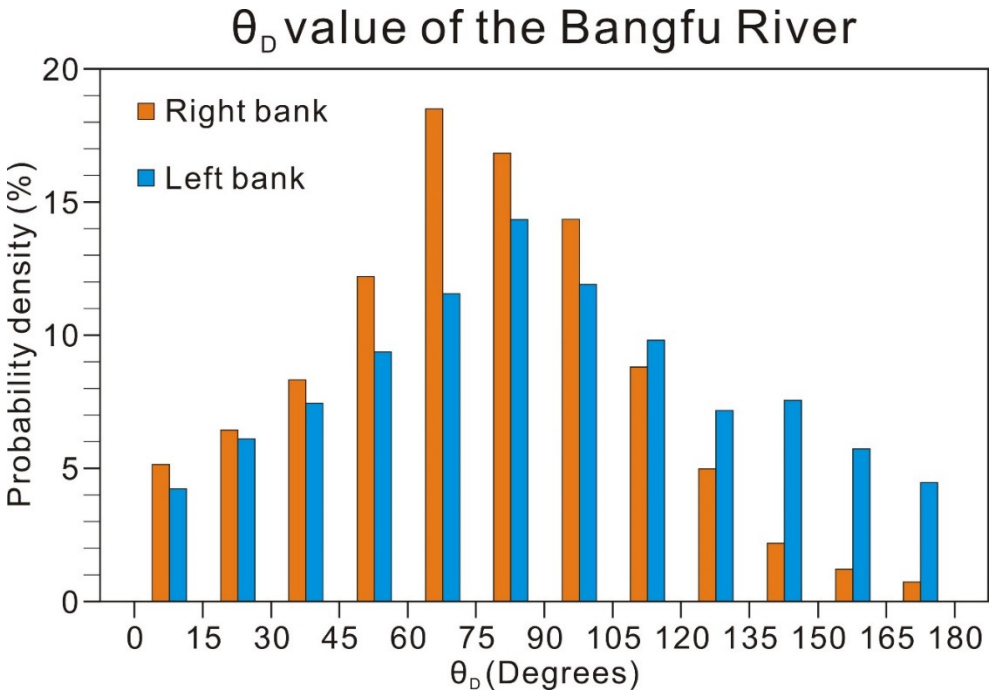

Figure 3.8. Frequency distribution histogram of θ_D value of two banks of the Bangfu River. Blue line represents left bank data, orange line represents right bank data.

3.5 CONCLUSION

The analysis of geomorphic indices in the southern Central Range suggests that differential uplift rate can be a major factor in influencing the river steepness (k_{sn}) and basin asymmetry (AF). Areas with k_{sn} values larger than 500 (circled in red line in Figure 3.9) occur primarily in the northern part of the study area and along the eastern flank of the range. Higher k_{sn} values in the north are consistent with the northward increase of asymmetry in the eastern flank of the range, suggesting higher uplift rates in the northern part of the study area. These results are consistent with a recent leveling survey that shows rates of uplift in the north of up 15mm/yr (circled by yellow line in Figure 3.9) compared to only a few mm/yr in the south. The consistency between these different techniques, which document uplift rates at different temporal scales, and the change in topography from south to north, suggest that the uplift trends are long-term and that uplift is driven by a crustal-scale processes.

Although the specific mechanism(s) driving uplift are not known, I speculate that uplift maybe driven by thrusting or duplex accretion at depth. For example, in Chapter 1 Huang and Byrne (2014), documented a regional-scale fold, the Laonung antiform that postdated the development of the ductile fabrics and appears to be currently active as evidenced by high uplift rates (purple line in Figure 3.9). Lee et al. (2006) have also proposed that a regional-scale thrust separates the Miocene and Eocene units in the central part of the range. The trend of the thrust projects northward to the South Cross-Island Highway where leveling

data show a maximum rate of uplift. One possibility therefore is that this thrust is also active and responsible for the uplift of the central part of the range. Alternatively, Simoes et al. (2007) used thermokinematic modeling, constrained by geochronologic data, to argue that uplift is driven by imbrication or accretion at depth, or more generally called underplating. Similar models of crustal deformation at depth have been recognized in the other orogenic systems (e.g., duplex accretion in Alaska, see Fisher and Byrne, 1987) and maybe operating today in Taiwan. Although the dominant process, thrusting or duplex accretion, is unknown, future studies that integrate surface deformation (e.g., GPS) and crustal scale geophysical data may provide important constraints on the geometry and kinematics of structures within the orogen.

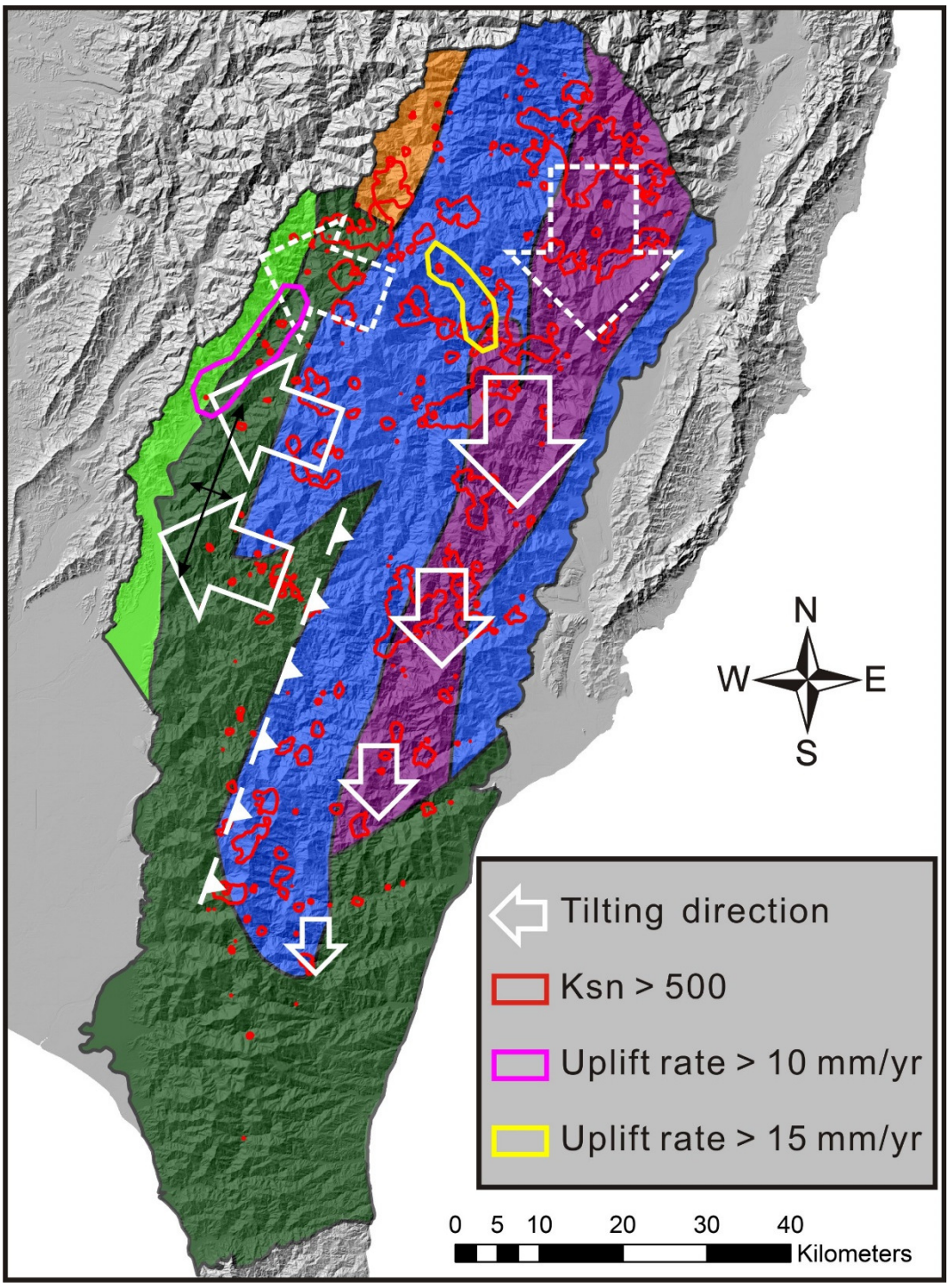

Figure 3.9. Proposed structure and surface deformation map of study area. The purple area represents the area with uplift rate higher than 10 mm/yr, and the yellow area represents the area with uplift rate higher than 15 mm/yr. The white arrows represent the tilting direction.

3.6 REFERENCE

Beyssac, O., Simoes, M., Avouac, J.P., Farley, K., Chen, Y.G., Chan, Y.C., Goffe, B., 2007. Late Cenozoic metamorphic evolution and exhumation of Taiwan. Tectonics 26, TC6001.

Byrne, T., Chan, Y.C., Rau, R.J., Lu, C.Y., Lee, Y.H., Wang, Y.J., 2011. The Arc–Continent Collision in Taiwan. Arc-Continent Collision, 213-245.

Chen, C.-H., 2000. Geologic Map of Taiwan. Central Geological Survey, Ministry of Economic Affairs.

Chen, C.-H., Wang, C.-H., 1995. Explanatory notes for the Metamorphic facies map of Taiwan, 2 ed. Central Geological Survey, Taipei, Taiwan.

Cheng, W.-B., 2004. Crustal structure of the High Magnetic Anomaly Belt, western Taiwan and its implications for continental margin deformation. Marine Geophysical Researches 25, 79-83.

Ching, K.E., Hsieh, M.L., Johnson, K.M., Chen, K.H., Rau, R.J., Yang, M., 2011. Modern vertical deformation rates and mountain building in Taiwan from precise leveling and continuous GPS observations, 2000–2008. J. geophys. Res 116, B08406.

Crespi, J., Chan, Y.C., Swaim, M., 1996. Synorogenic extension and exhumation of the Taiwan hinterland. Geology 24, 247-250.

Derrieux, F., Siame, L.L., Bourlès, D.L., Chen, R.-F., Braucher, R., Léanni, L., Lee, J.-C., Chu, H.-T., Byrne, T.B., 2014. How fast is the denudation of the Taiwan mountain belt? Perspectives from in situ cosmogenic 10Be. Journal of Asian Earth Sciences 88, 230-245.

Fisher, D., and Byrne, T., 1987. Structural evolution of underthrusted sediments, Kodiak Islands, Alaska. Tectonics, 6, 775-793.

Fisher, D.M., Willett, S., Yeh, E.-C., Clark, M.B., 2007. Cleavage fronts and fans as reflections of orogen stress and kinematics in Taiwan. Geology 35, 65-68.

Hare, P.W., Gardner, T., 1985. Geomorphic indicators of vertical neotectonism along converging plate margins, Nicoya Peninsula, Costa Rica. Allen and Unwin, Boston, 75-104.

Ho, C.S., 1986. A synthesis of the geologic evolution of Taiwan. Tectonophysics 125, 1-16.

Hsieh, M.L., Chyi, S.J., 2010. Late Quaternary mass-wasting records and formation of fan terraces in the Chen-yeo-lan and Lao-nung catchments, central-southern Taiwan. Quaternary Science Reviews 29, 1399-1418.

Hsu, S.-K., Liu, C.-S., Shyu, C.-T., Liu, S.-Y., Sibuet, J.-C., Lallemand, S., Wang, C., Reed, D.L., 1998. New Gravity and Magnetic Anomaly Maps in the Taiwan-Luzon Region and their Preliminary Interpretation. Terrestrial, Atmospheric and Ocean Sciences 9, 509-532.

Huang, C., Byrne, T.B., 2014. Tectonic evolution of an active tectonostratigraphic boundary in accretionary wedge: an example from the Tulungwan-Chaochou Fault System, southern Taiwan. Journal of Structural Geology.

Karlstrom, K., Coblentz, D., Dueker, K., Ouimet, W., Kirby, E., Van Wijk, J., Schmandt, B., Kelley, S., Lazear, G., Crossey, L., 2012. Mantle-driven dynamic uplift of the Rocky Mountains and Colorado Plateau and its surface response: Toward a unified hypothesis. Lithosphere 4, 3-22.

Kirby, E., Whipple, K.X., 2012. Expression of active tectonics in erosional landscapes. Journal of Structural Geology 44, 54-75.

Lee, J.-C., Chu, H.-T., Angelier, J., Chan, Y.-C., Hu, J.-C., Lu, C.-Y., Rau, R.-J., 2002. Geometry and structure of northern surface ruptures of the 1999 Mw=7.6 Chi-Chi Taiwan earthquake: influence from inherited fold belt structures. Journal of Structural Geology, 173-192.

Lee, Y.-H., Chen, C.-C., Liu, T.-K., Ho, H.-C., Lu, H.-Y., Lo,-W., 2006. Mountain building mechanisms in the Southern Central Range of the Taiwan Orogenic Belt—From accretionary wedge deformation to arc–continental collision. Earth and Planetary Science Letters, 252(3), 413-422.

Liao, H.S., 2003. Research of active structures along the Chaochou Fault in the southern Taiwan by geomorphic index. Master Thesis, National Central University, Chungli City, Taiwan, 124 pp.(in Chinese).

Ouimet, B.W., Byrne, B.T., Huang, C., 2012. Non-Equilibrium Topography in the southern Central Range of Taiwan, American Geophysical Union Fall Meeting, San Francisco.

Ouimet, W., Byrne, T., Siame, L., Bierman, P., Rood, D., 2013. Slow Erosion Rates, Increasing Relief and Transient Landscape Evolution within the Central Range of Taiwan, AGU Fall Meeting Abstracts, p. 02.

Ramsey, L.A., Walker, R.T., Jackson, J., 2007. Geomorphic constraints on the active tectonics of southern Taiwan. Geophysical Journal International 170, 1357-1372.

Rosenberg, R., Kirby, E., Aslan, A., Karlstrom, K., Heizler, M., Ouimet, W., 2014. Late Miocene erosion and evolution of topography along the western slope of the Colorado Rockies. Geosphere.

Simoes, M., Avouac, J. P., Beyssac, O., Goffé, B., Farley, K. A., Chen, Y. G., 2007. Mountain building in Taiwan: A thermokinematic model. Journal of Geophysical Research: Solid Earth (1978–2012), 112.

Suppe, J., 1981. Mechanics of Mountain Building and Metamorphism in Taiwan. Memoir of the Geological Society of China 4, 67-89.

Whipple, K., Wobus, C., Crosby, B., Kirby, E., Sheehan, D., 2007. New tools for quantitative geomorphology: extraction and interpretation of stream profiles from digital topographic data, Geological Society of America, Annual Meeting, Short Course Guide: Boulder Colorado.

Whipple, K.X., Tucker, G.E., 1999. Dynamics of the stream-power river incision model: Implications for height limits of mountain ranges, landscape response timescales, and research needs. Journal of Geophysical Research: Solid Earth (1978–2012) 104, 17661-17674.

Willett, S.D., Slingerland, R., Hovius, N., 2001. Uplift, shortening, and steady state topography in active mountain belts. American Journal of Science 301, 455-485.

Wiltschko, D.V., Hassler, L., Hung, J.H., Liao, H.S., 2010. From accretion to collision: Motion and evolution of the Chaochou Fault, southern Taiwan. Tectonics 29, TC2015.

Wobus, C.W., Crosby, B.T., Whipple, K.X., 2006. Hanging valleys in fluvial systems: Controls on occurrence and implications for landscape evolution. Journal of Geophysical Research: Earth Surface (2003–2012) 111.

Yu, S.-B., Cheng, H.-Y., Kuo, L.-C., 1997. Velocity field of GPS stations in the Taiwan area. Tectonophysics 274, 41-59.